UNIVERSIDAD CARLOS III DE MADRID

ELECTRICAL ENGINEERING DEPARTMENT

DOCTORAL THESIS

Nonlinear dynamic per-unit models for electrochemical energy systems. Application to a hardware-in-the-loop hybrid simulation

Author:
Lucía Gauchía Babé

Advisor:
Prof. Dr. Javier Sanz Feito

Leganés, 2009

TESIS DOCTORAL

NONLINEAR DYNAMIC PER-UNIT MODELS FOR ELECTROCHEMICAL ENERGY SYSTEMS. APPLICATION TO A HARDWARE-IN-THE-LOOP HYBRID SIMULATION

Autora: Lucía Gauchía Babé

Director: Prof. Dr. Javier Sanz Feito

Firma del Tribunal Calificador: Firma

Presidente: Dra. Inmaculada Zamora Belver

Vocal: Dr. Alain Bouscayrol

Vocal: Dr. Jesús Palma del Val

Vocal: Dra. Hortensia Amarís Duarte

Secretario: Dr. Guillermo Robles Muñoz

Calificación: Sobresaliente cum laude

Leganés, 15 de diciembre de 2009

Agradecimientos

Esta Tesis no habría visto la luz de no haber sido por la decisión de mi director, Dr. Javier Sanz Feito, de abrir esta nueva línea de investigación. Su apoyo, consejo, y entrega, más allá de lo imaginable, han sido una constante durante estos años. Gracias por el tantísimo tiempo que me has dedicado, por las revisiones maratonianas en fin de semana, por tu comprensión en los momentos personales difíciles, por tu sentido del humor y por tu generosidad. Javier, es todo un honor trabajar contigo.

Querría agradecer a Exide-Tudor las baterías cedidas para los ensayos y a Juan Carlos el apoyo para la adquisición del sistema dSpace.

Gracias a Sandra por ayudarme en la recta final de mi Tesis, que es el inicio de la suya.

A todos los miembros del Departamento de Ingeniería Eléctrica, especialmente a mis compañeros de doctorado, por tantos cafés, risas, angustias y horas compartidas: Diana, Mónica R., Carlos G., Carlos A., Miguel G.L., Miguel M., Mónica A., Jaime y Álvaro.

Querría destacar el ánimo e interés de Hortensia, Juan Carlos, Mª Ángeles, Jorge, Juanma, Edgardo, Belén y Javier R. También a Guillermo, por sus consejos y bromas. Gracias a Quino y David, por sus consejos y por prestarme su dSpace cuando más la necesitaba. Mónica Ch., gracias por ese año en el que trabajamos juntas, no sabes lo que agradecí tu compañía, cariño, explicaciones y ayuda.

Mi infinita gratitud a mis padres, por su inquebrantable fe en mi, su aliento, y su amor incondicional. A mi madre, gracias por ser ejemplo de fortaleza, por tus innumerables detalles y por tu comprensión. A mi padre, gracias por tu desinteresada entrega, horas de explicaciones y partidos de tenis. No tengo palabras para agradeceros todo vuestro cariño. Os debo todo lo que soy.

Gracias a mi hermano Padua, por soportar con infinita paciencia mis horarios y conversaciones monotemáticas. Gracias por ser el catalizador de las necesarias distracciones.

Mil gracias a Ángel y Alicia, compañeros y amigos de carrera y doctorado. Con vosotros, las dificultades lo eran menos y las alegrías de uno, las de todos.

Por último, gracias a mis amigos Pepa, María, Jose, César, Miriam, Rubén, Ramón, etc., por entender mis ausencias.

Acknowledgments

This Thesis would not have existed without the decision of my advisor Dr. Javier Sanz Feito to open this new research line. His support, advice and devotion have been a constant during these years. Thank you for enormous amount of time you have dedicated, for the reviews during weekends, for your understanding during difficult personal situations, for your sense of humor and for your generosity. Javier, it is a real honor to work with you.

I would like to thank Exide-Tudor for providing the batteries and to Juan Carlos for supplying the dSpace system.

Thank you to Sandra for helping me in the last part of my Thesis, which is the first on of her own Thesis.

To all the members of the Electrical Engineering Department, especially to my Doctorate fellows, for so many shared coffees, laughters, anguishes and hours: Diana, Mónica R., Carlos G., Carlos A., Miguel G.L., Miguel M., Mónica A., Jaime. y Álvaro.

I would like to highlight the interest and encourage shown by Hortensia, Juan Carlos, Mª Ángeles, Jorge, Juanma, Edgardo, Belén y Javier R. Thank you to Guillermo, for your advice and jokes. Thanks to Quino and David, for their advice and for lending me their dSpace system when I most needed it. Mónica Ch., thank you for the year in which we worked together, you cannot imagine how much I appreciated your company, kindliness, explanations and help.

My infinite gratitude to my parents, for their unwavering faith in me, for their support and unconditional love. To my mother, thank you for being an example of fortitude, for your innumerable gestures and for your understanding. To my father, thank you for your uninterested devotion, hours of explanations and tennis matches. I cannot find words to acknowledge all your love. I owe you what I am.

Thank you to my brother Padua, for enduring with infinite patience my timetable and monothematic conversations. Thank you for being the catalyst of the necessary distractions.

Many thanks to Ángel and Alicia, fellows during undergraduate and doctorate studies. With you, the difficulties lessened and the joy of one turned to be the joy of all three.

Last but not least, thank you to my friends Pepa, María, Jose, César, Miriam, Rubén, Ramón, etc., for understanding my absences.

Resumen

La situación energética actual está dominada por los combustibles fósiles, especialmente por el petróleo. Esta dependencia se está conviertiendo en arriesgada debido a las decrecientes reservas, a la incertidumbre de los recursos de petróleo y a las consecuencias económicas y políticas de una concentración de reservas en países de Oriente Medio. El sector transportes tiene una particular dependencia del petróleo como combustible y es una fuente de contaminación debido a su combustión.

De cara a reducir esta dependencia se están introduciendo energías renovables como fuentes alternativas de energia. Las más comunes son la eólica y la fotovoltaica, aunque existen otros tipos, como las energías mareomotriz, de gradiente térmico, biomasa o undomotriz. El principal inconveniente de estas energías es su carácter no programable, que fomenta el uso de sistemas de almacenamiento de energía.

Las energías renovables mencionadas no son aplicables a vehículos, por lo que para el sector transportes es más interesantes el uso de vectores energéticos tales como el hidrógeno. El hidrógeno puede ser un sustituto del petróleo para aplicaciones vehiculares, pero primero se han de resolver ciertos problemas, como son el elevado coste, la seguridad y el establecimiento de una infraestructura de distribución de hidrógeno. Como en el caso de los sistemas estacionarios renovables, las pilas de combustible de aplicación vehicular necesitan sistemas de almacenamiento de energía que sean capaces de suministrar picos de potencia durante la aceleración o subiendo una pendiente.

Esta situación energética ha provocado un incremento del desarrollo e investigación de sistemas electroquímicos, tales como las pilas de combustible, las baterías y los supercondensadores. Sobretodo, se está realizando un esfuerzo en el diseño, modelado, control y fabricación de estos sistemas, que permita su implantación tanto en aplicaciones estacionarias como vehiculares o portátiles.

Esta Tesis presenta el modelado dinámico no lineal de sistemas electroquímicos tales como las pilas de combustible, las baterías y los supercondesadores a través de ensayos en el dominio de la frecuencia, además de su validación con resultados experimentales. Se propone un sistemas por unidad para aquellos sistemas electroquímicos activos (pila de combustible y

batería). Estos sistemas son una herramienta útil para el diseño y comparación, debido a la gran variedad de tensiones y capacidades que pueden encontrarse, por ejemplo, en las baterías. Además, se ha propuesto un método de ensayo de espectroscopía de la impedancia para supercondensadores durante elevadas corrientes. Los resultados obtenidos y la comparación con resultados experimentales son muy positivos.

Por último, se ha realizado una simulación hardware-in-the-loop de sistemas híbridos de energía. La simulación realizada presenta un coste y complejidad menor que otros tipos de simulaciones. Esto es debido a que los elementos más caros, como es la pila de combustible, son sustituidos por una fuente de potencia programable capaz de reproducir la dinámica de tensión y corriente de la pila de combustible. Además, se propone un simulador de vehículo, capaz de reproducir, tanto la potencia demandada por el vehículo como el frenado regenerativo. La pila de combustible simulada y una batería real alimentan en paralelo al vehículo simulado, permitiendo llevar a cabo una simulación por unidad del conjunto y la prueba de diferentes estrategias de control para un determinado ciclo de conducción.

Abstract

The current energy situation is dominated by fossil fuel, especially oil. This dependency is turning critical due to the reducing reserves, uncertain oil resources, and political and economical ramifications of a concentration of fossil fuel reserves on the Middle East countries. The transportation sector is especially dependant on oil, and the combustion of oil produces environmentally harmful emissions.

Renewable energies are being introduced to reduce this fossil fuel dependency and emissions. The most extended are wind and solar photovoltaic, but other types such as tidal, thermal gradient, biomass or wave energy are also under research. The principal disadvantage of these renewable energies is its non-dispatchable nature, which forces the use of energy storage systems.

The renewable energies mentioned are not viable for the transportation sector, which considers more interesting other energetic vectors such as hydrogen. Hydrogen could substitute oil, but must first overcome cost, safety and hydrogen filling stations infrastructure problems. Just as in the case of stationary systems, fuel cells need energy storage systems, in this case to supply high power peaks during acceleration.

This energetic situation has caused an increase of the research and development of electrochemical systems, such as fuel cells, batteries and ultracapacitors. Intense research is being carried out in modeling, control and manufacture in order to apply them to both vehicular and stationary applications.

This Thesis presents the nonlinear dynamic modeling of electrochemical systems, such as fuel cell, batteries and ultracapacitors, through frequency domain tests and its validation with experimental tests. A per-unit system has been proposed for the active electrochemical systems: fuel cell and battery. This per-unit approach has revealed as a useful tool for comparison and design, due to the great disparity of voltages and capacities, e.g. in batteries, which can be found. Moreover, an experimental setup has been proposed in order to allow the electrochemical impedance spectroscopy tests of ultracapacitors during high current loads. Tests were carried out satisfactorily and a precise model was obtained.

Finally, a hardware-in-the-loop simulation for hybrid energy sources is presented. The simulation carried out has a lower cost and complexity compared to the real system. This is due to the fact that the higher cost system, the fuel cell and hydrogen installation, was substituted by a controlled dc power source able to reproduce its current and voltage evolution. Moreover, a vehicle simulator, able to reproduce the vehicle power demand and regenerative breaking is proposed. The simulated fuel cell and a real battery are connected to the simulated vehicle, allowing to carry out a per-unit simulation of different control strategies for a particular driving cycle.

Contents

Agradecimientos i

Acknowledgments iii

Resumen v

Abstract vii

Index of symbols xix

1. *Objectives* **1**

2. *Introduction* **3**
2.1. Current and future energy situation 3
2.2. Electrochemical systems 10
2.2.1. Fuel cells 10
2.2.1.1. The stack and operational principle 11
2.2.1.2. Auxiliary systems 14
2.2.1.3. Characteristic curve 15
2.2.2. Batteries 16
2.2.2.1. Parts and operational principle 17
2.2.2.2. Characteristic curve and principal variables . 20
2.2.3. Ultracapacitors 21
2.2.3.1. Parts and operational principle 21
2.2.3.2. Characteristic curve 23

3. *State-of-the-art* **25**
3.1. Introduction 25
3.2. Modeling techniques 25
3.2.1. Time domain tests 26
3.2.1.1. Current interruption 26
3.2.2. Frequency domain tests 28
3.2.2.1. Electrochemical impedance spectroscopy (EIS) 28
3.3. State-of-the-art of the modeling of electrochemical systems . . 35
3.3.1. Fuel cells 35
3.3.2. Batteries 39
3.3.3. Ultracapacitors 43

3.4. State-of-the-art of the simulation of hybrid electrochemical systems 47

4. *Nonlinear dynamic model for fuel cells* **55**
4.1. Introduction 55
4.2. EIS tests experimental procedure 56
4.2.1. DC operation conditions 58
4.2.2. AC test conditions 59
4.2.3. Experimental setup 60
4.3. EIS tests results: fuel cell impedance model 61
4.3.1. Fuel cell equivalent circuit 65
4.3.2. Temperature model 69
4.3.3. Complete model validation 72
4.4. Per-unit approach 73
4.4.1. Steady-state per-unit system for a fuel cell 73
4.4.2. Per-unit approach during alternate loads 75
4.5. Conclusions 77

5. *Nonlinear dynamic model for batteries* **79**
5.1. Introduction 79
5.2. EIS tests experimental procedure 80
5.2.1. DC operation conditions 81
5.2.2. AC test conditions 82
5.2.3. Experimental setup 83
5.3. EIS tests results: battery impedance model 85
5.4. Tests for the determination of the battery internal voltage . . 90
5.5. Complete battery model 94
5.5.1. State of charge calculation 96
5.6. Per-unit approach to batteries 98
5.6.1. Steady-state per-unit system for a battery 103
5.6.2. Per unit representation of the discharge curve 104
5.6.3. Per-unit approach during alternate loads 107
5.7. Conclusions 109

6. *Nonlinear dynamic model for ultracapacitors* **111**
6.1. Introduction 111
6.2. EIS tests experimental procedure 111
6.2.1. EIS test conditions 113
6.2.2. EIS experimental setup proposed 115
6.2.3. EIS tests results 116
6.2.4. Ultracapacitor impedance model and validation 122
6.3. Conclusions 124

7. *HIL simulation for hybrid energy sources* **127**
7.1. Introduction 127
7.2. HIL description 129
7.2.1. Per-unit HIL simulation 131
7.3. HIL implementation 132
7.3.1. Vehicle model 132
7.3.2. Vehicle simulator 133
7.3.3. Fuel cell simulator 134
7.3.4. HIL power connections 136
7.4. HIL acquisition and control system 138
7.4.1. HIL acquisition system 138
7.4.2. HIL control system 138
7.4.2.1. Energy management modes (EMM) 140
7.5. HIL experimental results 143
7.6. Conclusions 145

References **xxiii**

Index of figures

2.1. Hubbert chart for oil peak production [1] 4
2.2. Proven (darker) vs. recoverable (shaded) oil reserves [2] 5
2.3. Historic world energy consumption [3] 5
2.4. Historic world carbon dioxide production [3] 6
2.5. Electricity generation by fuel (left) and renewable source (right) [3] 7
2.6. European energy consumption by sectors (left) and transportation modes (right) [4] 8
2.7. Characteristics comparison for different fuels [5] 9
2.8. Components of an individual fuel cell 11
2.9. PEMFC operation principle 12
2.10. PEMFC auxiliary systems 14
2.11. PEMFC characteristic curve 15
2.12. Parts of a commercial battery [6] 17
2.13. Reactions during the battery discharge process 19
2.14. Reactions during the battery charge process 19
2.15. 12 V Lead acid battery characteristic curve 20
2.16. Components and operation of ultracapacitors [7] 22
2.17. Ragone chart for different energy storage systems 23
2.18. 3000 F Maxwell ultracapacitor 23

3.1. Current interruption test 27
3.2. Equivalent circuit obtained from the current interrupt test . . 28
3.3. Linearity of the characteristic curve 29
3.4. EIS test diagram 31
3.5. Nyquist plots for ideal elements 32
3.6. Nyquist plots for combined ideal elements 33
3.7. Nyquist plots for diffusion elements 34
3.8. Equivalent circuit presented by Pathapati and Larminie [8] . . 36
3.9. Equivalent circuit presented by Garnier and Laffly [9] 37
3.10. Equivalent circuit presented by Cooper [10] 38
3.11. Equivalent circuit presented by Choi [11] 38
3.12. Equivalent circuit presented by Karden [12] 39
3.13. Equivalent circuit presented by Nelatury [13] 40
3.14. Equivalent circuit presented by Baert [14] 40
3.15. Equivalent circuit presented by Salkind [15] 41
3.16. Equivalent circuit presented by Thele [16] 42

3.17. Hysteresis effect on the battery open circuit voltage presented by Thele [16] 42
3.18. Ultracapacitor equivalent circuit presented by Zubieta [17] . . 44
3.19. Ultracapacitor equivalent circuit presented by Buller [18] . . . 44
3.20. Ultracapacitor equivalent circuit presented by Dougal [19] . . . 45
3.21. Ultracapacitor voltamogram presented by Lajnef [20] 46
3.22. Ultracapacitor equivalent circuit presented by Rafik [21] 47
3.23. Signal level HIL simulation 48
3.24. Power level HIL simulation 49
3.25. HIL test bench for all electric ship simulation [22] 49
3.26. HIL simulation presented by Moore [23] 50
3.27. Mechanical level HIL simulation 51
3.28. HIL test bench for diesel hybrid vehicles [24] 52
3.29. HIL simulation presented by Cheng [25] 52
3.30. HIL simulation presented by Schupbach [26] 53
3.31. HIL simulation presented by Winkler [27] 53

4.1. Characteristics of the Nexa fuel cell 57
4.2. Nexa fuel cell characteristic curve [28] 57
4.3. Nexa fuel cell used 58
4.4. *EIS* on fuel cells 58
4.5. EIS test linearity vs. final model nonlinearity 60
4.6. Experimental setup for Nexa fuel cell EIS tests 61
4.7. Experimental setup photograph 62
4.8. Nexa fuel cell Nyquist and Bode plots 63
4.9. Fuel cell parameters rendered by ZView 64
4.10. CPE and R-CPE Nyquist plots 64
4.11. Difference in the C or CPE fitting 65
4.12. Fuel cell equivalent circuit 66
4.13. Information returned by Statgraphics for *R1* 67
4.14. Temperature evolution for different current steps 69
4.15. Statgraphics result for the thermal time constant 70
4.16. Current profile applied to fuel cell and model 71
4.17. Temperature model validation 71
4.18. Fuel cell Matlab/Simulink model 72
4.19. Complete model validation 72
4.20. Nexa fuel cell voltage and power characteristic in absolute (left) [28] and p.u. values (right) 74
4.21. Cut-off and resonance frequency 76
4.22. Nexa fuel cell resonance frequency 77

5.1. *EIS* on batteries 81
5.2. Experimental setup for battery EIS tests for a) discharge b) charge 84
5.3. EIS tests experimental setup photograph 85

5.4. Nyquist diagram for 70 % SoC during discharge 86
5.5. Bode diagram for 70 % SoC during discharge 86
5.6. Approximation of the Nyquist plot 87
5.7. Cut-off frequency evolution with SoC 87
5.8. Resonance frequency evolution with SoC 89
5.9. Equivalent circuit obtained through ZView 90
5.10. Statistical analysis for R_2 91
5.11. Equivalent circuit for the battery impedance 91
5.12. Charge efficiency 93
5.13. Hysteresis curve for OCV 95
5.14. Statgraphics observed vs. predicted curves for OCV during discharge (left) and charge (right) 95
5.15. Active equivalent circuit of the battery for a)charge and b)discharge 96
5.16. OCV vs. SoC 97
5.17. Matlab/Simulink model for the battery 98
5.18. Detail of the Matlab/Simulink model 99
5.19. Discharge current profile required to the battery 99
5.20. Experimental and modeled battery voltage during discharge . 100
5.21. Charge current profile injected in the battery 100
5.22. Experimental and modeled battery voltage during charge . . . 101
5.23. Discharge curve obtained by a)Doerffel and b)Gauchia in absolute values 105
5.24. Discharge curve obtained by a)Doerffel and b)Gauchia in p.u. values 107

6.1. 3000F Maxwell ultracapacitor 112
6.2. EIS control procedure for ultracapacitors 116
6.3. Currents and voltage evolutions for each equipment 117
6.4. EIS experimental setup 118
6.5. Photograph of the ultracapacitor EIS setup 119
6.6. Nyquist and Bode plots obtained for the ultracapacitor after the EIS tests 120
6.7. High frequency effect on the pore effective surface. Adapted from [29] 121
6.8. Equivalent circuit fitted with ZView 122
6.9. Ultracapacitor equivalent circuit 122
6.10. Ultracapacitor Matlab/Simulink model 123
6.11. Abrupt ultracapacitor current load 124
6.12. Experimental and modeled voltage 125

7.1. Case studied 129
7.2. Forces present in a vehicle while driving uphill 132
7.3. Vehicle simulator proposed 135
7.4. Fuel cell simulator proposed 135
7.5. HIL simulation power wiring 136

7.6. Chassis developed for power connections 137
7.7. Chassis upper (left) and lower (right) floor 137
7.8. HIL Matlab/Simulink programme 139
7.9. HIL simulation 140
7.10. HIL photograph 141
7.11. Fuel cell recharge current to the battery 142
7.12. NEDC driving cycle and downsized power (10:1) 143
7.13. Energy management mode 1 146
7.14. Energy management mode 2 147

Index of tables

4.1. Steady-state base magnitudes 74

5.1. Characteristics of the battery used 80
5.2. Experimental procedure to calculate the OCV after discharge 93
5.3. Experimental procedure to calculate the OCV after charge . . 94
5.4. Comparison between different authors 102
5.5. Proposed base variables for a battery 104
5.6. Proposed base variables for a battery 104
5.7. Base values for the Exide-Tudor battery studied 106
5.8. Base values for the BLA1 battery used by Doerffel 106

6.1. Maxwell Boostcap 3000F ultracapacitor characteristics 112

7.1. Parameters for the simulated vehicle 133

Index of symbols

A	Vehicle frontal surface
C	Capacitance
C_d	Drag coefficient
C_{dl}	Double layer capacitor
C_n	Battery rated capacity
DoD	Depth of discharge
E	Fuel cell internal voltage
E_0	Reversible cell potential
EL	Electronic losses
ESR	Equivalent series resistance
f	Frequency
f_0	Static friction coefficient
f_b	Base frequency
f_c	Cut-off frequency
f_r	Resonance frequency
f_v	Dynamic friction coefficient
F	Faraday constant
F_i	Forces present in the vehicle while driving
g	Gravitational acceleration
I	Current
I_{ac}	Current alternating component
I_b	Base current
I_c	Leakage current
I_{dc}	Current direct component
I_{sc}	Shortcircuit current
j	Imaginary unit
k_i	Winding losses
L	Inductance

m	Weight
n_i	Mols of gas i
OCV	Open circuit voltage
p	Constant phase element exponent
pc	Peukert coefficient
p_{H2}	Hydrogen partial pressure at the anode
p_{O2}	Oxygen partial pressure at the cathode
p_{H2O}	Water partial pressure at the cathode
P	Power
P_b	Base power
q_i^{in}	Flow of i species which enter the stack
q_i^{out}	Flow of i species which leave the stack
q_i^r	Flow of i species which react in the stack
R	Universal gas constant
R_i	Resistance
R_a	Charge transfer resistance
SoC	State of charge
SoH	State of health
SR	Stoichiometric relationship
t	Time
t_b	Base time
T	Temperature (Torque for chapter 7)
T_{cpe}	Constant phase element parameter
U	Voltage
U_{bat}	Battery voltage
U_{fc}	Fuel cell voltage
U_{uc}	Ultracapacitor voltage
$U_{C_i,L}$	Voltage drop at i capacitor or inductance
U_b	Base voltage
V_{an}	Volume of gas at the anode
X_i	Reactance
Y	Admitance

Z	Impedance
Z_b	Base impedance
Z_w	Warburg impedance
Z'	Real part of the complex impedance
Z"	Imaginary part of the complex impedance

Greek symbols

η	Efficiency
Θ	Slope angle
ρ_{air}	Air density
τ	Time constant
ω	pulsation

Acronyms

ac	Alternating current
AGM	Absorbed glass matt
ADVISOR	Advanced vehicle simulator
CPE	Constant phase element
dc	Direct current
DMFC	Direct methanol fuel cell
EDLC	Electric double layer capacitor
EIS	Electrochemical impedance spectroscopy
FCHEV	Fuel cell hybrid electric vehicle
HEV	Hybrid electric vehicle
HIL	Hardware-in-the-loop
ICE	Internal combustion engine
MEA	Membrane electrode assembly
p.u.	Per-unit
PEMFC	Proton exchange membrane fuel cell
SOFC	Solid oxide fuel cell
VRLA	Valve regulated lead acid batteries
YARC	Arc in the Y plane
ZARC	Arc in the Z plane

Greek based acronyms

ε ARC	Arc in the complex plane

CHAPTER 1

Objectives

The general objective of this Thesis is to open a new research line about hydrogen and electrochemical systems in the Electrical Engineering Department at the Carlos III University. This first approach is more focused on the electrochemical systems itself and vehicular applications, leaving the stationary applications to the near future.

Electrochemical systems are now on the focus of researchers, due to the opportunities they offer. They specially received attention from, obviously, electrochemical engineers who develop them, and from power electronic engineers who design the power converters which interface the electrochemical system and the load.

In this Thesis electrochemical systems are studied from an electric point of view, with which dynamic nonlinear models for fuel cell, batteries and ultracapacitors will be developed. This electrical focus includes the proposal of a per-unit system for electrochemical systems, in order to facilitate the integration of the models developed with conventional power systems. The particular objectives can be described as:

- Acquire a thorough knowledge of the electrochemical systems operation and state-of-the-art of the modeling techniques.
- Select the most appropriate modeling technique and apply it to fuel cells, batteries and ultracapacitors.

- Definition of the nonlinear models for each of the electrochemical systems: circuit topology and parameters.
- Develop an experimental setup which allows the test of ultracapacitors under high current loads for electrochemical impedance tests.
- Experimental validation of the dynamic nonlinear models obtained for the fuel cell, battery and ultracapacitor.
- Development of a per-unit system and definition of base values which are able to define the particularities of each electrochemical system.
- Design a hardware-in-the-loop (HIL) simulation which allows testing hybrid energy systems in a flexible, low cost and safe way.

The Thesis contents are distributed through eight different chapters. Chapter 1 starts with an introduction to the current energetic situation and principle of operation and parts of the different electrochemical systems. The state-of-the-art for the electrochemical modeling and HIL simulation is studied during Chapter 3, whilst Chapters 4, 5 and 6 present the fuel cell, battery and ultracapacitor modeling. The HIL simulation is included in Chapter 7, as well its application to a vehicular case. Chapter 8 closes the Thesis document with the conclusions, contribution, future work and publications.

CHAPTER 2

Introduction

Electrochemical systems are capable of generating and/or storing electric energy, and have an undeniable power electric use. However, they are not classic power electric elements, such as transformer, electric machines, or even more recent solar photovoltaic panels. Therefore, this chapter presents the future energy situation, and its possible effects on the energy scene, as well as an introduction to the different types of renewable energy sources and especially electrochemical systems.

2.1. Current and future energy situation

Nowadays the energy scene is dominated by fossil fuels, such as oil, gas and coal. This strong dependency on oil causes worldwide concern due to its mutual effects on the geopolitical, economic and environmental situation.

Even though these fossil fuels are naturally produced, the rate at which they are consumed is faster than the rate at which they are produced, and causes a dependency on the available reserves. It is not straightforward to calculate the amount of oil reserves, due to the location and deepness at which they can be found. It is an extended idea that the amount of these reserves is reducing dramatically, and as a consequence the oil extraction will also be reduced. This idea is supported by the Association for the Study of

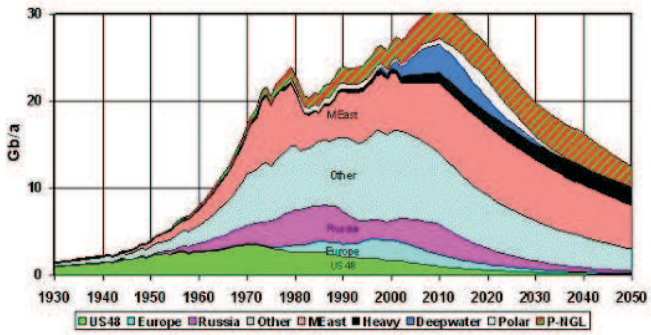

Fig. 2.1: Hubbert chart for oil peak production [1]

Peak Oil and Gas (ASPO), who predicts that the maximum oil extraction peak will be reached before 2020. This can be observed in Fig. 2.1.

Analyzing Fig. 2.1 and Fig. 2.2, it cannot be neglected that most reserves from which oil will be extracted after the peak is reached proceed from the Middle East. This fact increases concern due to their unstable political situation and future oil prices, undoubtedly high due to monopoly and reserve shortage.

However, there are dissenting voices to this, like the U.S. Geological Survey USGS (belongs to the U.S. Department of Interior). They presented the World Petroleum Assessment in 2000, in which they studied the oil reserves and resources, understanding reserves as known-but-not-exploited oil deposits, and resources as unknown oil deposits. Fig. 2.2 presents the corrected data for the USGS focus. It should be observed the difference in the location of reserves. Even though the Middle East countries keep a high percentage of reserves, North, Center and South America, as well as Europe see their resources increased.

These current decreasing reserves and uncertain resources collides with the increasing energy consumption. OECD countries continue to be the prime sink of energy, however, non-OECD countries, specially China and India will show a remarkable increase in their consumption. This is backed up by the International Energy Outlook 2009 report (published by the Energy Information Administration EIA, USA), which released the data shown in Fig. 2.3.

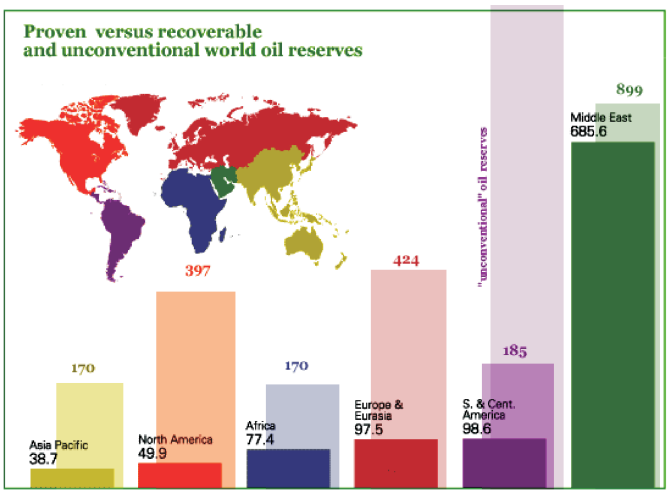

Fig. 2.2: Proven (darker) vs. recoverable (shaded) oil reserves [2]

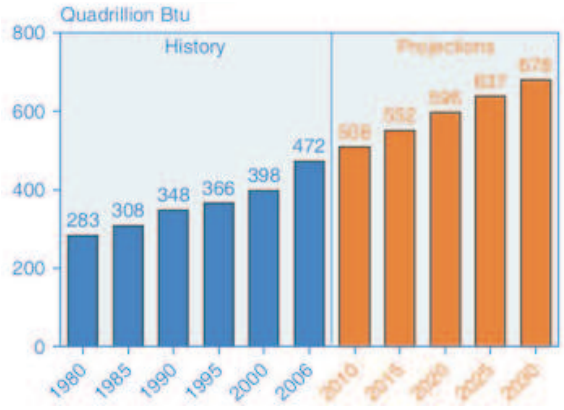

Fig. 2.3: Historic world energy consumption [3]

The increased 44 % of energy consumption from 2006 to 2030 will generate an increment in the carbon dioxide production, which will mostly proceed from non-OECD countries. The International Energy Outlook report expects non-OECD countries to generate a 77 % more carbon dioxide than OECD countries, due to their increasing economic and energy consumption growth. OECD countries are expected to maintain or slightly increase its emissions, as shown in Fig. 2.4.

With this general scene in mind, other energy sources, such as renewable ones are being explored in order to reduce environmental impact and oil dependency. Renewable energies have been historically used, principally water

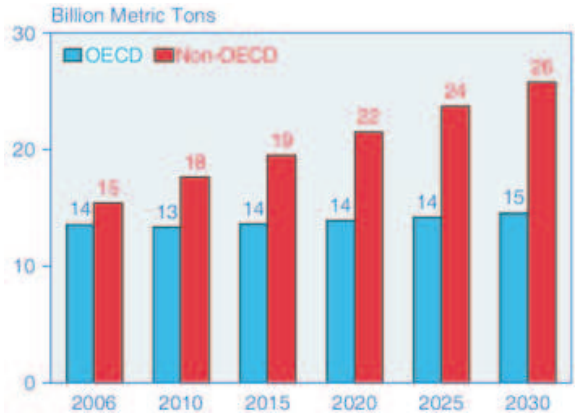

Fig. 2.4: Historic world carbon dioxide production [3]

for water mills and wind for boat propulsion. As shown in Fig. 2.5 water is still the most popular renewable energy source, followed by wind. However, there are other types of renewable energies. A non-exhaustive list of other renewable energies is [5]:

- Tidal energy: It is reliable and predictable, but difficult to actually setup.
- Solar photovoltaic: The sun path is also predictable, but weather introduces unpredictable energy output.
- Wave energy: Highly dependant on wind.
- Thermal gradient energy: It is specially interesting in tropical seas.
- Geothermal energy: Produces non-negligible emissions and is related to seismic activity.
- Biomass energy: It can be programmable.

One of the most important disadvantages of these renewable energies, apart from their higher cost, is its intermittent nature. Currently, fossil power plants do not present this problem due to its dispatchable nature, but a power system with a heavy renewable penetration needs some sort of energy storage in order to store the unused energy, instead of spilling it.

Energy storage is still a challenge and is receiving special attention due to its highly attractive hybridization with renewable energies. There is a wide range of technologies at different maturity levels, such as [30]:

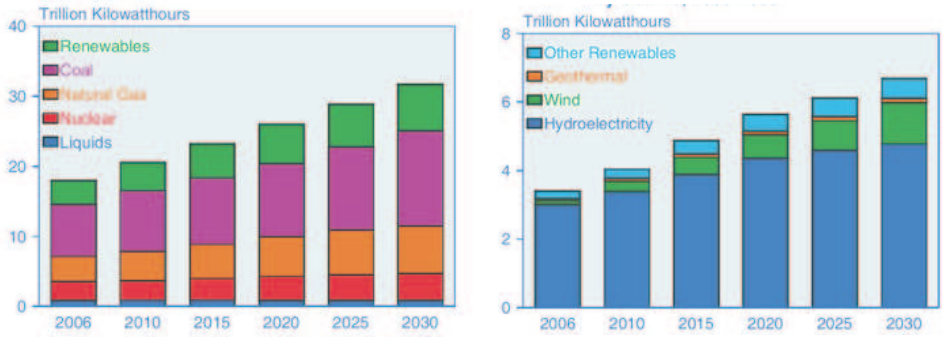

Fig. 2.5: Electricity generation by fuel (left) and renewable source (right) [3]

- Electrochemical storage: ultracapacitors.
- Kinetic energy storage: Uses the energy due to movement, as applied by flywheels.
- Potential energy storage: it can be elastic (spring application) or gravitational.
- Chemical energy storage: batteries are the most common example.
- Thermal and chemical energy storage: transforms the solar energy to chemical energy.
- Magnetic energy storage: stores energy in a magnetic field created by the flow of direct current through a superconductive coil.

These storage technologies can be used for stationary, transport and portable applications, but the renewable energies mentioned before are more focused for stationary applications [31] (even if, e.g., photovoltaic energy can be used for both transportation and portable systems) due to the fact few of these storage systems are applicable to transport, and those which apply (electrochemical, chemical and kinetic) present low energy densities. Therefore, transport systems need other propulsion systems with higher energy densities, which, in most cases, require some type of fuel. Oil replacement in the transportation sector is essential to reduce the harmful emissions and reduce the oil dependency. According to the 2007 Eurostat Energy, Transportation and Environment Indicators report, transportation (specially road transport) consumes a significant percentage of the total energy consumed, as seen in Fig. 2.6.

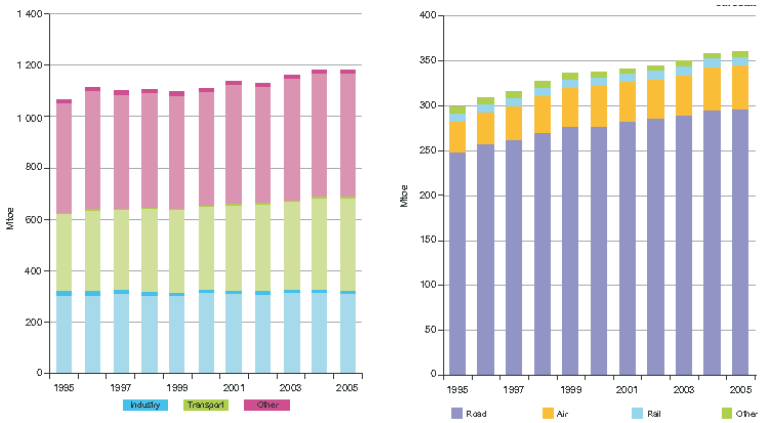

Fig. 2.6: European energy consumption by sectors (left) and transportation modes (right) [4]

A variety of fuels are being tested as a substitute of oil, some of which, as classified by the U.S. Department of Energy, present the characteristics presented in Fig. 2.7. Some of these fuels are already being used, especially biodiesel, natural gas, ethanol, methanol and propane. Hydrogen is also being used in order to study its viability as energy vector. However, it is not used in a large scale. This is due to the fact that there are still some challenges to be overcome. These challenges include onboard storage, transport, cost and safety.

An overview of types of hydrogen storage can be consulted in [32]. Basically there are two states in which hydrogen can be stored: gas or liquid. Gas state storage includes high pressure tanks, underground storage, storage with metal hydrides, which allow a lower storage pressure and storage in microspheres or nanotubes. Liquid storage is specially useful when high density is needed, as in aeronautical applications, but presents the inconvenience of cryogenic temperatures and the presence of the corresponding insulator. These storage challenges also influence the transport and distribution of hydrogen [33].

One of the principal drawbacks for a safe use of hydrogen is its small molecular size, which allows it to leak through pores or joints. Therefore, the storage tanks, joints and pipes used for the hydrogen flow must observe strict security measures. Due to its low atomic weight, if hydrogen leaks outdoors it quickly disperses in the surrounding atmosphere, and the risk of explosion

	Main source	Energy content (lower heating value)	Energy content (higher heating value)	Energy comparison (% of gasoline energy)	Physical state	Price ($/l)
Gasoline	Crude oil	8,974 kWh/m3	9,611 kWh/m3	100%	Liquid	0,644
Diesel	Crude oil	9,929 kWh/m3	106,19 kWh/m3	111%	Liquid	0,67
Biodiesel	Fats and oil from soy bean, waste, cooking oil, etc.	9,241 kWh/m3 for B100	9,891 kWh/m3 for B100	103% for B100 and 109% for B20	Liquid	0,812
Compressed Natural Gas(CNG)	Underground reserves	1,309e-5 kWh/g	1,45e-5 kWh/g	119,68 g has 17.3% of the energy in 1 l of gasoline	Compressed gas	0,45
Electricity	Coal, nuclear, natural gas, hydroelectric, wind and solar	N/A	N/A	0,264 kWh electricity contains 3% of the energy in 1 l	Electricity	N/A
Ethanol	Corn, grain and cellulose	5,9 kWh/m3 for E100	6,534 kWh/m3	E100 contains 66%	Liquid	0,562
Hydrogen	Natural gas, methanol and water electrolysis	3,33e-5 kWh/g	3,941 e-5 kWh/g	119,6 g has 44.4% of the energy in 1 l of gasoline	Compressed gas or liquid	4-8 $/kg 2005 2-3$/kg expected 2015
Liquified Natural Gas (LNG)	Underground reserves	5,776 kWh/m3	6,556 kWh/m3	64%	Cryogenic liquid	3 $ per 293 kWh [EIA]
Methanol	Natural gas, coal or woody biomass	44,254 kWh/m3	5,04 kWh/m3	49%	Liquid	0,22 $/l [Methanex]
Propane	By-product of petroleum refining or natural gas processing	6,566 kWh/m3	7,06 kWh/m3	73%	Pressurized liquid	25,06 c$/l

Fig. 2.7: Characteristics comparison for different fuels [5]

is very small if hydrogen does not reach the stoichiometric proportion needed to explode (4000 ppm). If the leak occurs indoors, the risk is remarkably higher, therefore, hydrogen and oxygen sensors should be always used. If finally the hydrogen leaked explodes, it will only happen when the hydrogen is present in high concentrations and a spark ignites it. The flame produced by hydrogen is hardly visible and emits less radiation than the generated by gasoline [34].

But the hydrogen has also got positive safety characteristics. Hydrogen is not toxic, as gasoline or derivates and the explosion energy by unit of stored energy is the smallest compared to the rest of fuels. These characteristics, summed up with the high efficiency of the fuel cells which generate electric power with hydrogen as fuel makes hydrogen an interesting possibility as a future energy vector.

2.2. Electrochemical systems

As mentioned earlier, this Thesis will focus on hybrid electric systems in which all the power sources have an electrochemical basis, and no conventional energy sources such as internal combustion engines are included.

2.2.1. Fuel cells

Even though fuel cells are nowadays on the focus of researchers, governments and private companies as a possible substitute of conventional energy systems, this technology is known since the 19^{th} century. It was Sir William Grove who in 1839 first presented a fuel cell formed by two platinum electrodes submerged in an acid solution and discovered that an electric current flowed between the electrodes [35]. However, it was not until the 20^{th} century that Nernst presented the thermodynamic laws which defined its operational principle and setup the first operative fuel cell, based on solid oxides and ceramic.

There are different technologies for fuel cells: polimeric, ceramic, molten

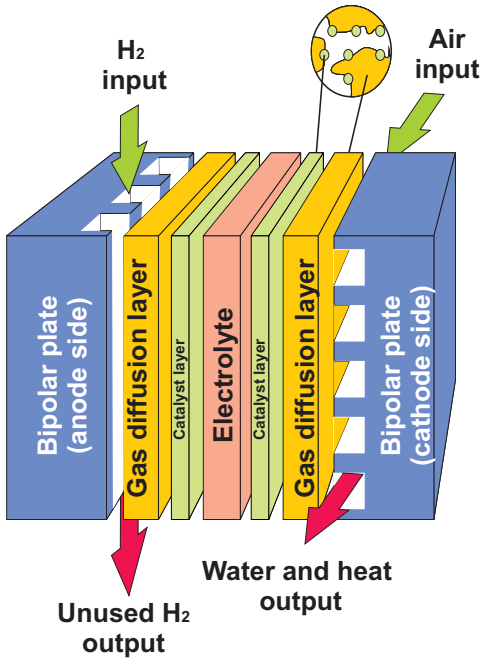

Fig. 2.8: Components of an individual fuel cell

carbonates, phosphoric, etc. Each of these technologies is especially appropriate for a particular application. For example, polimeric based fuel cells are convenient for transportation due to the fast start-up, ceramic fuel cells are useful in high power stationary applications whilst direct methanol are used in small portable systems [36]. This Thesis is more focused on the transportation application, therefore, emphasis is done in polimeric based fuel cells. An overview of other fuel cell technologies can be consulted in [35].

2.2.1.1. The stack and operational principle

The heart of fuel cells is the fuel cell stack, which is the element which converts the chemical energy to electricity. The stack is a series combination of individual cells in which the reaction takes place. The components of each cell: electrolyte, electrodes (anode and cathode), catalyst layer and gas diffusion layer are pointed out in Fig. 2.8.

For polimeric based fuel cells, really called proton exchange fuel cells (PEMFC), the fuel which must be supplied is hydrogen and oxygen (or air). The hydrogen is in gaseous state and enters the fuel cell through the canals of the bipolar plates (anode side), which allows the gas to distribute evenly

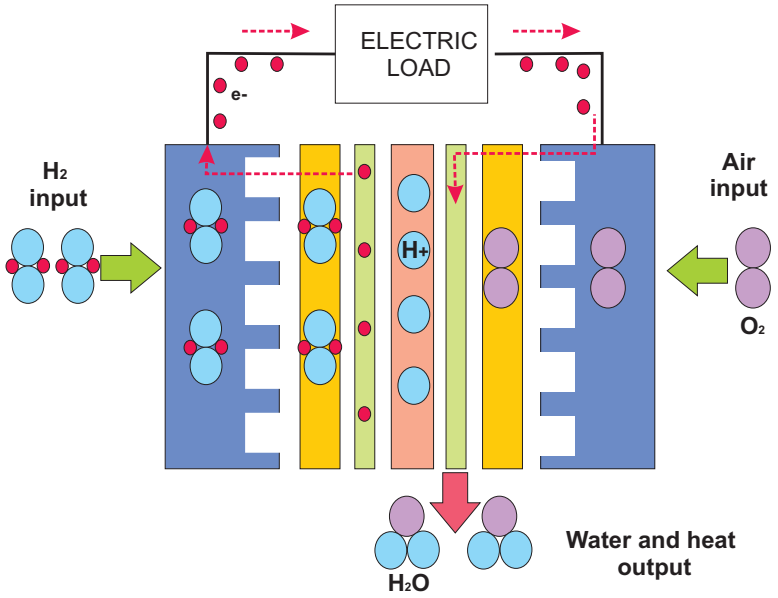

Fig. 2.9: PEMFC operation principle

through all the surface of the gas diffusion layer. On the other side, the oxygen or air does exactly the same thing on the cathode side. Once both gases have gone through the gas diffusion layer, they reach the catalyst layer, which is platinum based for PEMFCs. The catalyst of the anode side dissociates the hydrogen molecule in protons and electrons (see Fig. 2.9). The electrons flow through the electric load to which the fuel cell is connected whilst the protons go through the polymeric electrolyte until they reach the cathode side. Once on the catalyst layer of cathode side, the hydrogen protons react with the oxygen present in the air and the electrons which leave the electric load, generating water and heat.

$$\begin{aligned} 2 \cdot H_2 &\rightarrow 4 \cdot H^+ + 4 \cdot e^- \\ O_2 + 4 \cdot e^- + 4 \cdot H^+ &\rightarrow 2 \cdot H_2O \end{aligned} \tag{2.1}$$

In order to ensure a correct reaction and operation, the bipolar plates should be light, resistant, conductor of electricity and impermeable to gases, in order to ensure a correct distribution of gases through the gas diffusion layer. The most common materials are graphite or metal [37].

The gas diffusion layers help to diffuse the gas to the catalyst layer, conducts electrons from the anode and to the cathode and extracts the water produced in the cathode. To facilitate the water and gas flow, the gas diffu-

sion layer can be made impermeable by adding Teflon.

The catalyst layer is not, as the bipolar plates or the gas diffusion layer, a "solid" structure, but a deposit of catalyst particles on the gas diffusion layer. The reason for this is that the catalyst width is not relevant for the reaction which takes place. Only the surface which the catalyst layer exposes to the gas diffusion layer can alter the reaction (a larger surface is always preferable). The most common material is platinum, but other transition metals such as palladium and titanium could be applied. The use of a precious metal such as platinum increases the manufacture cost, and is therefore, another reason to keep low the amount of platinum used.

One of the distinctive elements in a fuel cell is its electrolyte. As we are focusing on the PEMFC, the electrolyte is a polymeric membrane which is normally made out of Nafion (really it is a derivate of Teflon and Nafion is the commercial name given by its manufacturer). This polymeric membrane should be chemically and thermally stable, in order to endure the action of oxidative agents, as well as relatively high temperatures. The membrane should also be proton conductive, to carry the hydrogen protons from the anode to the cathode. To achieve this the membrane must be humid, something which is possible due to the water generation on the cathode side. However, humid does not mean flooded. A flooded membrane could lead to a short-circuited fuel cell, so the water management is an important issue in fuel cells. Even if the membrane should be only proton conductive, there is a small amount of electrons and hydrogen molecules which directly crosses the membrane to reach the cathode, but no reaction occurs, so the output voltage of the cell will be lower than expected.

In the fuel cell argot, instead of talking about electrolyte, catalyst, etc. it is very common to call the assembly electrolyte+both catalyst layers Membrane Electrode Assembly 3 (MEA 3). If the both gas diffusion layers are included to the previous assembly, it is called Membrane Electrode Assembly 5 (MEA 5).

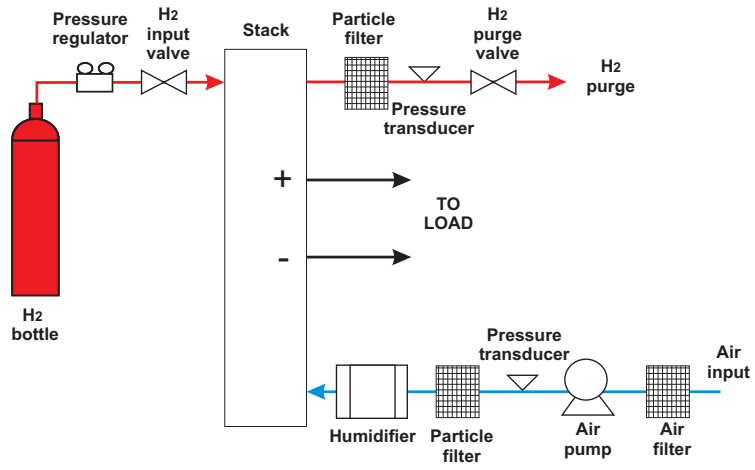

Fig. 2.10: PEMFC auxiliary systems

2.2.1.2. Auxiliary systems

At the beginning of this section we said the stack was the central element of the fuel cell. However, to ensure its correct operation other systems need to be included, as explained in [37]. These systems supply the gases, cool the stack, etc. Fig. 2.10 presents these auxiliary systems for a simple PEMFC.

The hydrogen gas is stored in a compressed bottle at high pressure (up to 200 bar), but lowers it pressure to about 10 bar through the pressure regulator. The hydrogen input valve is controlled by the fuel cell control system and the user interface software. 10 bar is still not low enough, so the fuel cell may have its own pressure regulator to reduce it further. Not all the hydrogen supplied to stack reacts, so the fuel cell control system purges periodically the unused hydrogen. This unused hydrogen can either be expelled to the atmosphere or be reused at the hydrogen input.

For the air flow system, the air is taken from the surrounding atmosphere; therefore, it needs to be filtered in order to avoid particles entering the fuel cell stack. To keep the fuel cell stack adequately supplied with oxygen, the air pressure is increased with an air pump. The pressure is measured through a pressure transducer and the air is humidified before entering the fuel cell cathode.

It is not included in Fig. 2.10, but fuel cell systems can also present a

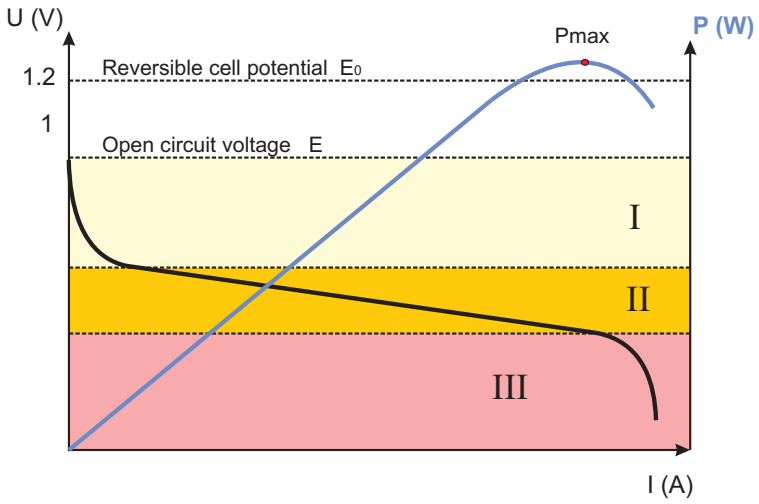

Fig. 2.11: PEMFC characteristic curve

blower or fan. With this element the fuel cell stack is cooled, in order to keep the fuel cell stack in its operating temperature range. The fan duty cycle is controlled by the fuel cell control system, which increases the fan duty cycle when the temperature reaches a certain threshold.

Apart from these auxiliary systems used to keep the fuel cell in correct and secure operating conditions, the electric connection of the fuel cell to the load can be done directly. However, the fuel cell output is an unregulated voltage, so a power converter is normally connected in between. The power converter nature (DC/DC or DC/AC) as well as its topology will depend on the final application. Also, the fuel cell is a power source which generates power, but does not sink it. Hence, a power diode can be connected at the fuel cell terminals to reject any power reflux.

2.2.1.3. Characteristic curve

The ideal voltage of an individual cell is 1.2 V, however, if the voltage is measured when the cell is at open circuit, the voltage will not surpass 1 V. This difference is due to the fact that ideally no reaction occurs when the fuel cell is at open circuit, but really there is a small consumption of reactants which cause this voltage drop.

The fuel cell voltage decreases for increasing load current, but it is not

a completely linear dependency. For low currents the voltage is a nonlinear curve (area I in Fig. 2.11) which is due to the activation polarization. This activation polarization is the overpotential which must be overcome before the reaction occurs. This phenomenon takes place both at the anode and cathode, but is dominant at the cathode side.

At medium currents, the voltage follows a linear evolution (area II in Fig. 2.11). This voltage drop is due to the ohmic polarization. Due to the linear nature this phenomenon can be represented by a resistance, which includes the resistance to the electrons flow from the catalyst layer to the electric load and to the protons flow from the anode to the cathode through the membrane.

Area III in Fig. 2.11 is due to the concentration polarization, present at high load currents. It is caused by the impossibility to increase the reactants concentration in order to increase the fuel cell output current.

Taking into account all these voltage drops, the final fuel cell voltage is:

$$U_{FC} = E - \Delta U_{act} - \Delta U_{ohm} - \Delta U_{conc} \tag{2.2}$$

2.2.2. Batteries

The principle in which the batteries are based was discovered by Luigi Galvani in 1780. He demonstrated with two different metals acting as electrodes and a frog as electrolyte that current could flow through the frog. But the battery as we know it was setup by Alessandro Volta in 1800. He developed the idea presented by Galvani by connecting the cells in series, so as to obtain a higher voltage. The batteries began to be used industrially with the Daniell battery in 1836, as well as an energy source for the telegraph.

Depending on the material from which the electrodes are manufactured and the electrolyte used, batteries present different characteristics. The most traditional battery is the lead-acid battery, followed by the nickel-cadmium, nickel-metal hydrides and lithium based batteries (lithium-ion or lithium-polymer). These are the basic and most commonly used batteries, but there is a wide spectrum of batteries which present more unusual materials, such as vanadium, silver, zinc, etc. In this Thesis we are going to work with an

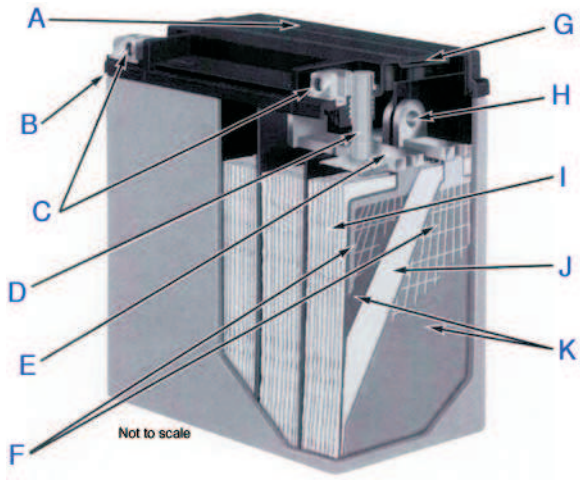

Fig. 2.12: Parts of a commercial battery [6]

Exide-Tudor lead-acid battery especially manufactured for traction purposes.

2.2.2.1. Parts and operational principle

Some parts of the battery resemble to those of the fuel cell, which is inevitable due to the fact that both are electrochemical systems. However, there is an outstanding difference between fuel cells and batteries. The difference lies in the supply of reactants, which can be done externally (fuel cells or flow batteries) or can be found inside the system casing (battery case). For the fuel cell case, it will generate electric energy indefinable whilst hydrogen is supplied to the anode and oxygen to the cathode. However, a battery has a finite time during which it can supply energy due to the fact that the reagent depletes when the discharge time is due.

Fig. 2.12 shows the elemental parts of a battery.

- A: Valve to allow the exit of gasses which can be produced during overcharging.
- B: Battery case.
- C: Positive and negative terminals.
- D: Connector between plates to terminal.
- E: Positive top plate.

- F: Positive and negative plates.
- G: Top sealing.
- H: Negative top plate.
- I: Plate separating material.
- J: Plate separator (separates the positive and negative plates.)
- K: Positive and negative plates.

The battery positive and negative plates can be mounted on a same plate, called bipolar plate. The positive plate is made out of lead dioxide, whilst the negative plate is a sponge texture lead. In between the positive and negative plates we can find the electrolyte. Even if in the batteries commonly used in vehicles for auxiliary load supply, the electrolyte is liquid (dilute sulphuric acid), batteries for traction purposes normally use non-liquid electrolytes [38]. This non-liquid electrolyte commonly has a gel or AGM (Absorbed Glass Matt) structure, which avoids the loss of electrolyte, which would negatively affect the battery operation.

The reactions which take place in a battery are different, depending if it is a charge or discharge process. For a discharge process, Fig. 2.13, the positive terminal reacts with the sulphate ions present in the electrolyte to produce lead sulphate. The sulphate ions of the electrolyte also react with the lead dioxide of the negative electrode to also produce lead sulphate. Therefore, both plates produce lead sulphate whilst the electrolyte looses the sulphuric acid and increases its water content.

For the charge process, an external power source is connected between the terminals of the battery. The initial state is the one left when the battery is discharged, that is, both electrodes are lead sulphate. With the charge process, the sulphate present in the electrodes return to the electrolyte, which recovers its sulphuric acid nature. And the positive electrode changes from lead sulphate to lead whilst the negative electrode changes to lead dioxide. Further information can be found in [39].

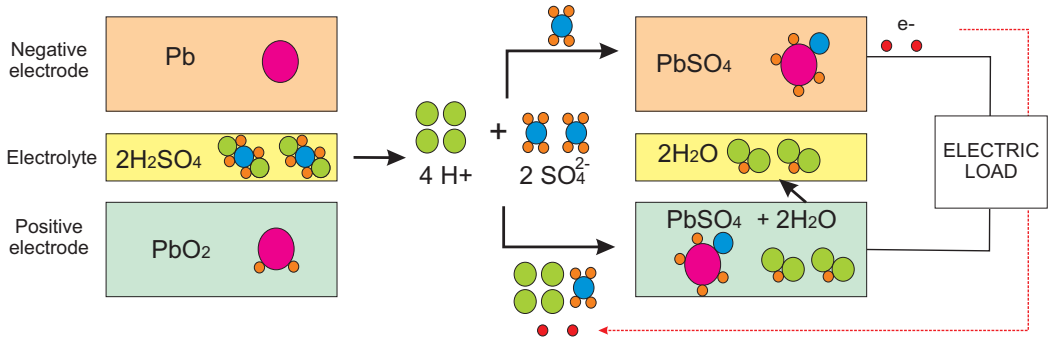

Fig. 2.13: Reactions during the battery discharge process

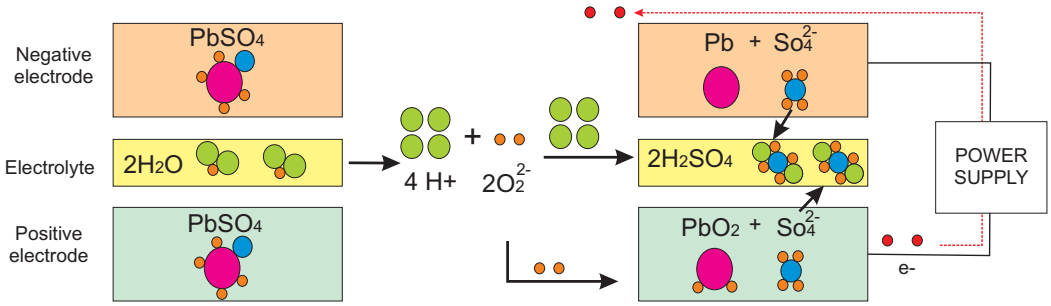

Fig. 2.14: Reactions during the battery charge process

To avoid overcharge it is desirable to follow the recommendations made by the manufacturer. If not, gasification may take place. This gassing phenomena happens when there is no more lead sulphate on the electrodes to react, as they are already lead (positive electrode) or lead dioxide (negative electrode). So oxygen is formed at the negative electrode and hydrogen at the positive electrode. In traditional (flooded) batteries, these gasses leave the battery casing, causing the loss of electrolyte. But nowadays, traction batteries are sealed, so gasses are trapped inside the casing, to allow its recombination to water.

Other problems which may be present in a battery are sulphatation and corrosion [40]. Sulphatation takes place when a battery is kept discharged during a long period of time, causing the lead sulphate present in the electrodes to form crystals, which are difficult to reverse to lead or lead dioxide. The corrosion takes place on the electrodes, increasing the internal electric resistance of the battery. Also, large crystal will be formed, reducing the active surface and the battery capacity.

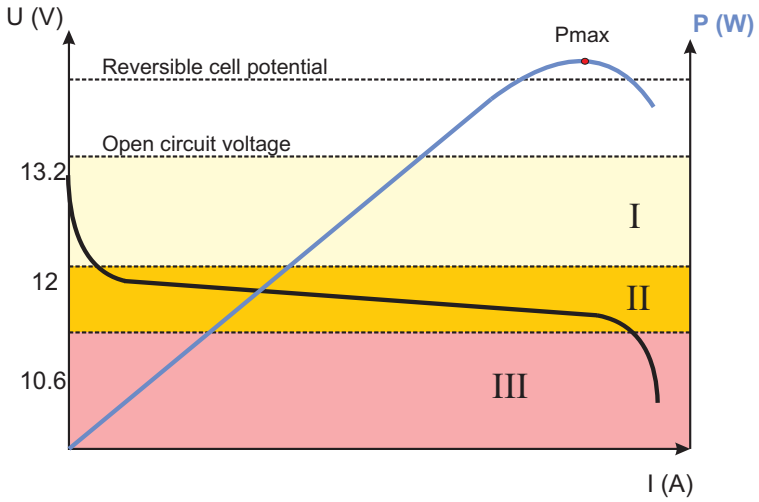

Fig. 2.15: 12 V Lead acid battery characteristic curve

2.2.2.2. Characteristic curve and principal variables

The characteristic curve of a battery is very similar to the one obtained for a fuel cell. Fig. 5.1 presents the characteristic curve for a 12 V battery module. The same three areas defined for the fuel cell: activation, ohmic and concentration polarizations can be also observed for the batteries.

But this characteristic curve does not completely define a battery. To know the rated battery discharge duration at the rated current it is necessary to define the battery capacity in A·h. For example, normally the principal characteristics are given as: 12 V, 100 A·h (20 h) lead acid battery. This means that the battery is capable of discharging during 20 h if the discharge current is $100/20 = 5$ A.

Other particular variables used for batteries are:

- Open circuit voltage (OCV): Voltage measured in open circuit at the terminals of the battery after a certain relax time has gone by.
- State of charge (SoC): Remaining battery capacity, measured as a percentage of the rated capacity.
- State of health (SoH): It reflects the general condition of the battery, as well as the ability to follow particular loads when compared to a fresh battery.

- Depth of discharge (DoD): Amount of energy extracted from the battery. It is normally expressed as a percentage of the rated capacity.

2.2.3. Ultracapacitors

Ultracapacitors are energy storage systems which belong to the family of capacitors. Conventional capacitors store energy by collecting positive charges on one electrode and negative charges on the other electrode, with an electrolyte in between. This charge separation is responsible for the potential created between both electrodes. However, ultracapacitors do not use the electrolyte in the same way, they use another technology, electric double layer, which allows them a massive charge separation.

The use of energy storage through electric double layer was first reported in 1957 by H. Becker, who worked at General Electric. The device as we know it nowadays was presented by Robert Rightmire, a chemist at Standard Oil Company of Ohio (SOHIO) at 1962. Another SOHIO researcher, Donald Boos continued in 1970 the research initiated by Rightmire.

2.2.3.1. Parts and operational principle

Ultracapacitors are formed by two metal electrodes (foils, which are not bulky) coated with activated carbon, immersed in an electrolyte and separated by a paper separator, as seen in Fig. 2.16 [7]. Electrons accumulate in one of the electrodes (the one connected to the negative terminal) and attract positive ions of the electrolyte [41]. On the other electrode, positive charges accumulate, attracting the negative electrolyte ions, while current flows through the external load. The separator avoids current from flowing directly between both electrodes and causes the effect of having two charge layers, which is why ultracapacitors are also called electric double layer capacitors (EDLC). Due to the fact that the electrodes are made out of a high porous material which present small diameter pores (order of nm) the charge can be stored in the mircopores at the interface between the electrode and the electrolyte. Moreover, the electrode surface is much larger than, for example, batteries, and can reach $2000 m^2/\text{g}$ [42]. This combination of large surface and small separation between charges allows to reach capacitances of farads

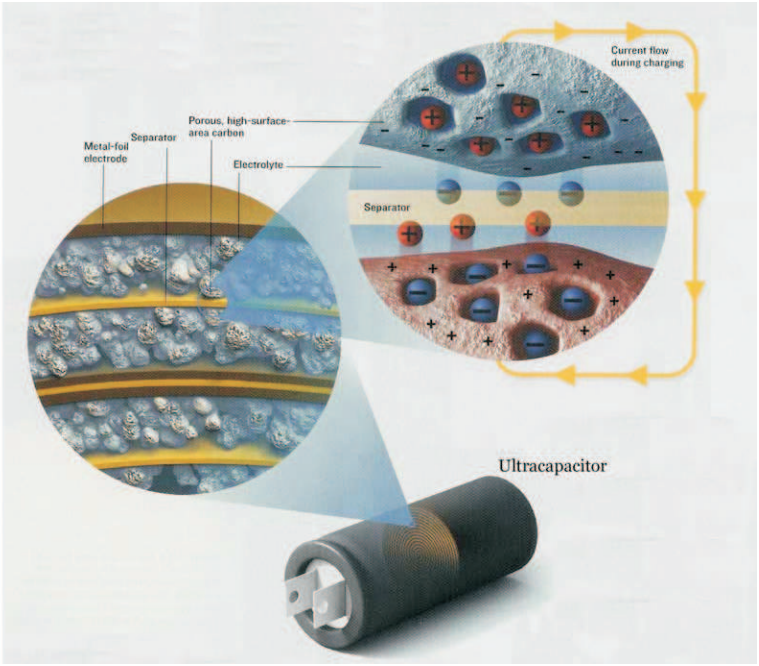

Fig. 2.16: Components and operation of ultracapacitors [7]

and thousands of farads. One of the drawbacks of the small separation is the maximum voltage, which depends on the dielectric breakdown characteristics, and causes ultracapacitors to be low voltage systems (3.5 V maximum).

These operation characteristics define ultracapacitors as high power sources, which are able to supply very high power peaks during very short periods of time. The differences between power and energy densities for different energy storage systems can be consulted in Fig. 2.17.

In addition to high power density, ultracapacitors present a long cycle life and endure deep cycles at high rates for 1.000.000 cycles without severely affecting its characteristics. Moreover, ultracapacitors can be stored during long periods of time and remain near to its original conditions.

Another particular characteristic of ultracapacitors is its small internal resistance, called electric series resistance (ESR). This makes the packaging of ultracapacitors in modules a difficult issue, as the contact and current collector resistances should be kept low enough to allow the ultracapacitor act during high power loads.

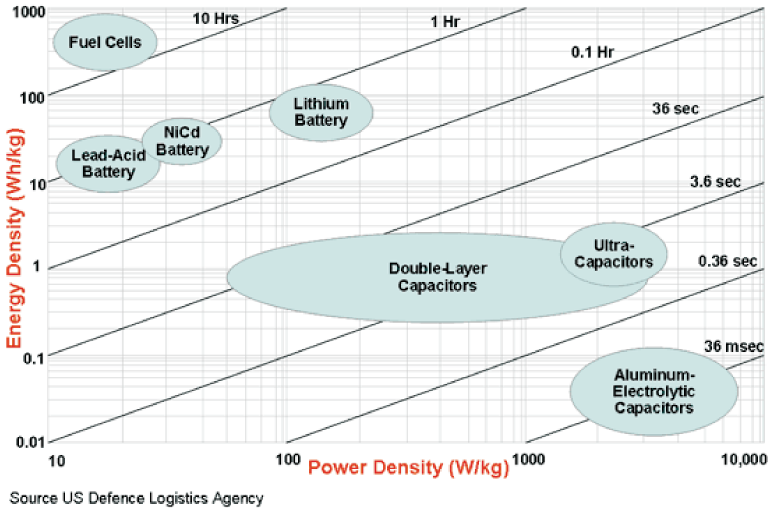

Fig. 2.17: Ragone chart for different energy storage systems

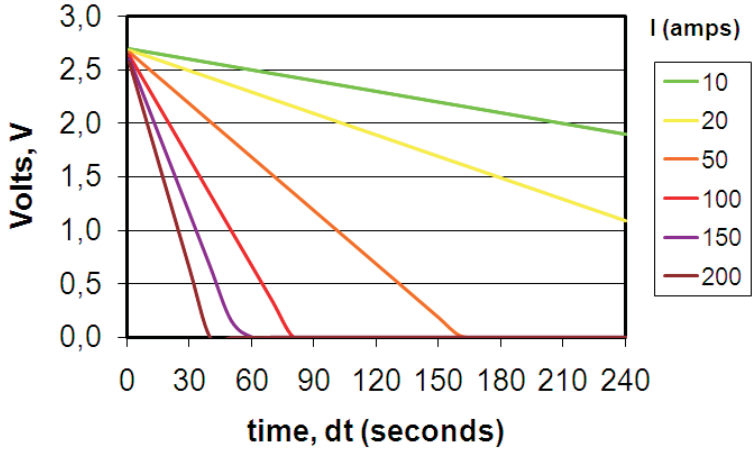

Fig. 2.18: 3000 F Maxwell ultracapacitor

2.2.3.2. Characteristic curve

There is not a unanimity in which is the characteristic curve for an ultracapacitor. However, manufacturers used discharge profiles, as the one shown in Fig. 2.18, which is the discharge profile given by Maxwell Technologies for the 3000 F 2.7 V ultracapacitor.

CHAPTER 3

State-of-the-art

3.1. Introduction

The previous chapter exposed the reasons for the interest and application of hydrogen as an energetic vector and the introduction of electrochemical systems in the stationary and transportation energetic scene. This chapter will deepen and present a critical review of the modeling techniques proposed by other authors for each of the electrochemical systems under study, that is, fuel cells, batteries and ultracapacitors and present test platforms useful for the testing of hybrid energy systems.

3.2. Modeling techniques

As seen in the previous chapter, the operational principle of fuel cells, batteries and ultracapacitors is based on electrochemical phenomena, but other processes, such as thermal, chemical, electric, fluid dynamic, etc. are also present.

If all these phenomena should be taken into account at a time, the modeling process would result too complex and time consuming. When applying modeling and engineering processes, different approaches can be considered, depending on the final use given to the model developed. For example,

fluid dynamic, thermal, chemical and electrochemical approaches are very adequate for the development stage of electrochemical system. But for the application stage, in which the electrochemical system has to interact with the load to which it is connected, an electric modeling of the system could be more adequate. Therefore, in this chapter we will focus on those models more suitable to a seamless integration in an electric simulation tool.

Engineering models would be useless if the numerical values of their parameters could not be determined through measures. For conventional systems (electric machines, combustion engines, transformers, etc.) whose mathematical models are perfectly defined, there are set of established tests, which allow to obtain the characteristics which define the system under study.

Electrochemical systems can be also subjected to a series of tests which allow to model their electrical behavior. Unlike conventional systems, the structure and mathematical models are still not universally defined, nor the test procedure or parameter obtention univocally established. These tests can be carried out either in the time or frequency domain. One of the most extended time domain test is the current interruption test whilst the frequency domain test the electrochemical impedance spectroscopy.

3.2.1. Time domain tests

3.2.1.1. Current interruption

The current interruption test is a time domain test in which the system under study is kept at its operation point (constant current load) until it reaches stationary state. Once reached, the current load is abruptly interrupted, allowing to study the voltage evolution, depicted in Fig. 3.1. Because electrochemical systems operate in direct current (dc), this test is carried out applying a dc current and measuring the dc voltage.

It can be observed that the (discharge) current interruption causes a voltage increase until it reaches the open circuit voltage. This voltage increase is vertical during the instants after the current interruption, but changes to nonlinear until it reaches the open circuit voltage. The step voltage increment is due to ohmic voltage drop and can be represented by a resistance.

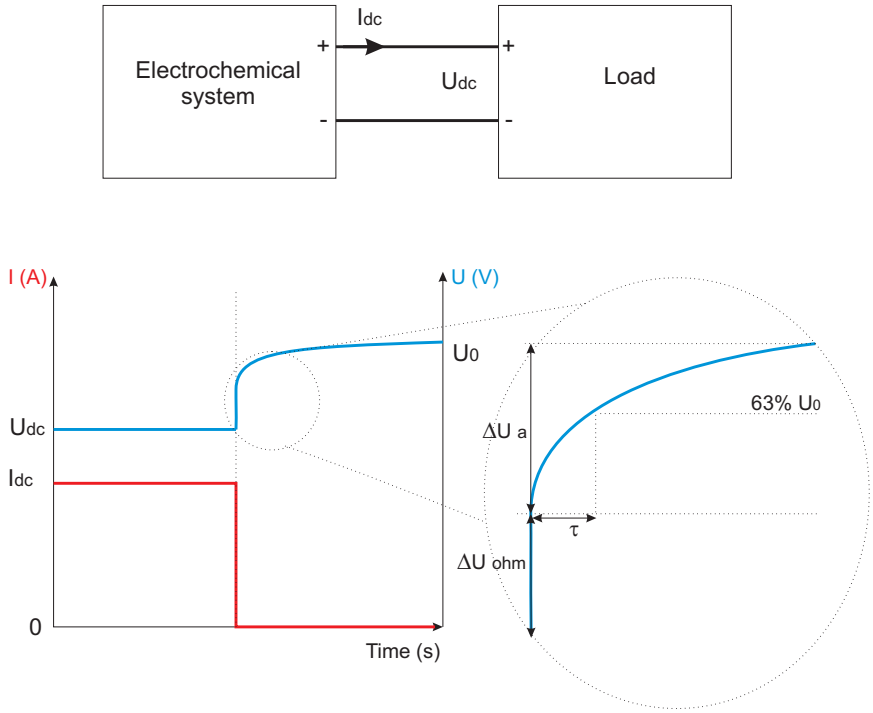

Fig. 3.1: Current interruption test

The nonlinear part can be approximated by a capacitor in parallel with a resistance (with a time constant τ). This RC network reproduces the behavior of the double layer capacitor present in electrochemical systems at the interface of the electrodes and electrolyte. The resistances and capacitance can be calculated as:

$$\begin{aligned} R_{ohm} &= \frac{\Delta U_{ohm}}{I} \\ R &= \frac{\Delta U_a}{I} \\ C &= \frac{\tau}{R} \end{aligned} \tag{3.1}$$

If this test is carried at different current loads I_{dc}, it is possible to analyze the dependency of each parameter with the current. Known these parameters, an equivalent circuit, depicted in Fig. 3.2, can be defined. The equivalent circuit represented includes the internal voltage E, which will depend on the electrochemical system.

The advantage of this modeling technique is its simplicity, both in setup and control. However, there are several drawbacks. The first one is that this

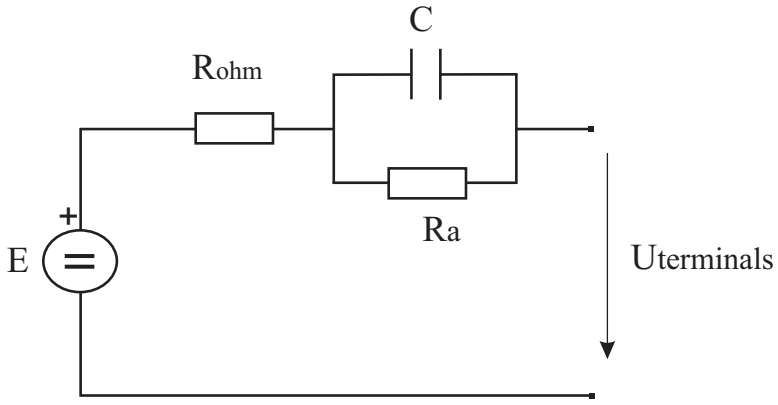

Fig. 3.2: Equivalent circuit obtained from the current interrupt test

a lumped equivalent circuit, which, for example, does not include the inductive behavior at high frequencies or the concentration voltage drop present during high load currents. Moreover, the model precision depends heavily on the correct identification of the point in which the voltage evolution changes from vertical to nonlinear. An imprecise calculation will cause the incorrect calculation of the voltage drops and the time constant. Finally, this method does not add significant information about the internal processes present in any electrochemical system.

Some examples of the application of this method to fuel cells can be found in [43], [44] and [45]. It can also be applied to batteries, but the test should be carried out for both charge and discharge processes.

3.2.2. Frequency domain tests

3.2.2.1. Electrochemical impedance spectroscopy (EIS)

The two most important differences between current interruption and EIS tests is that, whilst current interruption is carried out in the time domain and with direct current, EIS is a frequency domain test which needs the application of alternating current and voltage. One of the similarities is that EIS tests also seeks to calculate the impedance of the system under study. But the most important advantages of frequency domain tests are the richer information obtained and the simpler data processing (if the adequate software is used).

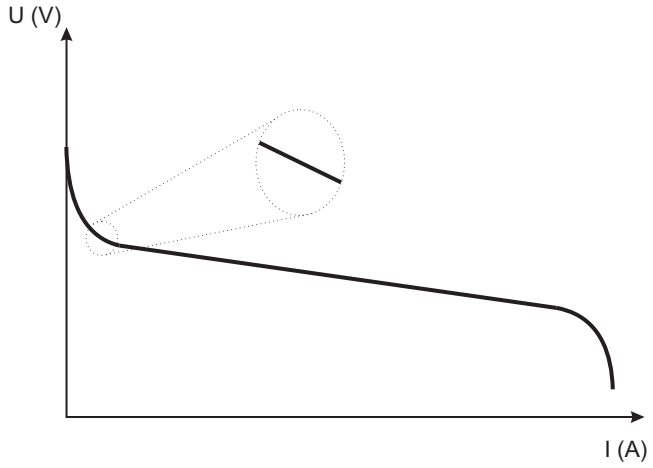

Fig. 3.3: Linearity of the characteristic curve

Electrochemical systems present a nonlinear characteristic curve. For example, Fig. 3.3 presents a fuel cell characteristic curve, which is nonlinear with a large signal analysis, but can be linearized if small variations are taken into account, as done with small signal analysis. To keep linearity during the tests, the ac signals applied are small enough(e.g. 5 % of the rated voltage).

During EIS tests a small ac excitation signal (either current or voltage) is applied to the electrochemical system. This excitation signal will cause the system to react, generating an ac voltage (if the excitation signal is current) or ac current (if the excitation signal is voltage). The ac excitation signal can be applied with a fixed (not usual) or variable frequency, which in the variable case can be programmed as a sweep.

If the ac excitation signal is current, it is said to be a galvanostatic mode EIS, whilst if it is a voltage signal it is called a potentiostatic mode. The selection criteria to chose between one mode or another is frequently the control mode of the system under test. For example, the fuel cell current is more easily controlled than the voltage. Hence, it would be easier to apply a galvanostatic (current control). Supposing galvanostatic mode EIS (current control),the excitation signal can be expressed as:

$$I\left(t\right) = I_0 \cdot \cos(\omega \cdot t) \;\; ; \;\; \omega = 2 \cdot \pi \cdot f \tag{3.2}$$

Where I_0 is the signal amplitude and f the signal frequency. Supposing that the system displays a linear behavior, the resulting ac voltage is:

$$E(t) = E_0 \cdot \cos(\omega t - \varphi) \tag{3.3}$$

φ is the phase at which the current signal is shifted, whilst E_0 is its amplitude. Known both the voltage and current, the complex impedance can be calculated as:

$$Z = \frac{E(t)}{I(t)} = \frac{E_0 \cdot \cos(\omega \cdot t - \varphi)}{I_0 \cdot \cos(\omega \cdot t)} = Z_0 \cdot \frac{\cos(\omega \cdot t - \varphi)}{\cos(\omega \cdot t)} \tag{3.4}$$

Electrochemical systems generate direct current, therefore, it is unavoidable to have both dc and ac signals while carrying out EIS tests. The dc level is used to keep the electrochemical system at its operation point, but it is not considered for the impedance calculation, in which only the ac signals are involved. This implies that the dc level must be rejected before the ac impedance is calculated. A diagram explaining the whole process is presented in Fig. 3.4.

EIS tests can be carried out with off-the-shelf equipment: electronic load, signal generator and voltage and current transducers. However, the subsequent impedance calculation and model extraction is time consuming and complex. Therefore, it is recommendable to use an impedance analyzer, which generates the excitation signal and calculates the complex impedance by measuring the current and voltage.

However, impedance analyzers are equipments more focused to test passive elements, which can be correctly characterized with the 60 mA current and 45 V threshold. However, the current limit is clearly insufficient for active elements, which can reach hundreds of amperes. This low current threshold forces the use of other equipments along with the impedance analyzer, such as potentiostats, which are able to absorb higher dc currents. However, potentiostats present a maximum of 100 A (the most expensive equipments, less than 40 A the rest), which is still a low value for testing, e.g. ultracapacitors.

After the EIS test is carried out, the data must be processed. Normally the impedance analyzer includes a software package to do it. The data is

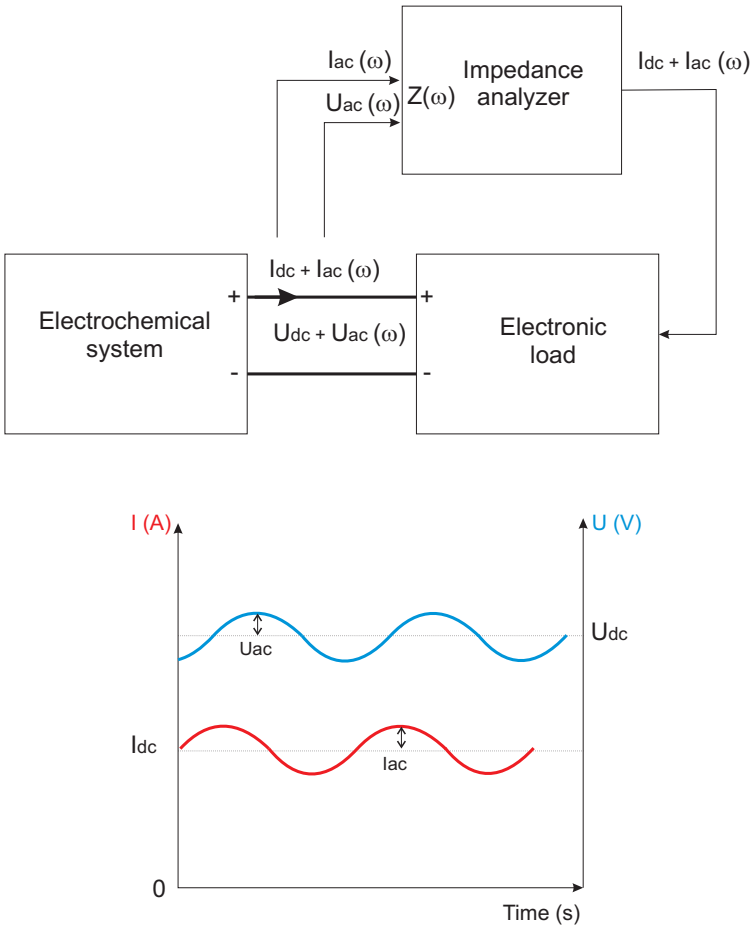

Fig. 3.4: EIS test diagram

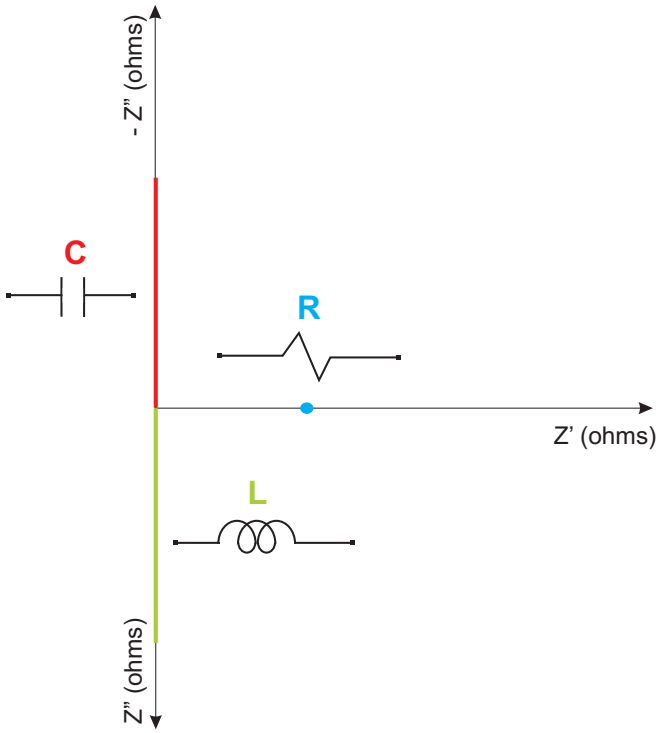

Fig. 3.5: Nyquist plots for ideal elements

rendered in a text file, which is traduced by the software to a Nyquist and Bode plot. Known these two plots, specially the Nyquist plot, the user can define an equivalent circuit, which the programme fits to the experimental results, as shown in Fig. 3.5.

The most frequently used elements are resistances, capacitors and inductances. Fig. 3.5 presents the Nyquist representation for each of these systems. The abscissa axis represents the real part of the complex impedance (Z'), whilst the ordinate axis is the imaginary part (Z"). To facilitate the interpretation of the Nyquist plots, the upper part of the imaginary plot corresponds to the negative imaginary part (-Z").

$$Z = Z' + jZ" \tag{3.5}$$

The resistance is represented by a point on the abscissa axis, with no imaginary part. Ideal capacitances or inductances correspond to vertical lines on the diagram. These type of ideal elements are rarely, if ever, found. It is more frequent to encounter real systems, which include the association of

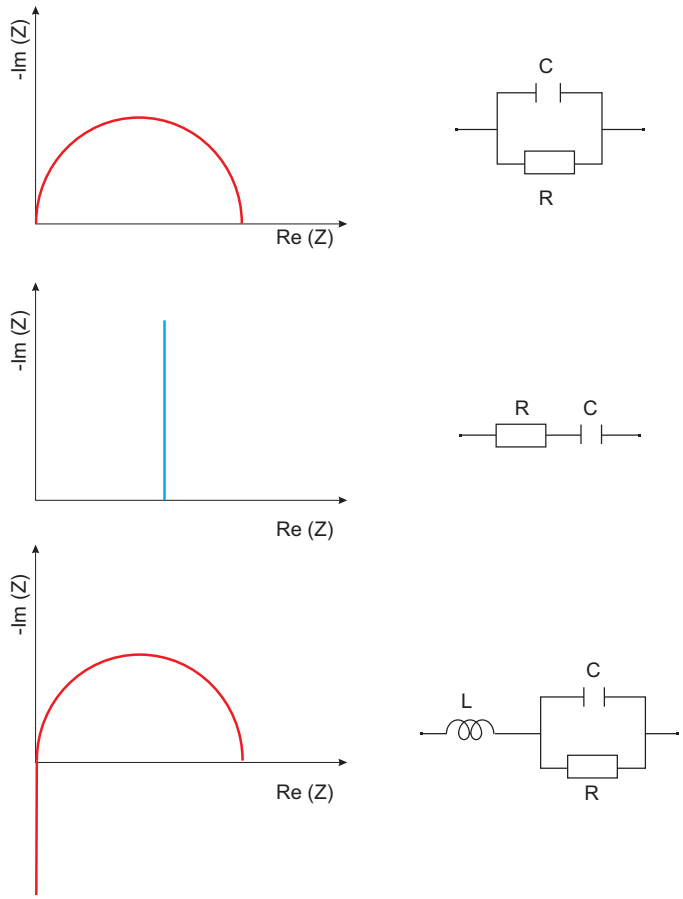

Fig. 3.6: Nyquist plots for combined ideal elements

two or more of these elements, as presented in Fig. 3.6.

For electrochemical systems, classic electric elements (resistances, capacitors and inductances) may not be enough to represent their internal behavior, due to, for example, diffusion phenomena. Most electrochemical systems use porous or rough materials for the electrode manufacture, which affect the diffusion of reactants. As stated by Barsoukov [46], diffusion causes an effect similar to a finite transmission line: the answer of the output to an electric stimulation is delayed, compared to the input. Therefore, the electrochemical system will present a distributed equivalent circuit. The exact impedance cannot be represented as a finite number of equivalent circuits, but for computational sake, it is normally limited to a finite number.

In order to represent this distributed effect, it is possible to find distributed elements, such as infinite and finite Warburg impedances, constant

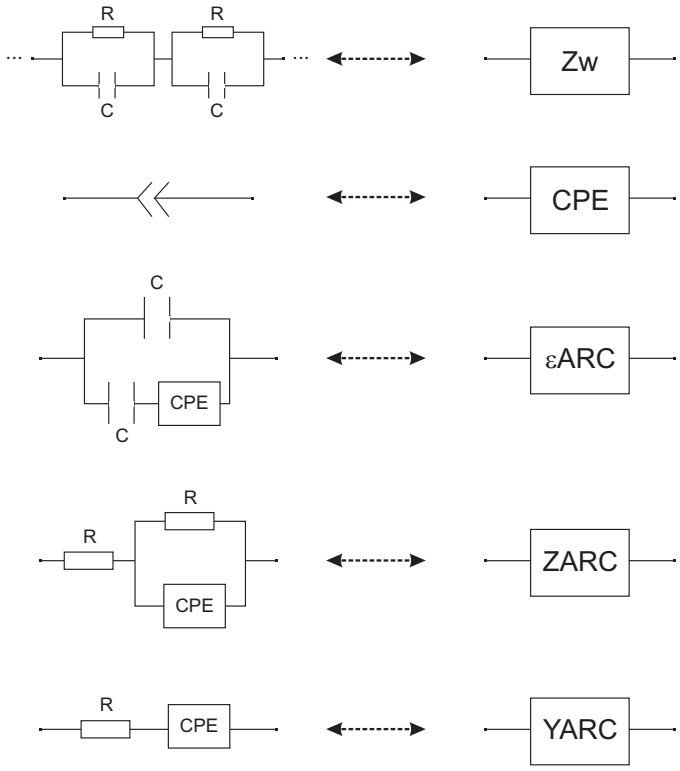

Fig. 3.7: Nyquist plots for diffusion elements

phase elements, ZARC or YARC, among others. The finite Warburg (Z_w) impedance does not correspond to an ideal impedance, such as resistance, capacitance or inductances. It is therefore simulated through an equivalent circuit of distributed RC networks, which can have a finite or infinite number of RC networks.

Another diffusion element is the constant phase element CPE. It can be used combined with other elements. When used in parallel with resistances it can reproduce a depressed semi-circle with the center lower than the abscissa axis. The CPE-R with another resistance in series result in a ZARC (ARC in the Z plane) element. The YARC (ARC in the Y plane) is obtained with the series connection of a CPE and resistance, as depicted in Fig. 3.7. This CPE element can also represent the electrode roughness, due to the fact that electrodes may present a fractal dimension (between 2 and 3 dimensions). It is also considered to represent the inhomogeneous distribution of reactants on the surface or the varying thickness and composition [46].

3.3. State-of-the-art of the modeling of electrochemical systems

3.3.1. Fuel cells

As commented earlier, there are a series of test methods which can be applied to characterize a fuel cell. A revision of these methods was done by Page [47] and Wingelaar [48].

One of the classic models, presented by Amphlett [49] in 1996, is a mechanistic model which takes into account mass and heat transfer in a PEM fuel cell. Later, in 2002, Pukruspan [50] presented a more complete model which included models for the auxiliary systems (compressor, etc.) and used the mass conservation principle and thermodynamic equations to calculate the flow of reactants through anode and cathode. It is an interdisciplinary model, which is more focused on the fuel cell system, rather than on the fuel cell stack.

Electric models are normally more focused on the fuel cell stack model, which is the element which generates the electric power. A classic model for the fuel cell stack is the one developed by Larminie [35] in 2000 and developed by Pathapati [8] in 2005. Both authors used models which included equivalent circuits, as the one depicted in Fig. 3.8, which were able to reproduce the fuel cell electric behavior. The equivalent circuit is the same as the one obtained by current interruption, that is, a lumped equivalent circuit. Despite the fact that Pathapati presents a dynamic model, it is validated with a nearly steady state current profile, so no information about the model behavior during abrupt loads is given.

In 2005 Wang presented a dynamic model programmed in Matlab/Simulink and PSPICE [51]. The equivalent circuit presented is the same as the Larminie and Pathapati circuit. But Wang carried out a series of experimental tests which allowed him to obtain the dependency of each parameter (resistances, voltage, etc.) with current and temperature. However, he did not mention the tests he carried out to obtain these relationships, so even though it is a highly referenced paper, it still has to prove how parameters were obtained.

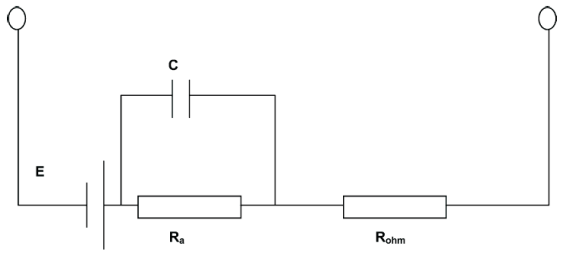

Fig. 3.8: Equivalent circuit presented by Pathapati and Larminie [8]

Moreover, he did not include a temperature model, even though temperature is a key parameter which influences the internal voltage of a fuel cell. Other authors, as Zhang [52] and Soltani [53] do include it. In comparison to Pathapati, Wang did apply a dynamic current profile in order to validate the model voltage dynamically.

The development of more detailed equivalent circuits needs EIS tests, such as those applied by Yuan in [54] and [55]. An analysis of the application of EIS to fuel cells was done by Parthasarathy in [56].Yuan presented the experimental procedure for the application of EIS tests for individual cells and stacks. He discussed which should be the relationship between the ac and dc signal amplitude. He investigated ac signals with an amplitude between a 1 and 15 % of the dc signal amplitude and concluded that for amplitudes smaller to a 5 % the data points were too scattered due to noise, whilst amplitudes larger than 5 % distorted the Nyquist plot at low frequencies.

He also mentioned two different equivalent circuits which could be fitted to the data obtained after the EIS tests, but did not present its equations or justify the election of those parameters. The most striking difference with the circuit mentioned up to this point is the substitution of the capacitors by constant phase elements CPE. However, he did not demonstrate the suitability of its use compared to a capacitor. Finally, he did not validate the circuits mentioned as his work is more centered on the EIS tests itself, rather than on the obtention of a dynamic model.

Other authors, as [9] and [57] keep the capacitor, but include the diffusion in the models by adding a Warburg impedance in series with the resistance of the RC network, as shown in Fig. 3.9, forming a so called Randles circuit.

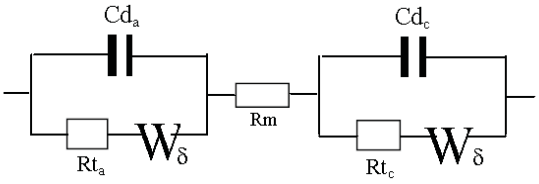

Fig. 3.9: Equivalent circuit presented by Garnier and Laffly [9]

Similarly to the CPE, the Warburg impedance has no electric equation, so it must be fitted to another element which can be described by a single or combined number of electrical components. The Warburg is normally substituted by a series connection of RC networks. The number of RC networks connected in series depends on the user (Garnier [9] used 10). However, this increases the number of differential equations which must be solved to calculate the output voltage.

Other authors which apply EIS to PEM fuel cells are Brunetto, Cooper and Zhu. Brunetto [58] carried out the EIS tests after keeping the fuel cell 5 hours in its operation point, in order to guarantee the fuel cell stationary state. The equivalent circuit is similar to the one used by Garnier, but without the Warburg impedance. He took into account the temperature effect, but did not model it. As commented with Wang, the temperature affects the fuel cell internal voltage, and should therefore be taken into account.

Cooper [10] carried out a revision of the electrical tests which can be carried out on fuel cells, and applied each of them, but did not present a critical comparison. He carried out EIS tests from 1 Hz to 10 kHz and presented the Nyquist plot obtained after tests, in which the fuel cell presented a capacitive behavior at 20 kHz. But other authors, as Zhu [59], actually found inductive behavior at 10 kHz. The equivalent circuit presented by Cooper is a transmission line model formed by resistances and capacitors, as shown in Fig. 3.10.

Other authors develop the fuel cell models as transfer function, as done by Boccaletti [60], Soltani [53] and Yalcinoz [61]. Only Soltani experimentally validated his model.

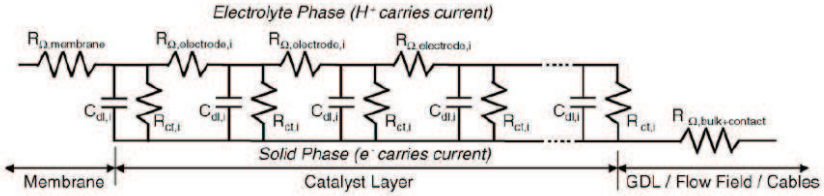

Fig. 3.10: Equivalent circuit presented by Cooper [10]

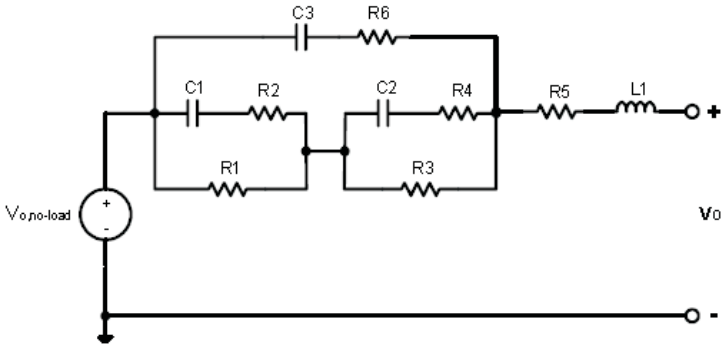

Fig. 3.11: Equivalent circuit presented by Choi [11]

Finally, Choi [11] developed a dc and ac equivalent circuit. The ac equivalent circuit was obtained after EIS tests. He proposes a per-unit system for the fuel cell, by using a base power, voltage and current which is a useful tool when connecting fuel cells to other power electric systems. However, he did not develop the idea by using the inverter as a base voltage transformer or by comparing the different fuel cells he models in per-unit values. Moreover, he did not include a base frequency for the ac equivalent circuit, shown in Fig. 3.11, or experimentally validate the developed model.

As a conclusion, multiple models have been presented for a fuel cell simulation. The equivalent circuits presented generally include similar elements. However, those who have included diffusion elements, such as CPE have not demonstrated its adequacy compared to capacitors. Moreover, of those authors who obtained the models through EIS tests, some studied the temperature effect on the fuel cell impedance, but did not develop a temperature model. This temperature model is necessary to calculate the fuel cell internal voltage. Also, the direct comparison of parameters for similar fuel cells is difficult due to the absolute value approach. This problem could be solved by using a per-unit approach, as done by Choi. However, Choi does not totally

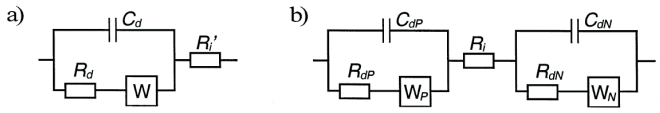

Fig. 3.12: Equivalent circuit presented by Karden [12]

define the base system, as he does not include a base frequency or comment the per-unit approach adequacy when connecting the fuel cell model with other power electric elements.

3.3.2. Batteries

One of the most relevant contributions to batteries was made by Peukert in 1897 [62]. Peukert carried out constant current tests to lead-acid batteries and discovered a relationship between the battery capacity, current and discharge time. This is a useful tool to know, e.g. the remaining capacity after a certain discharge time has gone by. The Peukert equation has been studied more recently by Doerffel [63].

The Electrochemical Energy Conversion and Storage System research group at the ISEA (Institute for Power Electronics and Electric Drives), Aachen University (Germany) is a reference for the modeling of electrochemical systems, specially batteries. In 2000 Karden [12] presented a method for measuring and interpreting battery impedance. They developed their own impedance analyzer and carried out galvanostatic EIS tests during continuous discharge and mini-cycles for different states of charge. They did not focus specifically on the development of an equivalent circuit, however, they did propose the one presented in Fig. 3.12. This figure presents two different equivalent circuits. Both present Warburg impedances, in order to reflect the diffusion at low frequencies. The difference between them is that one includes just one RC network, whilst the other presents two (one RC network per electrode). Later, he extended this analysis to other electrochemical systems [64].

Other authors, such as Tenno studied the relationship between the battery impedance and its characteristics [65]. He used an equivalent circuit similar to the two RC network model presented by Karden. But Tenno did

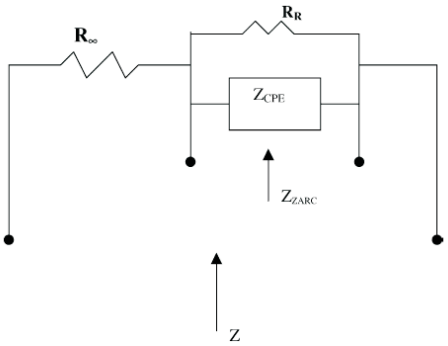

Fig. 3.13: Equivalent circuit presented by Nelatury [13]

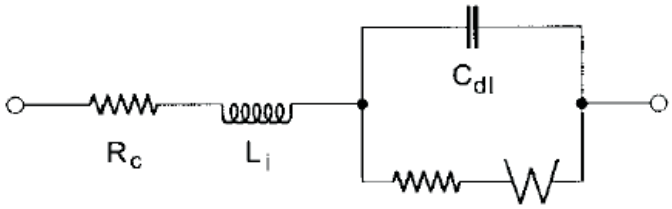

Fig. 3.14: Equivalent circuit presented by Baert [14]

not take into account the diffusion phenomenon.

In 2002 Nelatury [13] presented an equivalent circuit with just one network, but substituted the capacitor by a constant phase element CPE, as shown in Fig. 3.13. The R-CPE combination is also called ZARC, which is the expression he used. However, he did not validate the equivalent circuit presented. Other authors, like Buller [66], also used ZARC elements, but applied to Li-ion batteries.

Baert [14] included an inductance in series with the series resistance and RC network with a Warburg impedance, which is depicted in Fig. 3.14. The inductance he included models the inductance of the conducting path, which he considered constant for any state of charge. He proposed to center the attention on the resonance frequency (frequency at which the battery impedance is purely resistive) because of the slow phenomena on the electrodes, which are unable to follow high frequency excitation. He therefore simplifies the previous equivalent circuit to a series RLC circuit.

Another author who included the inductance is Salkind [15]. He carried

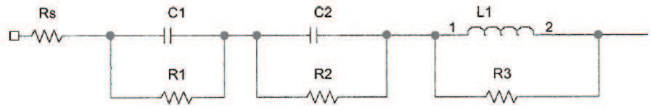

Fig. 3.15: Equivalent circuit presented by Salkind [15]

out EIS tests for two different batteries between 0.65 Hz and 65 kHz. Fig. 3.15 presents the equivalent circuit he proposed. It includes the series resistance and the two RC networks, as well as the inductance, but with a parallel resistance. He did not explain the reason for using this parallel resistance inductance.

In 2005, Thele [67] presented a battery model which was developed in a hybrid frequency and time domain. The reason for this approach is that any model obtained with EIS tests is a good approach for highly dynamic operation, but looses precision when longer processes need to be simulated (transport of sulphuric acid). However, to carry out this hybrid modeling it is necessary to know the thickness, porosity and geometric surface of the electrodes, values which are very difficult to obtain.

Thele, in 2008 developed a voltage behavior for Ni-Mh batteries [16] which can also be applied to lead-acid batteries. The equivalent circuit used is shown in Fig. 3.16 and includes a Warburg impedance in series with the rest of elements. Thele also presented the hysteresis effect of the open circuit voltage (OCV) for Ni-Mh batteries, in which the OCV presents different evolution with the state of charge depending on the nature (charge or discharge) of the process. This hysteresis curve is depicted in Fig. 3.17. Even though the hysteresis effect is not difficult to measure, it is seldom taken into account by most authors. However, the difference between charge and discharge curves of the hysteresis curve is sufficiently different to affect the final model precision.

Finally, there are authors, such as Huet [68], who are exclusively interested on the battery high frequency resistance, which is the battery impedance for the resonance frequency. He concluded that this resistance depends on the state of charge, but not on the current. Moreover, he investigated if this resistance could be an indicator of the battery state of charge, but concluded that it was not a reliable for state of charge monitoring. Huet had previously

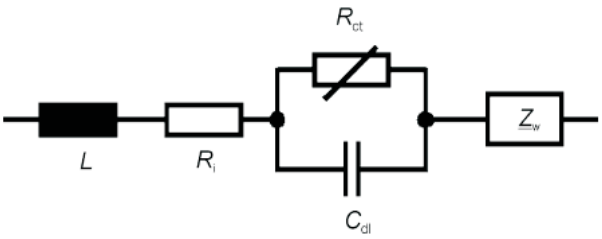

Fig. 3.16: Equivalent circuit presented by Thele [16]

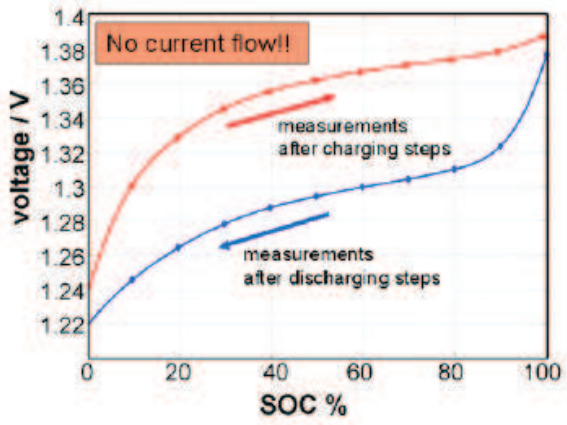

Fig. 3.17: Hysteresis effect on the battery open circuit voltage presented by Thele [16]

(1998) studied different ways to determine a battery state of charge and health [69].

The state of charge measurement, essential for the battery operation life, is a complex task due to all the chemical phenomena which takes place in a battery. Some authors, as Viswanathan [70], investigate the relationship between the charge transfer resistance (part of the RC network) and capacitance with the state of charge. They concluded the charge transfer resistance and capacitance increased for increasing states of charge. This relationship between the capacitance and state of charge was also observed by Tenno [65]. More recently, Hariprakash [71] and Blanke [72] have also studied the use of impedance measurements to calculate the battery state of charge and state of health.

Once all these battery models have been analyzed, it is surprising to find that only Thele takes into account the hysteresis effect on the battery internal voltage. Also, no author comments the difficulties present when comparing the different models for similar batteries. Even for the same technology and depending on the battery capacity and voltage, the parameters can vary orders of magnitude, which makes it difficult to directly compare models. This problem could be overcome with a per-unit comparison, but has not been found in literature.

3.3.3. Ultracapacitors

If compared to batteries, or even fuel cells, the modeling of ultracapacitors is less mature. Some authors which explain the ultracapacitor technology and limitations are Burke [42] and Conway [73]. The modeling techniques are the same as used for batteries or fuel cells, but present particular characteristics, as explained below.

In 2000 Zubieta presented the characterization of ultracapacitors for power electronic applications [17] in the time domain. He modeled the ultracapacitor as a three time-constant circuit formed by capacitors and resistances, as shown in Fig. 3.18. He reflected the dependency between capacitance and

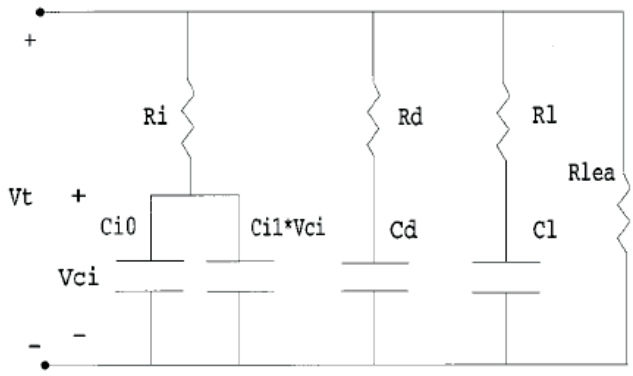

Fig. 3.18: Ultracapacitor equivalent circuit presented by Zubieta [17]

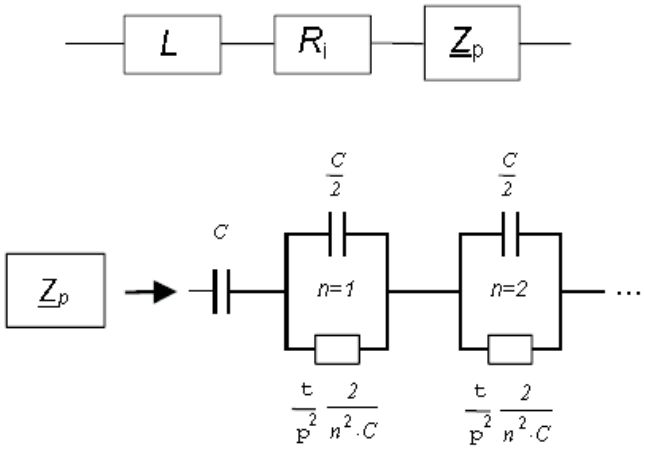

Fig. 3.19: Ultracapacitor equivalent circuit presented by Buller [18]

voltage with variable capacitors. He modeled 470 F and 1500 F capacitors by charging and discharging them and relating each branch parameters to the terminal voltage and time.

In 2001, Buller modeled the dynamic behavior of a 1400 F ultracapacitor through EIS tests [18]. He used an impedance analyzer developed at Aachen for battery testing. The EIS test were galvanostatic, with a frequency sweep between 10 μHz and 6 kHz. He did not specify the ac current amplitude, just indicated it was a small ac current. However, ultracapacitors need large currents to cause a small voltage ripple. He obtained an equivalent circuit formed by an inductance, a series resistance and a series connection of RC networks, as it can be seen in Fig. 3.19.

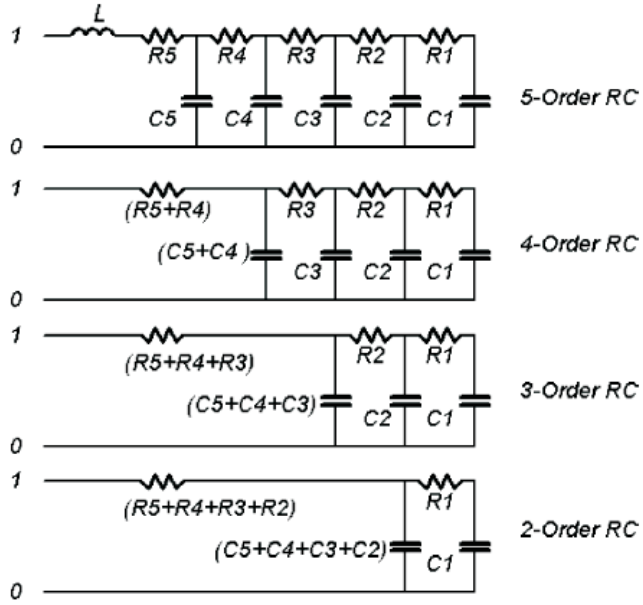

Fig. 3.20: Ultracapacitor equivalent circuit presented by Dougal [19]

During 2003 Lufrano also carried out EIS tests on ultracapacitors. But the main difference is that he did it in potentiostatic mode, with a 20 mV ac voltage excitation. He studied the evolution of the capacitance for different active materials with frequency, but did not specify a particular equivalent circuit.

Furthermore, authors do not agree on the number of RC networks that should be used. Dougal [19] presented the circuit shown in Fig. 3.20 to which he applied an automatic order selection method, changing the circuit order by taking into account different capacitors, depending on the phenomena it reflects. Leaving apart the inherent complexity of the method, the capacitance validation he presented does not follow the measurements trends and differs from one to three orders of magnitude. Moreover, the model voltage is not validated with experimental data.

Lajnef obtained a similar circuit to the one presented by Dougal, but with a fourth order circuit [74]. He used both current tests and frequency analysis. With the current tests he characterized the internal resistance and average capacitance. For the frequency analysis he used potentiostatic EIS tests between 10 mHz and 1 kHz, however he did not detail the ac voltage

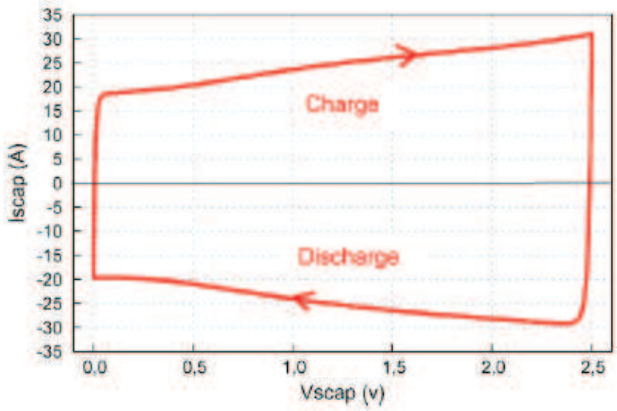

Fig. 3.21: Ultracapacitor voltamogram presented by Lajnef [20]

ripple amplitude. He validated the model experimentally, but recognized the inability of the model to take into account the voltage dependance of the capacitors. He later completed this work verifying the difference in the internal resistance during charge and discharge. Also, he presented the different methodologies used to characterize ultracapacitors, as the voltamogram presented in Fig. 3.21 [20]. He also participated in the study of supercapacitor ageing carried out by Briat [75]. At the end of 25,0000 tests they observed an increase in the ultracapacitor impedance and a loss of capacitance. He later continued with this research in [76].

To consider the temperature effect, Michel [77] observed that capacitance was reduced at freezing temperatures, due to the viscosity of the electrolyte at such low temperatures. He also observed a considerable increase of the internal resistance at these temperatures, for exactly the same reason. This is one of the arguments used by Rafik [21] for not taking into account the effect of temperature on the capacitance for positive temperatures. He used the equivalent circuit depicted in Fig. 3.22 to model a 2600 F with potentiostatic EIS tests. He carried out these tests with a 10 mV ac ripple (0.4 % of the dc voltage) superimposed to the dc voltage.

To conclude, there is a considerable percentage of models that have not been validated, and whose applicability may be questioned. Moreover, some authors do not include how the EIS tests were carried out. Even if some commented the ac ripple amplitude and frequency range, in most cases nothing

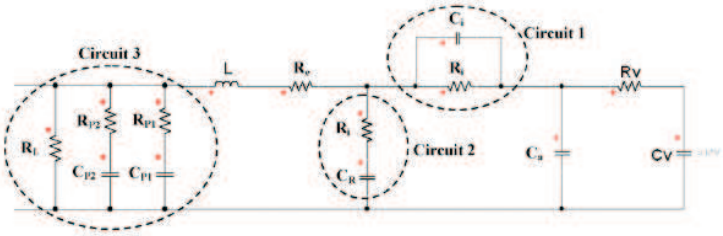

Fig. 3.22: Ultracapacitor equivalent circuit presented by Rafik [21]

is said about the impedance analyzer current limit or experimental setup and test procedure. This may be due to the fact that the ultracapacitors modeled do not present a very large capacitance. Finally, no author explains the model implementation and simulation, which is not straightforward because all the parameters depend on the voltage instead of on the current, as it is the case for fuel cells and batteries.

3.4. State-of-the-art of the simulation of hybrid electrochemical systems

The complete hardware setup of hybrid systems presents some drawbacks which cannot be ignored, such as high costs of the elements under test, the infrastructure and security requirements (especially for a hydrogen storage and supply system) and the complexity associated to the performance of the test when a high number of elements are involved. The other option is the pure simulation, which presents a lower cost, but presents the disadvantage of no real tests, to validate or confirm the system modeled. An intermediate solution between the two previous approaches is the hardware-in-the-loop (HIL) simulation, in which one or several devices of the system are used instead of their simulated models. This type of simulation lowers the cost and reduces the infrastructure needed.

In 1997 Maclay [78] underlined the usefulness of this simulation tool, which allows to mix both simulated and hardware systems. It is specially useful for hybrid energy sources and electric drives, as explained and classified by Bouscayrol [79].

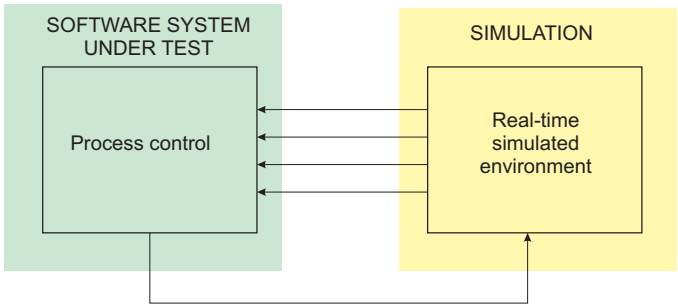

Fig. 3.23: Signal level HIL simulation

This classification is done considering the type of signal which interacts between the simulated and hardware system. The first type is the signal level HIL simulation. As seen in Fig. 3.23 the hardware element is a control scheme or similar, which interacts through control signals with the simulated environment (electric machine, mechanical load or power electronics). In this case, a control scheme can be tested without actually setting up a complex and expensive laboratory test bench due to the fact that the control schemes only need a processor and computer and the system which controls is also simulated through software. This approach has been applied, e.g. for power electronics testing [80].

The next HIL simulation level is the power level. In this case one of the simulated systems is substituted by the hardware real system, whilst the rest remains simulated. Now the simulated and hardware system also require power signals, as shown in Fig. 3.24. This is an increasingly used approach for highly complex systems, such as vehicles or electric drives. For example, Ren tested an all electric ship, with the electric machines and converters as real hardware. The simulated element is an electric power system (up to 756 nodes). The interface between simulated and hardware is done through a 5 MW power interface system, which is able to reproduce the voltage and current waveforms generated by the simulated power system. In this way, they could test the all electric ship propulsion without actually using a real ship, which is an extremely expensive option.

Moore [23] applied this simulation technique to PEM fuel cells, as presented in Fig. 3.26. In this case, Moore simulated the whole vehicle (electric

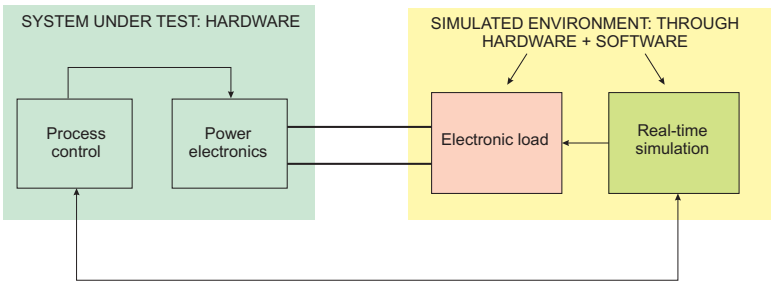

Fig. 3.24: Power level HIL simulation

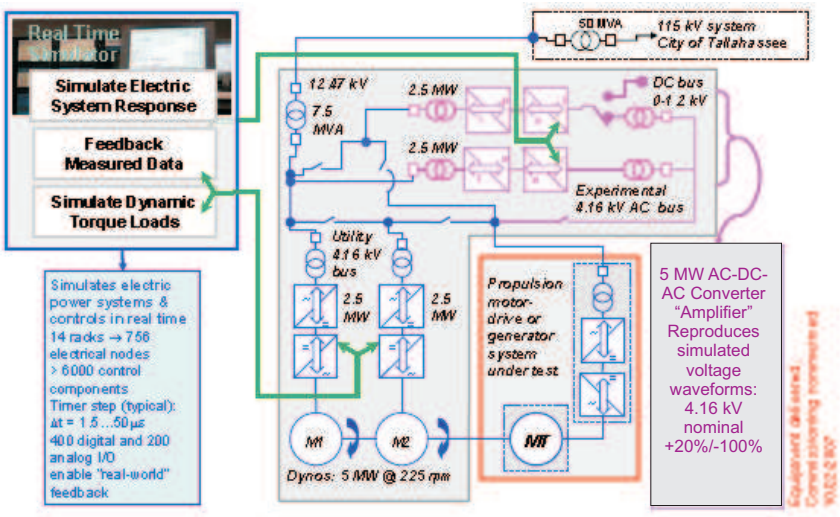

Fig. 3.25: HIL test bench for all electric ship simulation [22]

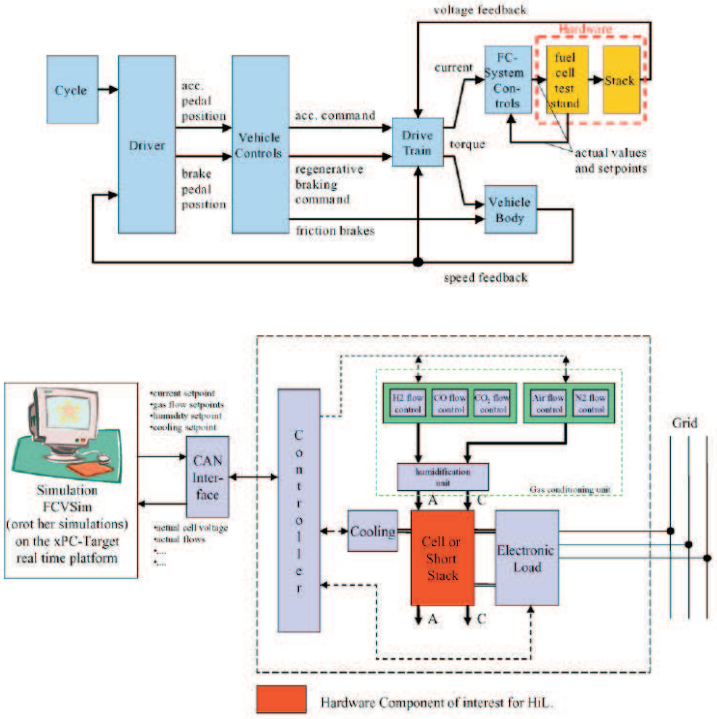

Fig. 3.26: HIL simulation presented by Moore [23]

machine included) and kept the fuel cell as the hardware element. The approach chosen by Moore is interesting due to the fact that he simulated the vehicle. However, the particular application is not realistic due to the fact that fuel cells cannot follow the vehicle load profile during acceleration or uphill, and therefore need high power storage systems.

The last HIL simulation level is the mechanical level, where the whole drive (control, power electronics and electric machine)is hardware. The simulated load is setup with a mechanical load or another electric machine. Therefore, both hardware and simulated elements interact mechanically, through the shaft, as depicted in Fig. 3.27. This mechanical level simulation can be interesting for vehicular applications, such as the diesel hybrid (battery) vehicle case carried out by Trigui [24]. In this way he could study the fuel consumption for different driving cycles. Due to the high cost and complexity of a real diesel hybrid vehicle, they simulated the vehicle chassis, driver, control, gear box and clutch, as seen in Fig. 3.28. The hardware elements were the internal combustion engine (ICE) and electric machine, with the necessary clutch and power converters. This setup is particulary useful for

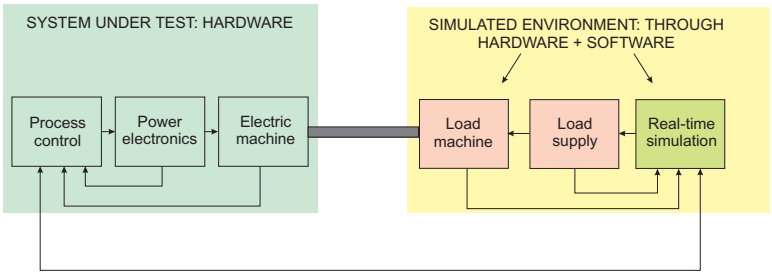

Fig. 3.27: Mechanical level HIL simulation

ICE based vehicles, but it is a very complex and expensive setup, which is specifically focused for vehicular applications, and hence presents a low flexibility for other types of loads or vehicle topologies, such as hybrid electric vehicles.

Another vehicular example of a HIL simulation, this time a power level HIL, is the hybrid electric vehicle simulated by Cheng [25]. He simulated a fuel cell/ultracapacitors vehicle with a simulated source for the fuel cell and real ultracapacitors. Due to the high cost and complexity of the vehicle, he simulated the vehicle through an electric machine connected to another electric machine connected to the dc bus, as shown in Fig. 3.29. He carried out the simulation of a normalized driving cycle. Even though this setup is simpler and with lower cost if compared to a real vehicle, the vehicle simulator is unnecessarily complex. Timmermans [81], who collaborated with the same authors as Cheng, presents similar work to the presented by Cheng, but more focused on the test bench development. In both cases, the presence of the electric machines increases the total cost and complexity. Moreover, the systems are specifically scaled for the particular case studied.

Schupbach [26] also presented a mechanical level HIL simulation for testing power trains of electric vehicles. However, he focused on the electric machine and used the Advanced Vehicle Simulator ADVISOR to simulate the energy sources. ADVISOR was developed by the National Renewable Energy Laboratory in USA (NREL) and is a Matlab/Simulink based platform which allows to simulate a wide range of commercial electric vehicles. Fig. 3.30 presents the HIL developed. Finally, another mechanical HIL simulation is the one presented by Winkler [27], who used the software Modelica/Dymola software and is also more centered on the mechanical part of the power train,

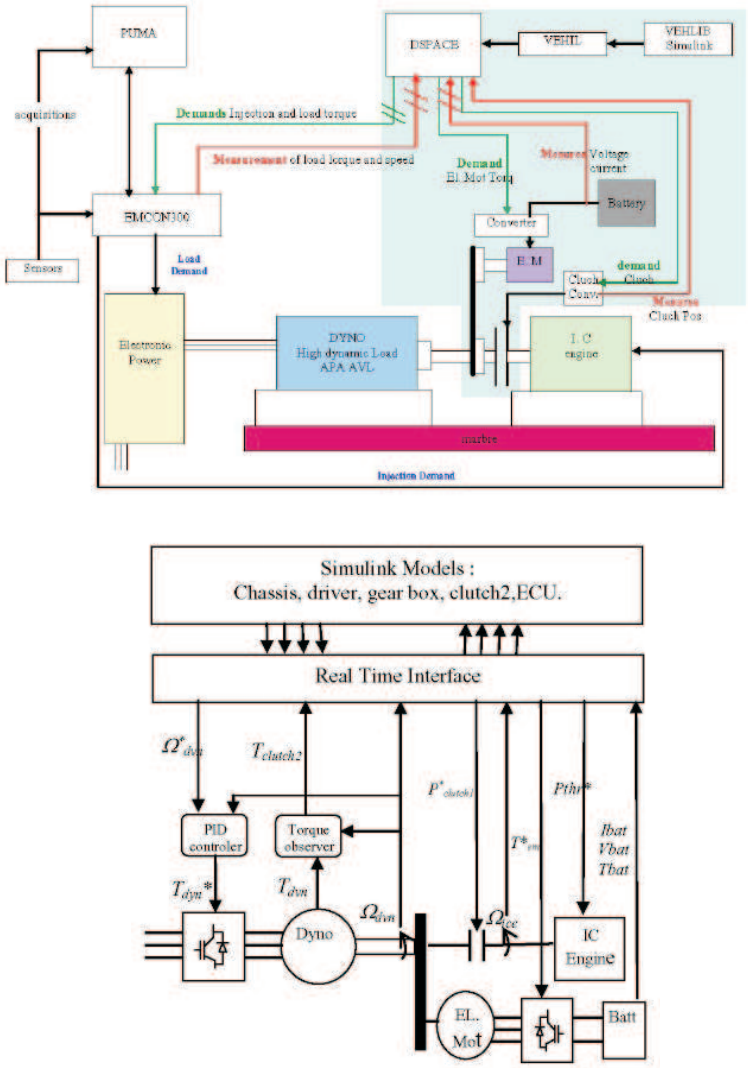

Fig. 3.28: HIL test bench for diesel hybrid vehicles [24]

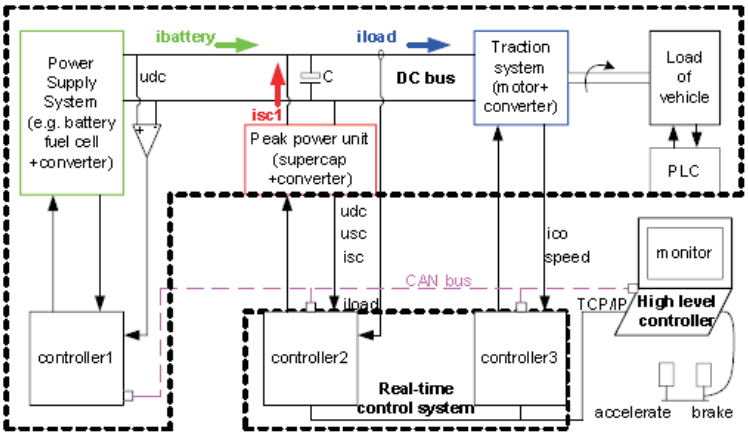

Fig. 3.29: HIL simulation presented by Cheng [25]

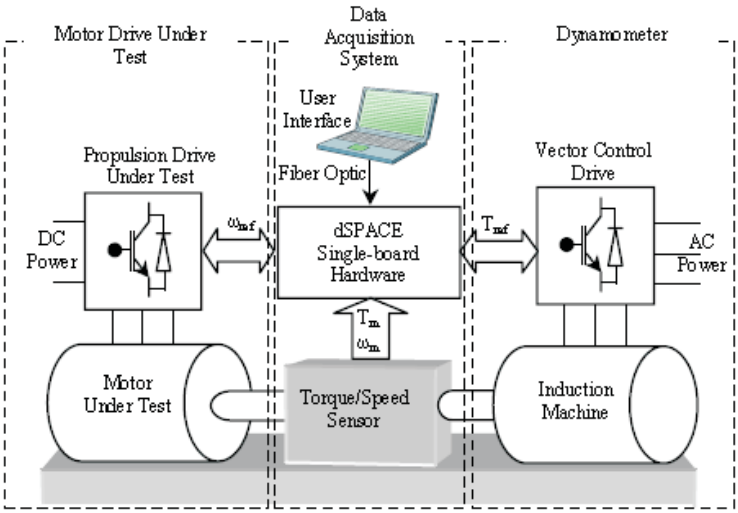

Fig. 3.30: HIL simulation presented by Schupbach [26]

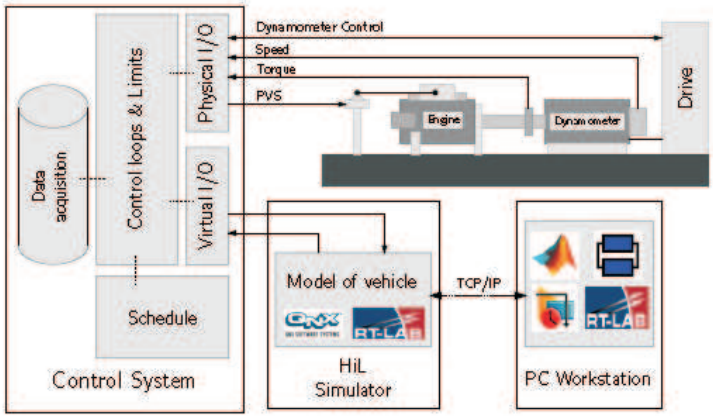

Fig. 3.31: HIL simulation presented by Winkler [27]

as it can be observed in Fig. 3.31. In both cases, the authors are very focused on the mechanical part of the power train, and not on the energy sources.

It can be concluded that most works use mechanical level HIL simulation, which is costly and complex due to the electric drives. Moore presented a power level HIL simulation for a fuel cell vehicle, with a completely simulated vehicle. However, his approach is not realistic as the fuel cell cannot supply the necessary power during acceleration. It would have been more interesting to test a hybrid electric vehicle, with both fuel cell and energy storage system. Moreover, this case would allow a more realistic study, due to the fact that the storage systems could absorb regenerative breaking, which was not tested

by Moore.

CHAPTER 4

Nonlinear dynamic model for fuel cells

4.1. Introduction

This chapter presents a nonlinear dynamic model of PEM fuel cells for simulation purposes, in both absolute and relative (per-unit) units, its deduction, development and validation.

A PEM fuel cell is an electrochemical system which produces the electric power through its principal component: the stack. But the stack needs auxiliary systems, such as fan, compressor, filter, etc. in order to keep the stack environment in the correct operating conditions. Hence, the PEM fuel cell behavior presents thermal effects due to the heat generation, fluid dynamics present by the water and gas transport, electrochemical reactions in the stack, electrical phenomena, etc. The fluid, thermal and electrochemical approach are specially useful for the development stage of fuel cells. But for its integration in its final application it is more useful an electric model, which can easily interact with the rest of electric models: electric machines, grid, power converters, etc.

Therefore, in this Thesis an electric model will be developed. This elec-

tric model will adopt the form of an equivalent circuit which will be able to reproduce its voltage dynamic performance. The parameters of the resulting equivalent circuit will be obtained through electrochemical impedance spectroscopy EIS tests. Although the work is applied to a PEM fuel cell, the experimental methodology and results can be extended to other technologies such as SOFC, DMFC, PAFC, etc.

The PEM fuel cell studied is a 1.2 kW Nexa Ballard fuel cell which operates with direct gaseous hydrogen at its anode and air at its cathode [28]. Its principal characteristics are detailed in Fig. 4.1 and Fig. 4.2, and Fig. 4.3 presents its photograph. The Nexa fuel cell presents the particular characteristic of being a closed system, in which the user can only control the current output, but not the auxiliary services: pump, fan, etc. To do that it would have been necessary to modify the hardware of the control system by cutting wires and soldering new components to the printed circuit. Obviously this operation would have invalidated the product warranty. Therefore, the model presented does not control the auxiliary services, as this is done by the onboard fuel cell control system. If this can be a disadvantage for control purposes, it turns into an advantage taking into account that most commercial fuel cells are also closed loop systems. This is specially beneficial for safety reasons.

4.2. EIS tests experimental procedure

Electrochemical Impedance Spectroscopy EIS is an experimental procedure carried out in the frequency domain, in which either the current or voltage of the tested element is controlled, their ratio being represented by an electrical impedance, as explained in more detail in the State-of-the-art chapter.

Due to the fact that the fuel cell current is more easily controlled than voltage, galvanostatic (current control) mode tests are conducted. In this mode the fuel cell is set to its dc operation current and a small signal ac current with variable frequency is superimposed. Both the dc+ac current components cause a dc+ac voltage response, which allows the obtention of

OUTPUTS	Requirement	Definition	Quantity
Power1	Rated Power	Capacity at Standard Conditions, BOL	1200 W
Voltage	Operating voltage range	22 V to 50 V	
Voltage at Rated Power	26 V		
Start-up Time	Min. time to Pn from a Cold Start	2 minutes	
Emissions	Noise	Maximum noise emission at 1m	72 dBA
Water	Max. water produced at Pn	870 mL/hr	
Physical	Dimensions	L x W x H	56 x 25 x 33cm
Mass	Total system mass	13 kg	
Lifetime	Operating Life	Minimum number of operating hours before EOL	1500 hours
Cyclic Life	Min. nº start and shut-down cycles before EOL	500	
Shelf Life	Min. storage before EOL	2 years	
INPUTS	Requirement	Definition	Quantity
Fuel	Purity	Lowest acceptable concentration of hydrogen	99.99% H2 (vol)
Pressure	Allowable inlet supply pressure	70 – 1720 kPa(g)	
Acceptable Impurities	Max. inert fluids	0.01% (vol)	
Maximum CO and CO2 combined	2 ppm (vol)		
Maximum total hydrocarbon	1 ppm (vol)		
Maximum oxygen	500 ppm (vol)		
Consumption	Max. fuel consumption at Pn	less than 18.5 SLPM	
Power Conditioning	Current Ripple	Max. current ripple at 120 Hz	24.7% RMS 35% pp
DC Power	Voltage	Allowable range of input voltage	18 V to 30 V
Supply	Power	Maximum power draw during start-up	60 W
Operating	Location	Acceptable locations for use	Indoors and outdoors
Environment	Temperature Range	Acceptable ambient, cooling and oxidant air Tº	3°C - 40°C
Relative Humidity	Acceptable ambient relative humidity	0% - 95% (non-condensing)	
EMI Tolerance	Operates safely in the EMI environment	specified by UL 991	

Fig. 4.1: Characteristics of the Nexa fuel cell

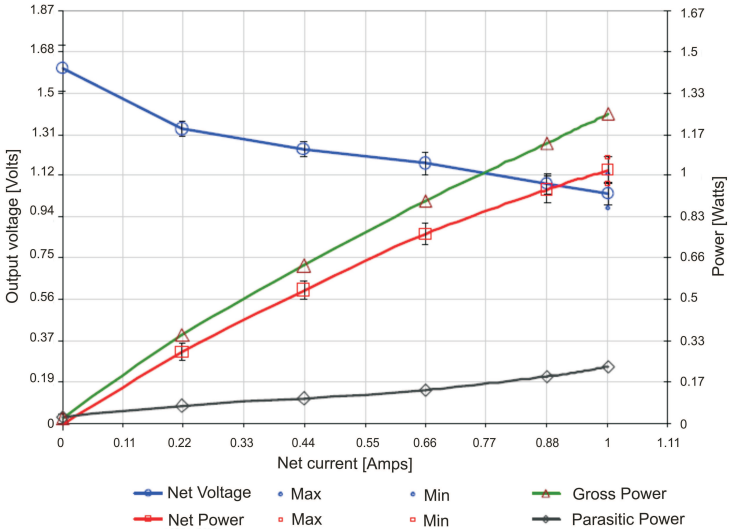

Fig. 4.2: Nexa fuel cell characteristic curve [28]

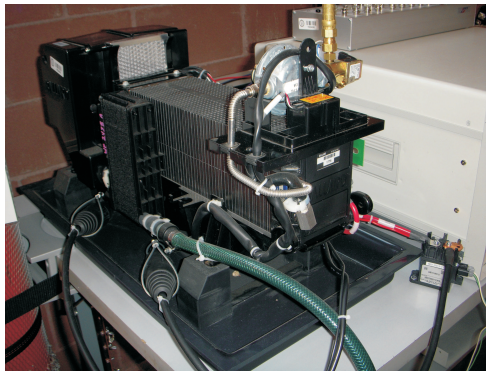

Fig. 4.3: Nexa fuel cell used

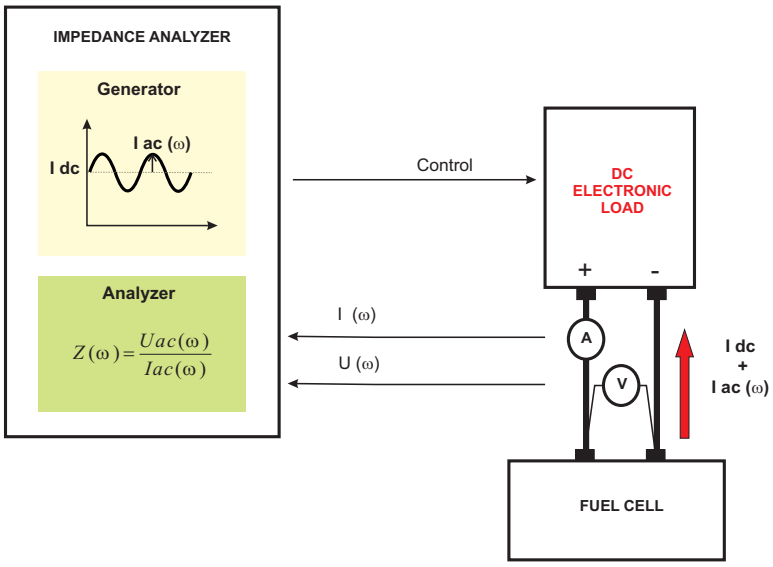

Fig. 4.4: *EIS* on fuel cells

the battery complex impedance taking into account only the ac components of the current and voltage signals, as depicted in Fig. 4.4.

4.2.1. DC operation conditions

In this Thesis EIS tests were carried out for different output currents ranging from 10 to 50 A. According to the operational manual [28] the tests could be performed up to 60 A. However, at 50 A the fan and air pump duty cycle were already near 95 %, hence, this value has been chosen as a practical current limit. The tests were carried out after 1 h of continuous operation in the working point owing to the slow dynamics. To reach the steady-state

situation the fuel cell needs a certain amount of time for the membrane to hydrate adequately and to reach the operation temperature. Obviously, this time depends on the current programmed. For low currents, the steady-state regime is reached more quickly due to the relatively small temperature increase. Higher currents increase the water generation at the cathode and cause higher stack temperatures, and therefore the fuel cell needs a longer time to reach its humidity, temperature and voltage steady-state regime. Other authors wait up to 5 h, as [58].

During the tests the anode of the fuel cell was fed with hydrogen at 11 bar (from a 200 bar bottle by means of a pressure regulator). As the Nexa fuel cell is provided with a communications board and its own software, an external 24 V power supply was needed.

4.2.2. AC test conditions

As seen in Fig. 4.5, for each operation point an ac component is superimposed. The amplitude of the ac component must not disturb the linearity hypothesis which is supposed during the tests. In order to calculate the impedance it is necessary to suppose that current and voltage have a linear relationship during each EIS test. However, the final model obtained is not linear, due to the fact that voltage does not vary lineally with current, as depicted in Fig. 4.5. The sinusoidal ac superimposed current can admit different amplitude values, however, it should not be too high as it would alter visibly the dc operation point, nor too small as it would be confounded with the noise present in the signal. Yuan [55] investigated different amplitude values and finally selected a 5 % of the dc current because other values distorted the Nyquist plot, as explained during the state-of-the-art. Following the recommendation done by Yuan, in this Thesis we also apply an ac signal with an amplitude of a 5 % of the dc current.

The ac signal frequency sweep can be as wide as desired, e.g. from mHz to MHz. The frequency interval is limited by the test time and the test purpose. If the lower frequency limit is very low, the test time would lengthen and the test conditions (fuel cell humidity, temperature, etc.) would vary from

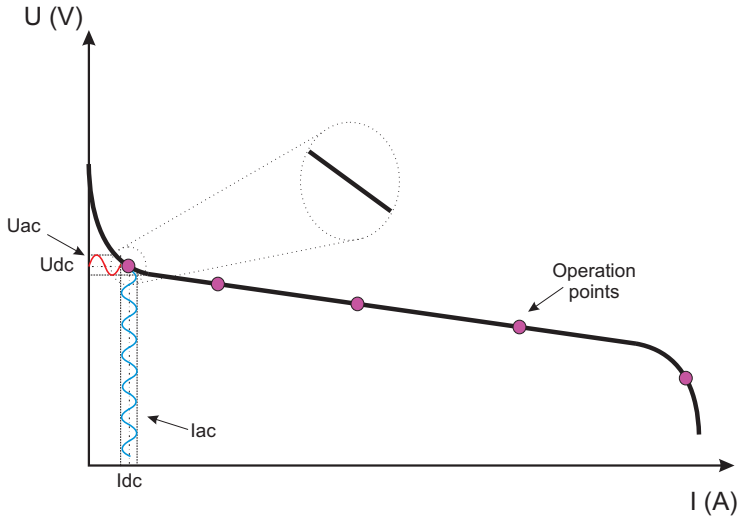

Fig. 4.5: EIS test linearity vs. final model nonlinearity

the beginning to the end of the test, invalidating the results obtained. The maximum frequency limit is defined by the maximum operating frequency at which the fuel cell will be operated, i.e. the rise time of the most abrupt transitory, which will not exceed the kHz frequencies. With these considerations in mind, the frequency interval selected is 0.5 Hz-6 kHz as with these frequencies the tests render the results needed. In order to obtain solid data, 20 cycles are applied for each frequency and 40 points per decade registered.

4.2.3. Experimental setup

To carry out the EIS tests the following equipment has been used:

- Impedance analyzer (Solartron 1260).
- DC electronic load (Chroma 63201: 80 V, 300 A).
- DC power source (Sorensen SGI: 60 V, 167 A).
- LEM LA 55-P current transducer.
- ±15 V power source for transducer supply.
- Computer.
- Nexa Ballard fuel cell.

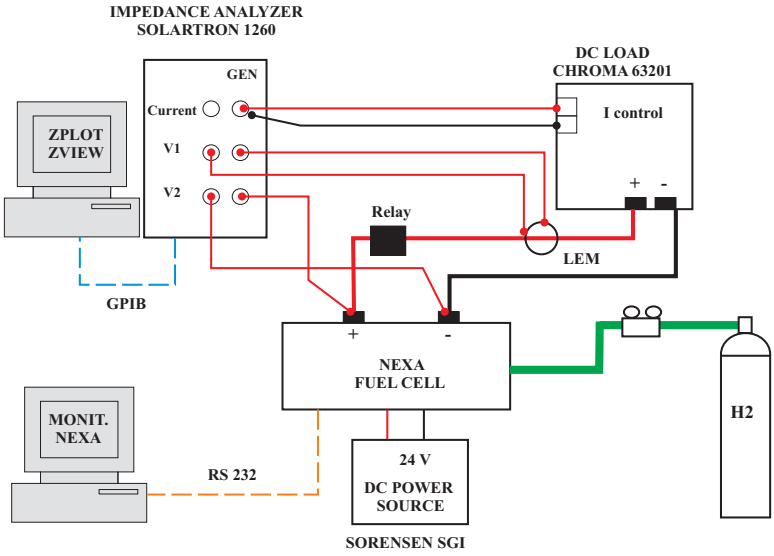

Fig. 4.6: Experimental setup for Nexa fuel cell EIS tests

The wiring diagram and a photograph of the EIS tests experimental setup are presented in Figs. 4.6 and 4.7. The tests are controlled by the impedance analyzer Solartron 1260, which through the software ZPlot sends an analogical signal to the electronic load representing the dc+ac current forced at the output of the fuel cell. The current and voltage are measured through the terminals V1 and V2 and sent to the impedance analyzer, which can then calculate the complex impedance by extracting the ac components of the current and voltage. The impedance measurements takes into account the power cables included in the Nexa fuel cell for its connection.

4.3. EIS tests results: fuel cell impedance model

The data obtained during the EIS tests is then processed with the software ZView, which represents the Nyquist and Bode plots for the complex impedance calculated, as presented in Fig. 4.8. The abcissa axis Z′ represents the real part of the fuel cell complex impedance, whilst the ordinate axes Z” represents the imaginary part. The frequency sweep starts at the minimum frequency, which corresponds to the farthest point in the right hand side of the Nyquist plot and increases as the test develops towards the left hand side points. Negative values of Z” correspond to the capacitance behavior

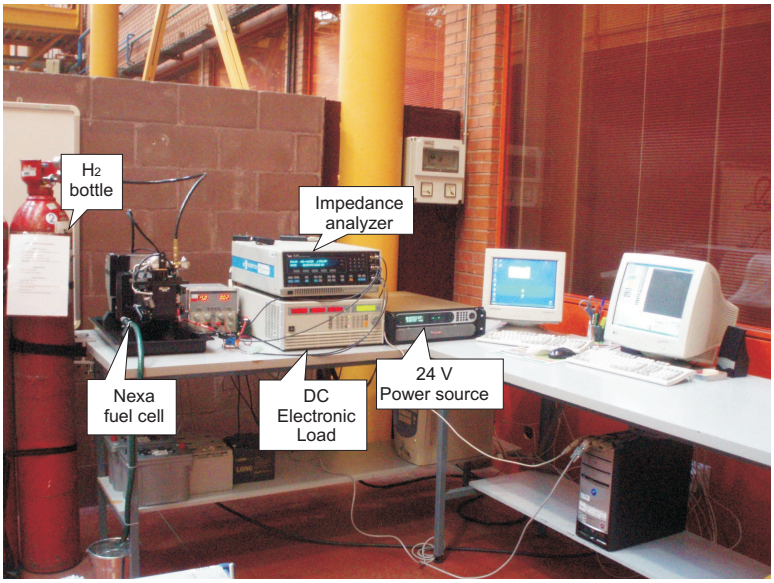

Fig. 4.7: Experimental setup photograph

of the fuel cell, whilst positive values correspond to inductive behavior. The resonance frequency point is defined as the frequency in which the capacitive and inductive impedances cancel each other, and therefore the fuel cell impedance becomes purely resistive (Z"=0). As it can be observed in Fig. 4.8, the complex impedance of the fuel cell decreases for increasing currents up to 40 A and increases for higher currents. This phenomenon is also described in [54], and is present at high currents, when the mass transfer is dominant.

To obtain an electric model, the impedance values obtained through the EIS tests must be fitted to a particular electric circuit. The software ZView allows to test between any electric circuit defined by the user with the elements included in its library. Therefore, a wide combination of circuits can be tested. Fig. 4.9 presents the information returned by ZView for the 10 A test, which includes the parameters, its absolute values and error between the experimental and simulated equivalent circuit. The circuit presented is formed by a series inductance which represents the inductive behavior of the system at high frequencies, a series resistance which reflects the ionic resistance of the membrane. The circuit also presents an R_1CPE network. The constant phase element CPE, as explained by [46], [82] and [54], is a fictitious element which can model diffusion phenomena, roughness of electrodes or inhomogeneous distribution of reactants on the surface. The CPE can also try

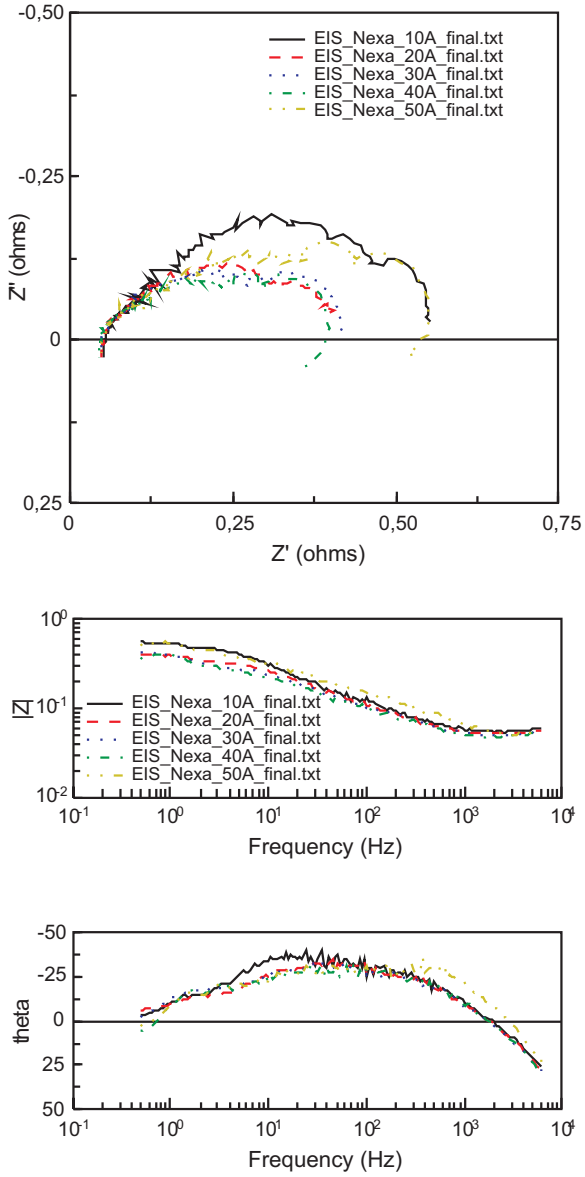

Fig. 4.8: Nexa fuel cell Nyquist and Bode plots

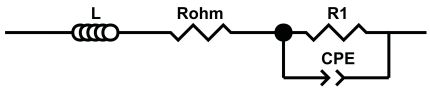

Element	Freedom	Value	Error	Error %
L	Free(+)	8,1432E-7	2,0041E-8	2,4611
Rohm	Free(+)	0,049393	0,00043111	0,87282
R1	Free(+)	0,56896	0,0065807	1,1566
CPE-T	Free(+)	0,15304	0,0042221	2,7588
CPE-P	Free(+)	0,67358	0,0049499	0,73486

Fig. 4.9: Fuel cell parameters rendered by ZView

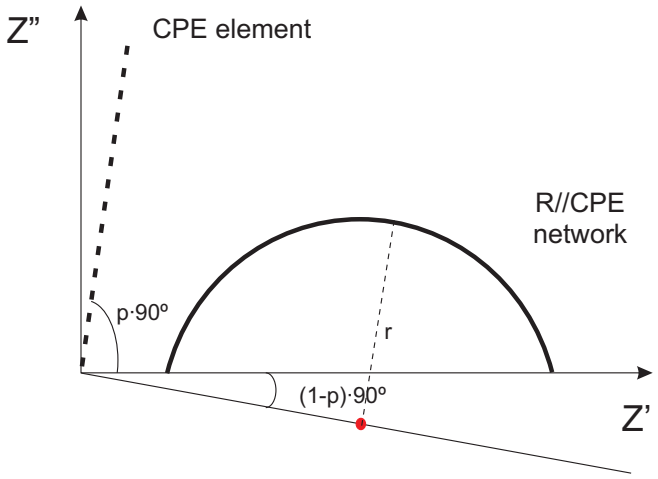

Fig. 4.10: CPE and R-CPE Nyquist plots

to represent the fractal dimension of surfaces which are not 2D or 3D, but an intermediate value. In this Thesis, we have used a CPE due to the fact that it takes into account all these phenomena and combined with a resistance can reproduce the semicircle that appears in the Nyquist plot, whose center does not lay on the abscissa axis, but in a lower position, as depicted in Fig. 4.10. Mathematically, the CPE impedance can be described as:

$$\frac{1}{Z} = Y = T_{cpe} \cdot (j \cdot \omega)^p \tag{4.1}$$

The parameter p varies between 0.5 and 1, therefore the CPE Nyquist plot is not a vertical line as a capacitor, but inclined with a $p{\cdot}90^o$ angle. If p is 1, the equation is identical to a capacitor equation. However, a CPE is not a physical element, and cannot be described by a single electric equation, hence, an equivalent capacitor C_1 can be calculated with (4.1) for the R-CPE network, where T_{cpe} and p are the CPE parameters.

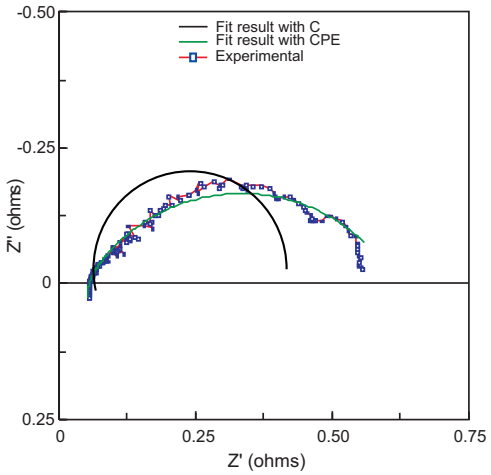

Fig. 4.11: Difference in the C or CPE fitting

$$C_1\,(F) = T_{cpe} \cdot (\omega_{\text{máx}})^{p-1} = \frac{(T_{cpe} \cdot R)^{1/p}}{R} \tag{4.2}$$

The value of this equivalent capacitor is different from the one obtained if the Nyquist plot is directly fitted to an RC network instead of an R-CPE network. For instance, for the test at 10 A, the value of C was a 40 % smaller than the equivalent capacitor calculated after fitting the CPE. The different fit for each option is shown in Fig. 4.11. This advantage of the CPE over the capacitor is also commented, but no proved, by [59].

4.3.1. Fuel cell equivalent circuit

Therefore, the equivalent circuit obtained is shown in Fig. 4.12, where E is the fuel cell internal voltage, R_{ohm} the contact resistance and R_1C_1 the network which emulates the double layer capacitor. The voltage on terminals of the fuel cell is U_{fc}.

A study of the dependency of each parameter of the equivalent circuit as polynomial equations with the current is carried out. To prove this dependency a statistical analysis is carried out with the statistical software Statgraphics. Statgraphics is a statistical program developed by Statpoint Technologies Inc. which is a 32 bit program which runs under Windows.

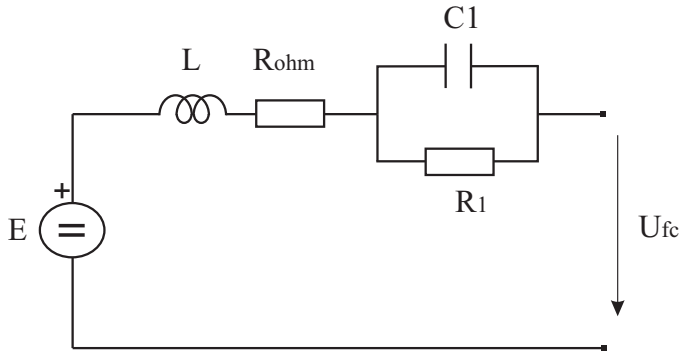

Fig. 4.12: Fuel cell equivalent circuit

An example of the information returned by Statgraphics for R_1 is presented in Fig. 4.13. The information yielded by Statgraphics includes the observed vs. predicted plot, in which the model points should be as near as possible to the line with slope 1 shown. It can be observed that the predicted vs. observed values values adjust very satisfactorily to the 45º line.

The electrical equations which can be obtained from Fig. 4.12 are presented in (4.3) and (4.4):

$$\begin{aligned}
L\,(H) &= 1{,}33 \cdot 10^{-6} - 5{,}23 \cdot 10^{-8} \cdot I + 6{,}41 \cdot 10^{-10} \cdot I^2 + 5{,}09 \cdot 10^{-12} \cdot I^3 \\
R_{ohm}\,(\Omega) &= 0{,}05 - 7{,}83 \cdot 10^{-6} \cdot I + 1{,}97 \cdot 10^{-5} \cdot I^2 - 2{,}39 \cdot 10^{-7} \cdot I^3 \\
R_1\,(\Omega) &= 0{,}76 - 0{,}02 \cdot I + 1{,}80 \cdot 10^{-4} \cdot I^2 + 3{,}97 \cdot 10^{-6} \cdot I^3 \\
C_1\,(F) &= 0{,}12 - 0{,}01 \cdot I + 7{,}27 \cdot 10^{-4} \cdot I^2 - 1{,}45 \cdot 10^{-6} \cdot I^{,3} + 9{,}36 \cdot 10^{-8} \cdot I^4
\end{aligned} \tag{4.3}$$

$$\begin{aligned}
U_{fc}\,(V) &= E - R_{ohm} \cdot I - \left(I - C_1 \cdot \frac{dU_{C1}}{dt} \right) \cdot R_1 \\
E\,(V) &= N \cdot \left[E_0 + \frac{RT}{2F} \cdot \left(\ln \frac{p_{H_2} \cdot \sqrt{p_{O_2}}}{p_{H_2O}} \right) \right]
\end{aligned} \tag{4.4}$$

N is the number of cells in series (47), E_0 is the standard no load fuel cell voltage, R the universal gas constant, T the stack temperature, F the Faraday constant, p_{H_2} the partial pressure of hydrogen at the anode, p_{O_2} the partial pressure of oxygen at the cathode and p_{H_2O} the partial pressure of water formed at the cathode. The stack temperature is highly dependant on the current generated by the fuel cell, and will be demonstrated later.

Multiple Regression Analysis

Dependent variable: R1

Parameter	Estimate	Standard Error	T Statistic	P-Value
CONSTANT	-0,881369	0,0776897	-11,3447	0,0560
I	0,132302	0,0101552	13,028	0,0488
I^2	-0,00438669	0,000376927	-11,638	0,0546
I^3	0,0000451043	0,00000416174	10,8378	0,0586

Analysis of Variance

Source	Sum of Squares	Df	Mean Square	F-Ratio	P-Value
Model	0,0829511	3	0,0276504	110,86	0,0687
Residual	0,000249409	1	0,000249409		
Total (Corr.)	0,0832006	4			

R-squared = 99,7002 percent
R-squared (adjusted for d.f.) = 98,8009 percent
Standard Error of Est. = 0,0157927
Mean absolute error = 0,00604027
Durbin-Watson statistic = 3,57143

The StatAdvisor

The output shows the results of fitting a multiple linear regression model to describe the relationship between R1 and 3 independent variables. The equation of the fitted model is

R1 = -0,881369 + 0,132302*I - 0,00438669*I^2 + 0,0000451043*I^3

Since the P-value in the ANOVA table is less than 0.10, there is a statistically significant relationship between the variables at the 90% confidence level.

The R-Squared statistic indicates that the model as fitted explains 99,7002% of the variability in R1. The adjusted R-squared statistic, which is more suitable for comparing models with different numbers of independent variables, is 98,8009%. The standard error of the estimate shows the standard deviation of the residuals to be 0,0157927. This value can be used to construct prediction limits for new observations by selecting the Reports option from the text menu. The mean absolute error (MAE) of 0,00604027 is the average value of the residuals. The Durbin-Watson (DW) statistic tests the residuals to determine if there is any significant correlation based on the order in which they occur in your data file. Since the DW value is greater than 1.4, there is probably not any serious autocorrelation in the residuals.

In determining whether the model can be simplified, notice that the highest P-value on the independent variables is 0,0586, belonging to I^3. Since the P-value is less than 0.10, that term is statistically significant at the 90% confidence level. Depending on the confidence level at which you wish to work, you may or may not decide to remove I^3 fr

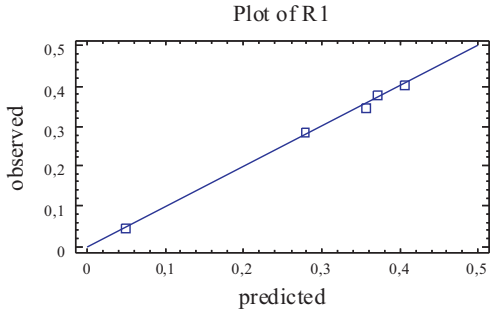

Fig. 4.13: Information returned by Statgraphics for *R1*

The partial pressures can be obtained through the ideal gas law, which is, for example, applied to hydrogen as:

$$p_{H_2} \cdot V_{an} = n_{H_2} \cdot R \cdot T \tag{4.5}$$

V_{an} [83] is the volume of gas present in the anode and n_{H_2} the moles of hydrogen. If (4.5) is derived respect to time (4.6) is obtained.

$$\frac{dp_{H_2}}{dt} = \frac{RT}{V_{an}} \cdot q_{H_2} = \frac{RT}{V_{an}} \cdot \left(q_{H_2}^{in} - q_{H_2}^{out} - q_{H_2}^{r}\right) \tag{4.6}$$

q_{H_2} is the flow of hydrogen in (moles/s).
$q_{H_2}^{in}$ is the flow of hydrogen moles which enter the stack.
$q_{H_2}^{out}$ is the flow of hydrogen moles which leave the stack.
$q_{H_2}^{r}$ is the flow of hydrogen moles which react in the stack.

The flow of hydrogen and air moles which enter the stack can be measured with a flow meter. If no flow meter is used, as in this Thesis, the flow of moles can be calculated indirectly with (9) known the flow of moles which have reacted and the stoichiometric relationship SR of the gas. The gas SR reflects the gas excess which should be supplied to the reaction in order to obtain a satisfactory reaction. Here we have used the SR approximation suggested by [83].

$$\begin{aligned} SR &= \frac{q_{H_2}^{in}}{q_{H_2}^{r}} \\ SR_{H_2} &= 1{,}02875 + 0{,}00412546 \cdot I \\ SR_{O_2} &= 5{,}51131 - 0{,}138273 \cdot I + 0{,}00146051 \cdot I^2 \\ q_{H_2}^{r} &= \frac{I}{2 \cdot F} \end{aligned} \tag{4.7}$$

Equation (4.8) is obtained if (4.7) is substituted in (4.6).

$$\begin{aligned} \frac{dp_{H_2}}{dt} = \frac{RT}{V_{an}} \cdot q_{H_2} = \frac{RT}{V_{an}} \cdot \left(SR_{H_2} \cdot q_{H_2}^{r} - q_{H_2}^{r}\right) = \\ = \frac{RT}{V_{an}} \cdot (SR_{H_2} - 1) \cdot \frac{I}{2F} \end{aligned} \tag{4.8}$$

Similar equations can be deduced for the oxygen and water partial pressures. Known these partial pressures and substituted in (4.4) allows calculating the fuel cell output voltage.

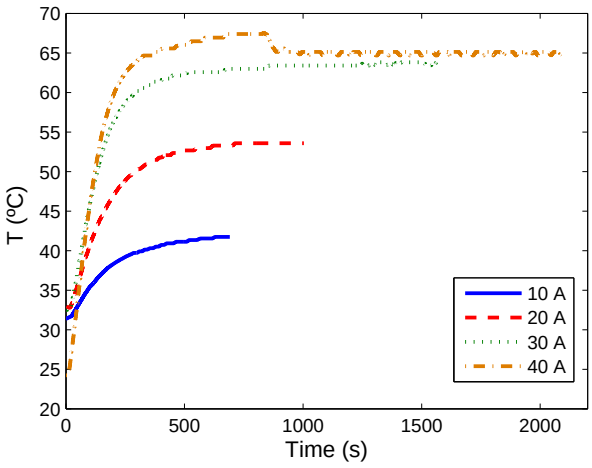

Fig. 4.14: Temperature evolution for different current steps

4.3.2. Temperature model

As pointed out before, the fuel cell output voltage is influenced by the stack temperature [8] whilst the temperature depends on the current supplied by the fuel cell [52], [53]. The temperature is controlled by the fuel cell control system, and includes a fan for cooling purposes. To investigate the dependency of temperature with current, current steps for 10, 20 and 30 A were applied to the fuel cell until the stationary temperature was reached. The temperature evolution for these current steps is presented in Fig. 4.14.

With these results, the final temperature for each current and thermal time constant can be calculated. This thermal time constant is influenced by the cooling fan, which is normally at a certain percentage duty cycle in order to, not only to cool the stack, but also dilute hydrogen that is purged from the fuel cell during normal operation [28]. The thermal time constant is obtained as the time elapsed until the 63 % of the steady-state value is reached. Again, the software Statgraphics is used to obtain the relationship between current and the thermal time constant. Fig. 4.15 presents the results and observed vs. predicted curve, which shows a good agreement:

$$\tau\,(s) = 181{,}624 + 0{,}8028 \cdot I - 0{,}0532 \cdot I^2 \tag{4.9}$$

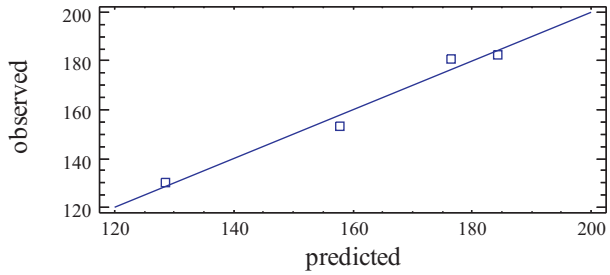

Fig. 4.15: Statgraphics result for the thermal time constant

Whilst the dependency of the final temperature with the current can be expressed as:

$$T_f\,(^{\circ}C) = 24{,}4975 + 1{,}9058 \cdot I - 0{,}0531 \cdot I^2 \tag{4.10}$$

Known the stationary temperature and the time constant, the temperature evolution with time and current for an initial temperature T_0 (room temperature) can be obtained with:

$$T\,(^{\circ}C) = T_0 + (T_f - T_0) \cdot (1 - e^{-t/\tau}) \tag{4.11}$$

In order to validate the temperature model proposed, the current profile of Fig. 4.16 is applied to the fuel cell, whilst the temperature and fan duty cycle are measured. The results can be observed in Fig. 4.17.

It can be observed in Fig. 4.17 that the simulated temperature follows the measured values, except for high currents, which provokes the model to deviate. This difference is due to the fact that the fan increases its duty cycle nearly a 20 % when the stack temperature rises above 65°C, thus changing the heat transfer rate of the stack. On the contrary, the modeled temperature keeps rising with a slightly different time constant. This difference affects the subsequent points. When the duty cycle returns to near a 35 %, the simulated and experimental temperatures match again.

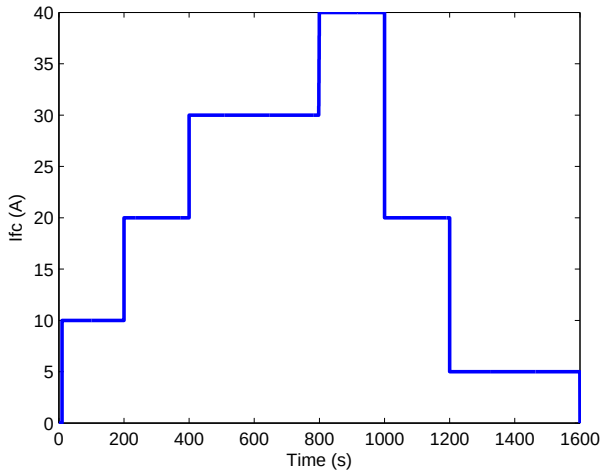

Fig. 4.16: Current profile applied to fuel cell and model

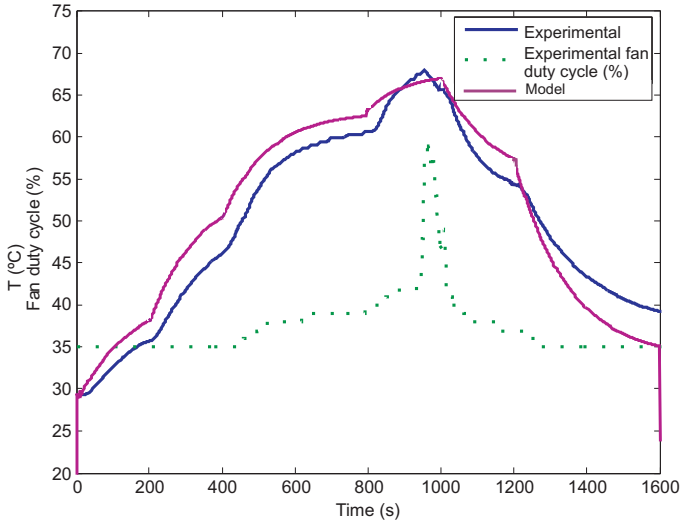

Fig. 4.17: Temperature model validation

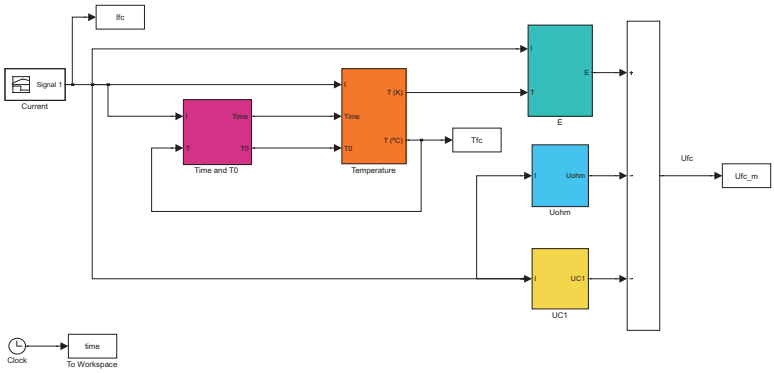

Fig. 4.18: Fuel cell Matlab/Simulink model

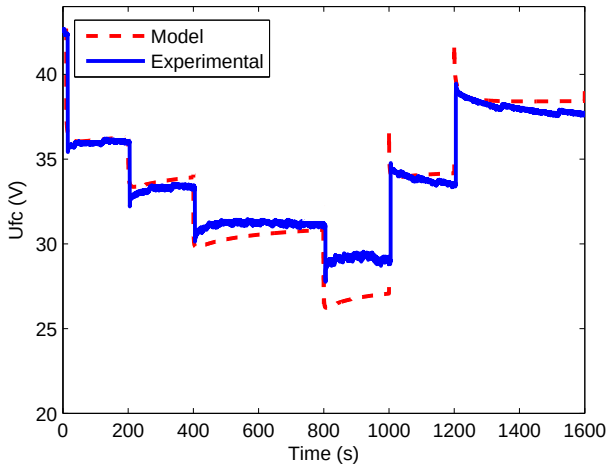

Fig. 4.19: Complete model validation

4.3.3. Complete model validation

The electrical equivalent circuit equations and temperature model were programmed in Matlab/Simulink, as shown in Fig. 4.18. The same current profile in Fig. 4.16 was applied to the fuel cell and the voltage was monitored. The comparison between experimental and modeled values are presented in Fig. 4.19.

In general the model yields a good approximation of the experimental values. Here also, a maximum difference of an 8 % appears during the maximum current pulse, which provokes the increase of the stack temperature and fan duty cycle. The temperature affects the fuel cell impedance [53], [52], especially at very high temperatures, as in this case.

4.4. Per-unit approach

A per unit system pursues the representation of electric variables as dimensionless values referred to a set of base values. The electric variables in a power system are power, voltage, current and impedance and a mathematical relationship between them can be found. As there are four different, but interdependent variables, it is a two degree of freedom system in which once two of base values are defined, the other two can be obtained with (4.12).

$$\begin{aligned} P &= U \cdot I \\ U &= I \cdot Z \end{aligned} \tag{4.12}$$

The definition of the base values is an arbitrary decision; however, for a particular component it is usual to select the its rated values as base values. For example, in a generator with rated 200 MVA and 20 kV voltage, the base power and voltage can coincide with its rated values. Hence, the base current and impedance can be calculated as:

$$\begin{aligned} I_b &= \frac{S_b}{\sqrt{3} \cdot U_b} = \frac{200 \cdot 10^6}{\sqrt{3} \cdot 20 \cdot 10^3} = 5773{,}5\,A \\ Z_b &= \frac{U_b^2}{S_b} = \frac{(20 \cdot 10^3)^2}{200 \cdot 10^6} = 2\ \Omega \end{aligned} \tag{4.13}$$

For this example, if an element consumes 20 MW, the p.u. power will be 0.1 p.u, which gives an understandable measure of the power consumed compared with the rated value.

As it was pointed before, power systems may present different voltage levels; therefore, the base voltage will be different for each area. The power element which separates each different base voltage region is a power transformer, which establishes the voltage levels depending on the number of turns of its windings. Fuel cells are not directly connected to a power transformer, but to an electronic power converter, which carries out the same function of voltage area definition as the power transformer.

4.4.1. Steady-state per-unit system for a fuel cell

In this work we will present a per-unit model for a Ballard Nexa 1.2 kW fuel cell. The voltage and power curve are depicted in Fig. 4.20. As it can be

Base power	Base current	Base voltage	Base impedance
1.2 kW	45 A	26.67 V	0.59267 W

Table 4.1: Steady-state base magnitudes

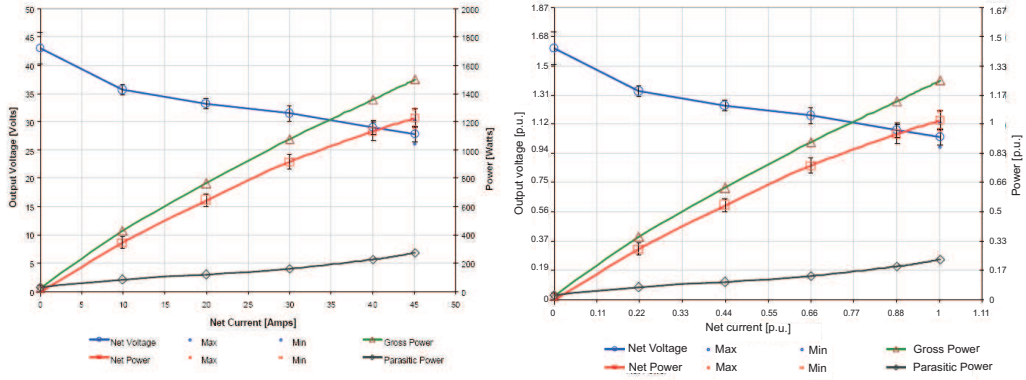

Fig. 4.20: Nexa fuel cell voltage and power characteristic in absolute (left) [28] and p.u. values (right)

observed, the maximum power obtained is 1.2 kW at 45 A of current. The curves have not been depicted for higher currents as the power and voltage values would decrease nonlinearly and provoke a low efficient operation. As the rated power is 1.2 kW, this value will be chosen as the base power. Likewise, the base current can be 45 A. However, this decision is arbitrary and other values may be considered. Known these two base values, the rest of the base values can be calculated according to (4.12). The whole set of base values are presented in Table 4.1. With these base values, the absolute curve in Fig. 4.20 can be regarded from a different perspective if the voltage, current, and power values are expressed in p.u. values, as done in the right side of Fig. 4.20.

With a simple glance to the p.u. curve of Fig. 4.20 it it is possible to know, e.g. how far each point is from the rated operation point (1 p.u.). This cannot be done when absolute values are used, as seen in the absolute curve of Fig. 4.20. Therefore, the curves are the same, but the language in which they are expressed highlight information which otherwise would go unnoticed.

4.4.2. Per-unit approach during alternate loads

The previously defined steady-state base values were proposed taking into account that fuel cells generate dc electric power, and that their theoretical operation point is a fixed point. However, fuel cells are able to admit an ac component superimposed to its dc operation point, which may be due to the particularities of the load or to the influence of the power converter to which it is connected [84]. The frequency and amplitude of this ac component can influence the fuel cell output power and life. An increase of this ac component will reduce the output power and a high load frequency can provoke concentration voltage drops due to the inability of reactants to reach the catalyst layers at the required speed.

For these situations it may be interesting to model the fuel cell taking into account the influence of frequency on the fuel cell impedance. This dependency is reflected on the EIS tests carried out. The fuel cell impedance varies from capacitive, to resistive and inductive behavior depending on the frequency of the load ac component.

To take into account these ac components on a per-unit system it is necessary to define a base frequency. Even though Choi [84] also defined a per-unit system he did not take into account the influence of an ac load on the per-unit system, even though he defined a dc and ac equivalent circuit. Hence, a criterion for the selection of the base frequency should be established. Studying the Nyquist plot, there are two singular candidate points to be considered. The first one is the cut-off frequency for R_1C_1, defined as seen in (4.14), and shown in Fig. 4.21.

$$f_{c1} = \frac{1}{R_1 C_1} \tag{4.14}$$

The second possible point is the resonance frequency, pointed out in Fig. 4.21 as the frequency at which the capacitive and inductive impedances cancel each other, and therefore the fuel cell impedance becomes purely resistive. The choice of the resonance frequency as the base frequency has a relevant advantage compared to the cut-off frequency, which is the simple identification in the Nyquist plot where Im[Z(w)] = 0, or in the Bode plot, where $\omega = 0$. Moreover, there is a further reason to select the resonance frequency

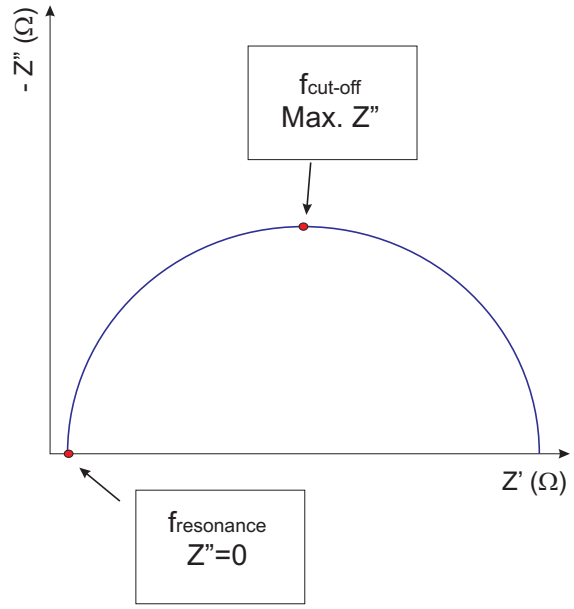

Fig. 4.21: Cut-off and resonance frequency

as base frequency: in this point the per-unit frequency is 1 p.u. Per-unit frequencies lower than one will automatically imply a capacitive behavior, while values higher will reflect an inductive behavior.

Albeit this resonance point is easily identifiable, it slightly decreases for increasing current, as depicted in Fig. 4.22. So, the previous base current(45 A) is the recommended decision criterion to select the base frequency. Considering that the steady-state base magnitudes were selected for rated values it is logical to infer that the base frequency should also be selected for rated current. Therefore, the base frequency chosen for the Nexa fuel cell is 2266.5 Hz (1 p.u.). Any frequency lower that the base frequency will be smaller to 1 p.u., instantly revealing the capacitive behavior, whilst frequencies larger than 1 p.u. will mean inductive behavior. These frequencies can be expressed as per-unit values with (4.15)

$$f\,(p.u.) = \frac{f\,(Hz)}{f_b\,(Hz)} \tag{4.15}$$

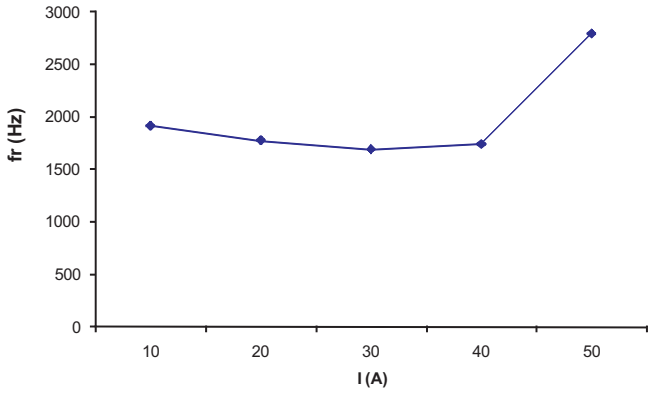

Fig. 4.22: Nexa fuel cell resonance frequency

4.5. Conclusions

Frequency domain tests, such as EIS, are a powerful tool to study the internal behavior of fuel cells. Moreover, it allows to model the fuel cell stack voltage operation through the fitting of an equivalent circuit. After fitting different types of equivalent circuits, the best approximation was found for the model presented. The inclusion of a diffusion element, such as the CPE allowed to fit more precisely the fuel cell impedance Nyquist plot. The suitability of a CPE versus an ideal capacitor has been demonstrated.

It has been observed that the developed temperature model takes into account the fuel cell fan due to the fact that the temperature time-constant decreases for increasing temperature. This is due to the fact that for increasing temperatures the fan sees its duty cycle increased, and causes a faster heat evacuation. However, as seen in the temperature model validation, the model is unable to exactly follow the temperature evolution during very high current loads, and affects the voltage model precision. This issue could be solved with a more detailed cooling model.

Finally, a per-unit system has been defined. Even though this was also presented by Choi, the per-unit system proposed in this work is a more general system, applicable to any type of load. This flexibility is due to the proposal of a base frequency, which can be defined when the current load presents a certain ac component superimposed to the dc operation point. Two different frequencies: cut-off and resonance frequency were studied as

possible base frequency. Finally, the resonance frequency was chosen due to its simple identification in Nyquist and Bode plots, as well as to the resistive impedance of the fuel cell at the resonance frequency. Any frequency lower to 1 p.u. will automatically imply a capacitive fuel cell behavior, whilst any frequency higher to 1 p.u. will include an inductive behavior.

CHAPTER 5

Nonlinear dynamic model for batteries

5.1. Introduction

This chapter presents a nonlinear dynamic model of electrochemical batteries for simulation purposes, in both absolute and relative (per-unit) units, its deduction, development and validation. The battery studied is a sealed lead-acid battery, specially designed for traction purposes by Exide-Tudor [85]. Its principal characteristics are detailed in Table 5.1.

As explained previously a battery is an electrochemical system, which includes multiple aspects, such as thermal effects, fluid dynamics, electrochemical reactions, electrical phenomena, etc. Therefore, the model can be carried out from any of these points of view. However, the objective is to obtain a dynamic model which is able to yield information about its electric behavior, neglecting other effects which could be included. Moreover, it is desirable to obtain a model which can easily interact with other electric or electronic system models.

This electric model will adopt the form of an equivalent circuit which will be able to reproduce its current and voltage dynamic performance. The

Dimensions	Length	260 mm
	Width	173 mm
	Height	207 mm
	Weight	17,5 kg
Rated performance	Reserve capacity	95 min
	C 5h	45 Ah
	C 20h	50 Ah
	SAE CCA (-18ºC)	770 A
	EN CCA (-18ºC)	800 A
	Cycles 2.5 % DOD	more than 200000
	Cycles 17.5 % DOD	more than 3000
	Vibration proof	EN 53342 V3
Description	Connectors	2 conical DIN terminals
	Colour	Grey
	Lid	Flat with centered gas outlet
Others	Charging procedure	20 h/14,4 V+4 h/1,25 A
	Max. recc. voltage	15 V
	Max. disch. load	1000 A (30 s)
	Max. shorcirc. load	1500 A (5 s)

Table 5.1: Characteristics of the battery used

parameters of the resulting equivalent circuit will be obtained through electrochemical impedance spectroscopy EIS tests. Although the work is applied to a lead-acid battery, the experimental methodology and results can be extended to other technologies such as Ni-Mh, Li-ion, etc.

5.2. EIS tests experimental procedure

Electrochemical Impedance Spectroscopy EIS can be also applied to batteries, in a similar way as it was applied for fuel cells. However, the test procedure is slightly different due to the charge/discharge processes. Even if the main duty of a battery is to supply energy through discharge, depending on the final application, re-charging can also be a determinant process. Therefore, the final battery model should be able to reproduce both charge and discharge operation.

As in the case of the fuel cell, the battery current is more easily controlled

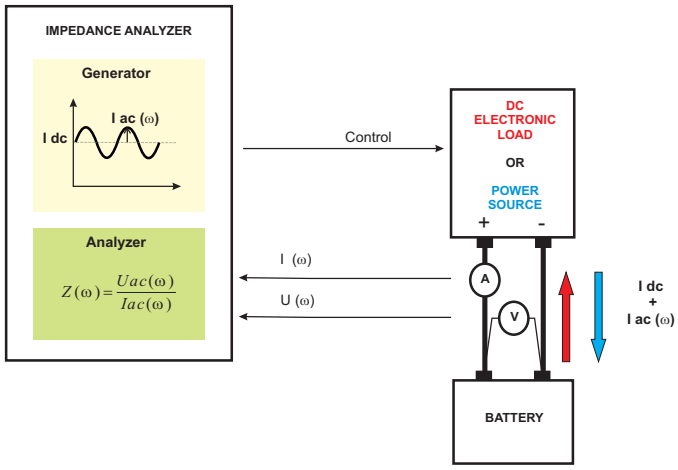

Fig. 5.1: *EIS* on batteries

than the voltage, galvanostatic (current control) mode tests are conducted, as, e.g. done by [64], [15] and [86]. Likewise, the battery is set to its dc operation current and a small signal ac current with variable frequency is superimposed. Both the dc+ac current components cause a dc+ac voltage response, which allows the obtention of the battery complex impedance taking into account only the ac components of the current and voltage signals, as depicted in Fig. 5.1.

5.2.1. DC operation conditions

A battery can operate in a wide range of states of charge (*SoCs*), either during charge or discharge processes within an also wide range of currents and temperatures. These facts play an important role in determining the number of tests necessary to characterize the battery.

A battery *SoC* can vary from fully discharged (0 %) to fully charged (100 %), however, it is not recommended to operate frequently at very low *SoCs* as it shortens the battery life. Therefore, the lower *SoC* at which tests are conducted has been set to 40 %. The selection criterion for the *SoC* upper limit is the battery voltage, which should not exceed the maximum voltage recommended by the manufacturer during charge (14.4 V for the battery under study). For high *SoCs* the battery can easily suffer overvoltage and overcharge; hence, the maximum *SoC* considered is 90 %.

The battery used can either supply or absorb very high currents (up to 1000 A discharge during 30 s). To select the dc operation values at which the EIS tests are carried out, two facts have to be taken into account. The first one is related to the lower current limit. If the lower limit is too small, the results obtained from the model will be incorrect due to the considerable noise component in the current and voltage signals. Therefore, 2.5 A is selected as the minimum dc current. The second fact which must be taken into account is that the test conditions (current, voltage, SoC) should be kept within a narrow interval. For example, if tests are carried out at very high currents, the battery SoC will vary more than 10 % from the beginning to the end of the test, invalidating the results obtained. This will limit the maximum current to 20 A.

The maximum and minimum current operation, the test duration and the room temperature will influence the battery operation temperature. If the battery current is kept low, the test duration is less than 15 minutes, then the battery temperature can be considered to be constant and equal to the room temperature (25°C). Therefore, tests will be carried out for the following operation conditions:

- Process: charge and discharge.
- DC current: 2.5, 5, 10 and 20A.
- SoC: 40, 50, 60, 70, 80 and 90 %.

5.2.2. AC test conditions

As pointed out previously, a current ac signal is superposed to the dc current, allowing to carry out the EIS test during the normal battery operation. However, the ac signal should not disturb substantially the operation conditions (current, voltage, SoC and temperature). Therefore, in all EIS tests the ac selected signal presents a low amplitude which is dependant on the dc operation current. The ac current ripple should be much smaller than the dc current level; therefore, the ac signal amplitude is defined as a certain percentage of the dc operation current. Different ac-dc current relationships can be investigated, as presented in Chapter 3, but for this work the ac signal

amplitude selected is a 5 % of the dc current, as higher values would provoke ac voltages greater than 0.25 % of the rated voltage (12 V) and lower values would present a high noise component [54].

The frequency of the ac ripple is variable and sweeps from its minimum frequency to its maximum frequency. Due to the fact that each of the phenomenon which takes place in a battery is revealed at different frequencies, it is necessary to subject the battery to a frequency sweep. This sweep can vary from low frequencies (μHz) to high frequencies (kHz-MHz), as explained in [87]. However, it is not possible to carry out such a wide interval of frequencies due to the duration of the tests. For example, if very low frequencies were explored, the test time could lengthen for hours, which would provoke a variation of the test conditions, especially in temperature and *SoC*. Therefore, the minimum frequency is set at 0.1 Hz, whilst the maximum frequency is selected at 6 kHz. The upper frequency is selected at 6 kHz as higher frequencies would not reveal more relevant information and above 6kHz the measures include more noise. This is especially true in the case of the electronic load and the power source, which can present difficulties in following high frequency signals.

5.2.3. Experimental setup

To carry out the EIS tests the following equipment has been used:

- Impedance analyzer (Solartron 1260).
- DC electronic load (Chroma 63201: 80 V, 300 A).
- DC power source (Sorensen 20-150E: 20 V, 150 A).
- LEM LA 305-S current transducer.
- $\pm$15 V power source for transducer supply.
- Computer.
- Exide-Tudor 12 V lead-acid battery.

For both the discharge and charge processes, the impedance analyzer controls the whole test through the software Zplot by programming the dc

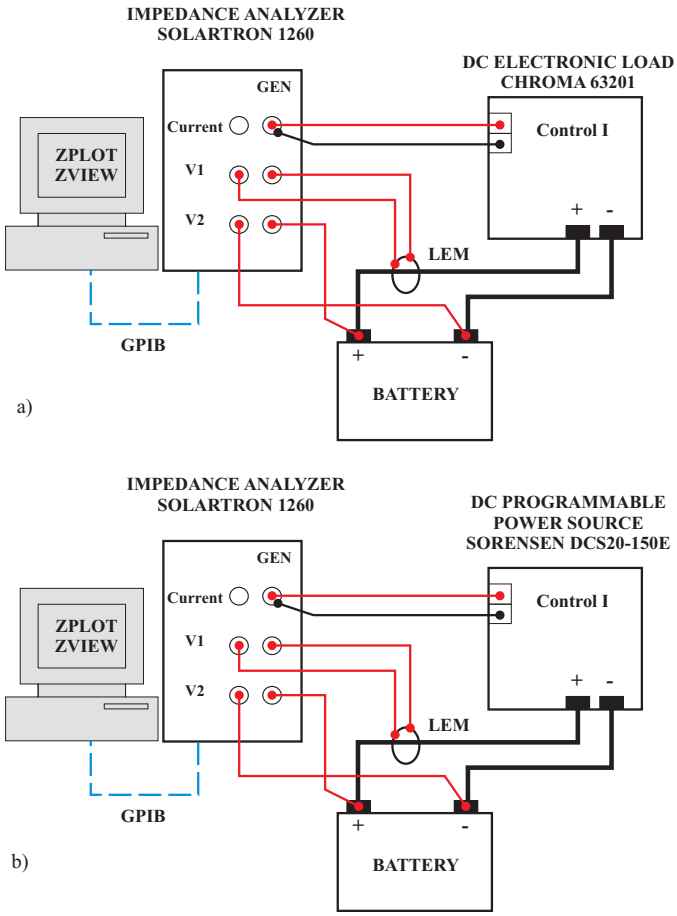

Fig. 5.2: Experimental setup for battery EIS tests for a) discharge b) charge

electronic load (during discharge processes) or the dc power source (during charge processes) externally with a 0-10 V signal, imposing the dc and ac current the battery should sink or supply. The battery current is measured by the LEM transducer and sent to the impedance analyzer, whereas the voltage is directly measured by the impedance analyzer at the battery terminals to avoid the influence of the power cables on the impedance calculation. Fig. 5.2 depicts the power and control connections between the different equipments involved for both charge and discharge tests and Fig. 5.3 shows a photograph of the setup.

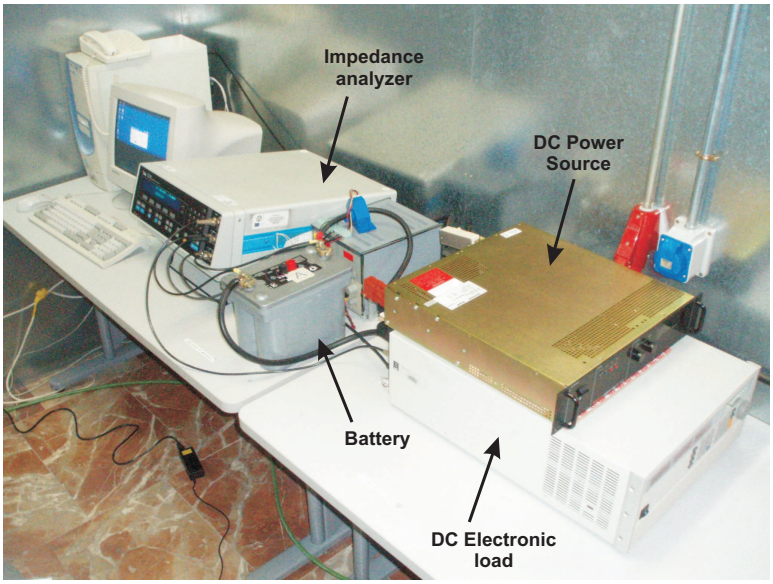

Fig. 5.3: EIS tests experimental setup photograph

5.3. EIS tests results: battery impedance model

EIS tests were conducted for both charge and discharge processes, as it can be found in [16], so two different equivalent circuits are obtained for the battery. Once all the tests are completed, the measurements obtained are processed with the software ZView, licensed by the impedance analyzer manufacturer. This software allows plotting the Nyquist and Bode plots for the battery impedance and adjust it to an equivalent circuit, whose topology is proposed by the user. Figs. 5.4 and 5.5 presents the results for one of the cases, at 70 % SoC at 2.5, 5 and 10 A. Z" represents the imaginary part of the complex impedance while Z′ represents the real part. If Fig. 5.4 is read from the upper to the lower part, it can be observed that the battery shows a capacitive behavior (negative imaginary part) at low frequencies, whilst it behaves as an inductive impedance (positive imaginary part) at higher frequencies.

The capacitive behavior is reflected by a curve which resembles two circumferences, one with a smaller diameter than the other, as reflected in Fig. 5.6, and also reported by [16], [64], [88], [67]. The maximum of each circumference corresponds to the so called cut-off frequency, which corresponds to

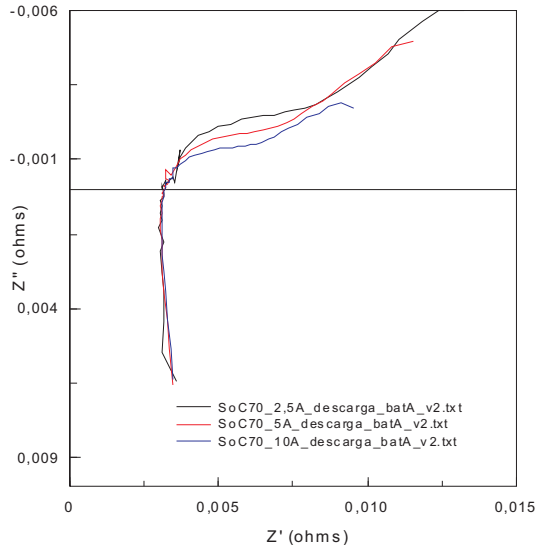

Fig. 5.4: Nyquist diagram for 70 % SoC during discharge

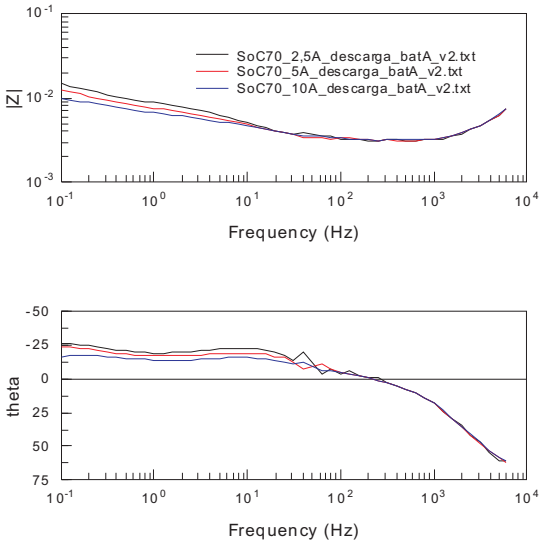

Fig. 5.5: Bode diagram for 70 % SoC during discharge

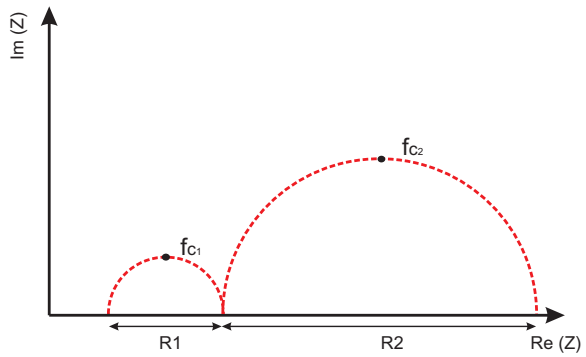

Fig. 5.6: Approximation of the Nyquist plot

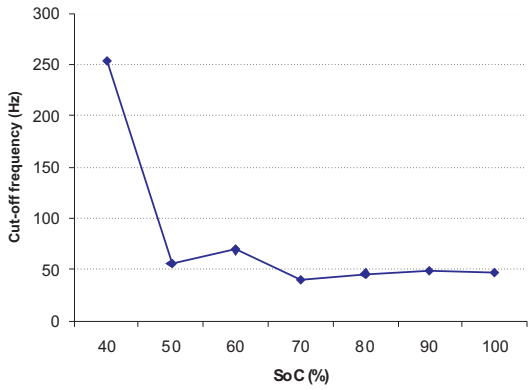

Fig. 5.7: Cut-off frequency evolution with SoC

the point where the imaginary part of the RC network impedance reaches its maximum value. The cut-off frequency is not constant, but shows a well defined trend, as a function of the SoC for the anode electrode which is shown in Fig 5.7. The frequency is high for low $SoCs$, and is around 50 Hz for the rest of $SoCs$.

As seen in Chapter 3, a circumference in a Nyquist plot corresponds to a RC network. In this case, there are two different circumferences and each of them corresponds to a different RC network.

The bigger circumference can be encountered at low frequencies, which can range from 100 μHz to 1 Hz (from 0.1 Hz in this work). At these frequencies the dominant phenomenon is the diffusion inside the porous electrodes [89]. As reported by [87], diffusion can be located either in the electrolyte or the electrodes. Diffusion is created in the electrolyte due to the move-

ment of ions, which must travel from the electrode were they are produced to the other electrode, in which they are consumed. However, the most relevant diffusion takes part in the electrodes. As electrodes are porous, the electrochemical reaction can take place both inside or on the surface of the electrode, and is precisely this fact summed up with the presence of pores which provoke the diffusion. More information about these phenomena can be consulted in [39], [69].

The smaller circumference which represents an RC network describes the behavior at intermediate frequencies (from 1 Hz to 1 kHz) and represents the charge transfer reaction and the double layer capacitance, which occur in parallel due to the fact that both the double-layer capacitor and the electrochemical charge transfer appear on the electrode surface [89].

The double layer capacitor is similar to the one described for the fuel cell and can be represented as a capacitance in parallel to the charge transfer resistance.

The inductive behavior of the battery appears at high frequencies (> 1 kHz) and is represented in the Nyquist plot by a line, which is not totally vertical, but slightly curved to the right. This small curvature is due to the skin effect present at very high frequencies. At these frequencies, the penetration depth of the current in the conductors lessens, increasing the real part of the complex impedance. This penetration depth depends on the material proprieties, particulary on the inverse of the conductivity square root and the inverse of the frequency square root [87].

When the imaginary part of the impedance is zero, the impedance becomes purely resistive. This point represents the smallest impedance value for the whole curve. The corresponding frequency (resonance frequency) is not constant, but dependant on the battery SoC, and is depicted in Fig. 5.8 from the EIS test carried out. As it happened for the cut-off frequency, the value for low $SoCs$ is higher than for the rest of $SoCs$. This trend has also been observed by [72]. For the battery studied in this Thesis, the resonance frequency is comprised between 265 Hz and 190 Hz.

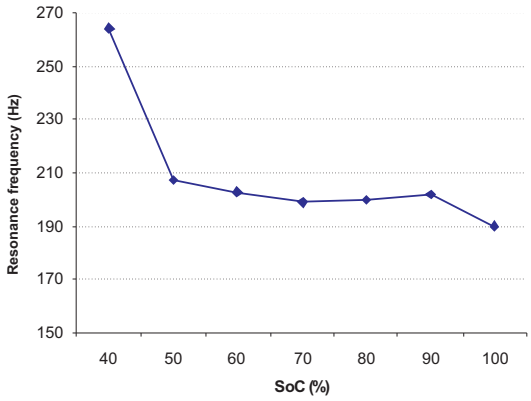

Fig. 5.8: Resonance frequency evolution with SoC

With the Nyquist plots for the all the $SoCs$ at the different currents, an equivalent circuit, as the one shown in Fig. 5.9 can be obtained for each of the EIS tests.

Once all the EIS tests data has been process with ZView, as shown in Fig. 5.9, it is possible to study the effect of current and SoC on the battery impedance. To do so, the statistical software, Statgraphics, is used. A multivariable analysis has been carried out for each parameter of the equivalent circuit. For example, the statistical analysis carried out for R_2 is displayed in Fig. 5.10.

One of the plots returned by Statgraphics is the Observed vs. Predicted chart, in which the best possible plot is when all the points are on the 45º line, which would mean that the model parameters are identical to the observed values.

With the previous results a passive dynamic nonlinear model for the battery which distinguishes a charge from a discharge process is obtained and depicted in Fig. 5.11. The parameters equations during discharge are given in (5.1).

Element	Freedom	Value	Error	Error %
L	Free(+)	1,8589E-7	3,7982E-9	2,0433
Rohm	Free(+)	0,0034064	3,2615E-5	0,95746
R1	Free(+)	0,010322	0,00068629	6,6488
C1	Free(+)	171,8	6,7805	3,9467
R2	Free(+)	0,0026366	7,3451E-5	2,7858
C2	Free(+)	4,421	0,2483	5,6164

Chi-Squared:	0,0088829
Weighted Sum of Squares:	0,81723
Data File:	D:\TESIS\ENSAYOS\ENSAYO EIS BATERIA\CON SE
Circuit Model File:	D:\TESIS\ENSAYOS\ENSAYO EIS BATERIA\CON SE
Mode:	Run Fitting / Freq. Range (0,1 - 6000)
Maximum Iterations:	100
Optimization Iterations:	0
Type of Fitting:	Complex
Type of Weighting:	Calc-Modulus

Fig. 5.9: Equivalent circuit obtained through ZView

$$
\begin{aligned}
L(H) &= 1{,}72 \cdot 10^{-7} - 2{,}25 \cdot 10^{-11} \cdot SoC \\
R_{ohm}(\Omega) &= 4{,}25 \cdot 10^{-3} - 6{,}13 \cdot 10^{-7} \cdot SoC^2 + 5{,}68 \cdot 10^{-7} \cdot SoC^3 \\
R_1(\Omega) &= 0{,}013 - 1{,}51 \cdot 10^{-3} \cdot I + 6{,}06 \cdot 10^{-5} \cdot I^2 + 2{,}24 \cdot 10^{-7} \cdot SoC^2 \\
C_1(F) &= 174{,}131 - 0{,}42 \cdot I^2 - 0{,}21 \cdot SoC^2 + 4{,}73 \cdot 10^{-3} \cdot SoC^3 - 2{,}68 \cdot 10^{-5} \cdot SoC^4 \\
R_2(\Omega) &= 9{,}30 \cdot 10^{-4} - 7{,}15 \cdot 10^{-5} \cdot I^2 + 5{,}45 \cdot 10^{-6} \cdot I^3 + 1{,}61 \cdot 10^{-6} \cdot SoC^2 - \ldots \\
&\quad \ldots - 1{,}22 \cdot 10^{-8} \cdot SoC^3 \\
C_2(F) &= 5{,}74 + 0{,}01 \cdot I^2
\end{aligned}
\tag{5.1}
$$

5.4. Tests for the determination of the battery internal voltage

The battery equivalent circuit shown in Fig. 5.11 is a passive circuit, which needs a power source or similar element to represent the active nature of the battery. This active element is a voltage source which represents the open circuit voltage OCV, which is dependant on the SoC, as recorded in the literature by [90], [16] and [91].

Multiple Regression Analysis

Dependent variable: R2

Parameter	Estimate	Standard Error	T Statistic	P-Value
CONSTANT	0,0101726	0,00420623	2,41845	0,0420
I^2	0,0000319902	0,00000559691	5,71569	0,0004
SOC	-0,000431785	0,000151369	-2,85254	0,0214
SOC^2	0,00000545876	0,00000130864	4,17132	0,0031

Analysis of Variance

Source	Sum of Squares	Df	Mean Square	F-Ratio	P-Value
Model	0,0000755932	3	0,0000251977	52,95	0,0000
Residual	0,00000380678	8	4,75848E-7		
Total (Corr.)	0,0000793999	11			

R-squared = 95,2056 percent
R-squared (adjusted for d.f.) = 93,4076 percent
Standard Error of Est. = 0,000689817
Mean absolute error = 0,00045577
Durbin-Watson statistic = 1,19645

The StatAdvisor

The output shows the results of fitting a multiple linear regression model to describe the relationship between R2 and 3 independent variables. The equation of the fitted model is

R2 = 0,0101726 + 0,0000319902*I^2 - 0,000431785*SOC + 0,00000545876*SOC^2

Since the P-value in the ANOVA table is less than 0.01, there is a statistically significant relationship between the variables at the 99% confidence level.

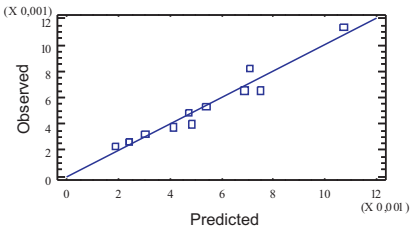

Fig. 5.10: Statistical analysis for R_2

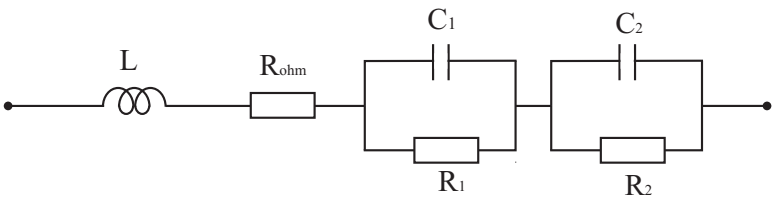

Fig. 5.11: Equivalent circuit for the battery impedance

This relationship between the OCV and the SoC differs also during charge/discharge process. When the whole charge/discharge cycle is considered, this causes a sort of hysteresis effect on the OCV curve due to the battery surface charge. In fact,when the battery is charged, the charge accumulates on the electrode surface and then diffuses through the electrodes [16], [91]. This diffusion process is slower than the ions transport across the electrolyte, provoking a charge accumulation on the electrode surface, and hence an increase of the battery voltage. This phenomenon is rarely taken into account by other authors, even if it does affect the final accuracy of the model.

To calculate the OCV for the battery under study after a charge or discharge process, the battery is charged to a 100 % SoC following the standard UNE-EN 50342-1 [92], which details that the battery should be charged with a constant voltage of 14.4 V during 20 h, with a $5{\cdot}I_{rated}$ current limitation, followed by a constant current charge of $0.5{\cdot}I_{rated}$ during 4 h.

To obtain the OCV curve after a discharge process, successive pulse discharges of 10 A with 15 min rest between pulses were applied to the battery until the 30 % of SoC was reached, as detailed in Table 5.2.

From the SoC reached at the end of the previous tests, successive charging current pulses are applied with 45 minutes rest between pulses. In this case the rest time is longer than after a discharge due to the slower diffusions processes. During this process, the charge current is reduced for increasing SoC to avoid overvoltage, which could endanger the battery. Another difference with the discharge procedure is that for a charge process the charge efficiency should be taken into account. This efficiency reflects that not all the energy injected to the battery is used for its charging due to the effect of irreversible processes such as gasification during overcharging [93]. The charge efficiency is smaller for high $SoCs$, when the battery presents a higher opposition to accept charge, needing small values of currents during large periods of time to complete the charging process. The experimental procedure for the OCV obtention after a charge process is detailed in Table 5.3.

The hysteresis curve for the OCV obtained is depicted in Fig. 5.13. The

SoCinitial (%)	ΔSoC (%)	SoCfinal (%)	Discharge time* (h)
100	5	95	0.25
15 min rest			
95	5	90	0.25
15 min rest			
90	10	80	0.5
15 min rest			
80	10	70	0.5
15 min rest			
70	10	60	0.5
15 min rest			
60	10	50	0.5
15 min rest			
50	10	40	0.5
15 min rest			
40	5	35	0.25
15 min rest			
30	5	30	0.25

*Discharge time: $t\,(h) = \frac{\Delta SoC(\%) \cdot C_n}{I(A) \cdot 100}$

Table 5.2: Experimental procedure to calculate the OCV after discharge

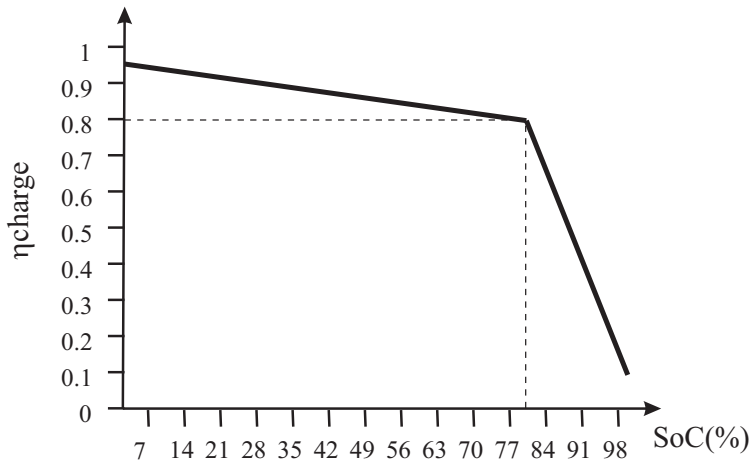

Fig. 5.12: Charge efficiency

SoCinitial (%)	ΔSoC (%)	SoCfinal (%)	I (A)	η	Charge time* (h)
30	5	35	20	0.89	0.14
45 min rest					
35	5	40	20	0.884	0.14
45 min rest					
40	10	50	20	0.875	0.285
45 min rest					
50	10	60	10	0.856	0.584
45 min rest					
60	10	70	5	0.83	1.2
45 min rest					
70	10	80	5	0.818	1.22
45 min rest					
80	10	90	1	0.8	6.25
45 min rest					
90	5	95	0.5	0.45	11.11
45 min rest					
95	5	100	0.5	0.275	18.18

*Discharge time: $t\,(h) = \frac{\Delta SoC(\%) \cdot C_n}{\eta \cdot I(A) \cdot 100}$

Table 5.3: Experimental procedure to calculate the OCV after charge

equations obtained with Statgraphics for the charge and discharge cycle are presented in (5.2), whilst the observed versus predicted curves for each equations are shown in Fig. 5.14. The determination of the OCV completes the development of the active model.

$$\begin{aligned} OCV_{dis.} &= 11{,}5648 - 0{,}00759 \cdot SoC + 0{,}00148 \cdot SoC^2 - ... \\ &\quad ... - 3{,}5 \cdot 10^{-5} \cdot SoC^3 + 3{,}61 \cdot 10^{-7} \cdot SoC^4 - 1{,}34 \cdot 10^{-9} \cdot SoC^5 \\ OCV_{char.} &= 13{,}9733 - 0{,}3276 \cdot SoC + 0{,}01769 \cdot SoC^2 - ... \\ &\quad ... - 4{,}1 \cdot 10^{-4} \cdot SoC^3 + 4{,}4 \cdot 10^{-6} \cdot SoC^4 - 1{,}79 \cdot 10^{-8} \cdot SoC^5 \end{aligned} \tag{5.2}$$

5.5. Complete battery model

The final structure of the active nonlinear dynamic model of the battery is represented in Fig. 5.15. The voltage at the battery terminals is calculated

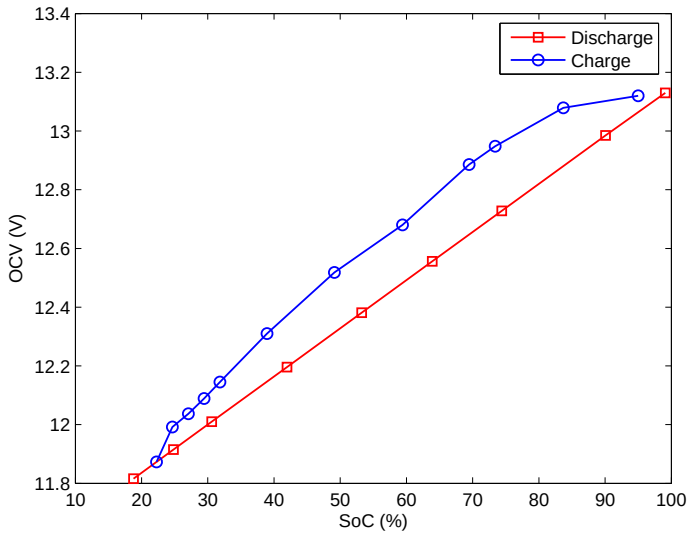

Fig. 5.13: Hysteresis curve for OCV

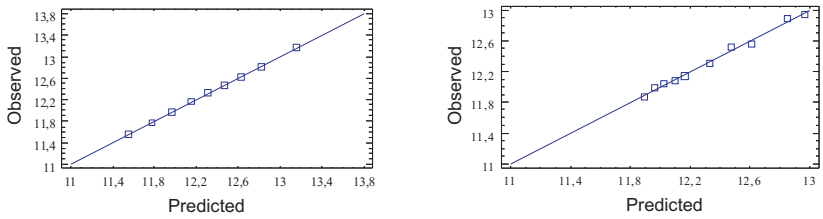

Fig. 5.14: Statgraphics observed vs. predicted curves for OCV during discharge (left) and charge (right)

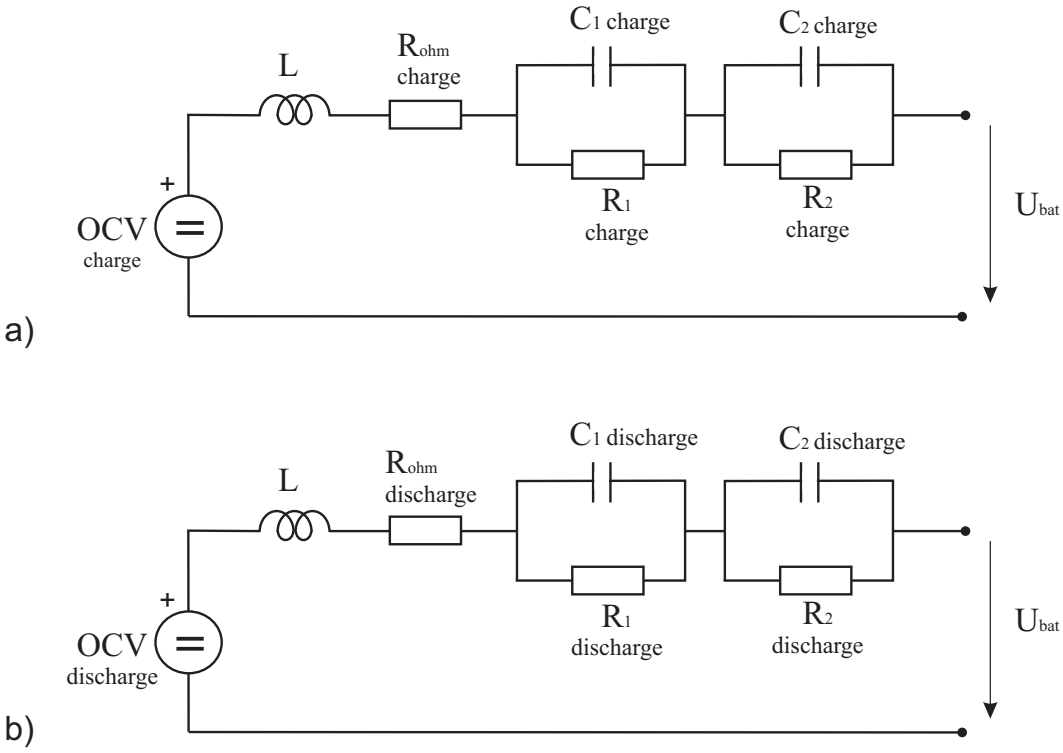

Fig. 5.15: Active equivalent circuit of the battery for a)charge and b)discharge

in (5.3).

$$\begin{aligned} U_{bat} &= OCV - U_L - U_{R_{ohm}} - U_{C_1} - U_{C_2} \\ U_L &= L \cdot \frac{dI}{dt} \\ U_{R_{ohm}} &= R_{ohm} \cdot I \\ U_{C_1} &= \int \frac{1}{C_1} \cdot \left(I - \frac{U_{C_1}}{R_1} \right) \cdot dt \\ U_{C_2} &= \int \frac{1}{C_2} \cdot \left(I - \frac{U_{C_2}}{R_2} \right) \cdot dt \end{aligned} \tag{5.3}$$

5.5.1. State of charge calculation

To reproduce the behavior of a battery, not only the voltage dynamic should be emulated, but also the battery state of charge *SoC*, which is a percentage of the rated capacity and indicates the battery useful capacity.

The battery *SoC* calculation is not a trivial issue [94], [69], especially for non-flooded batteries, as, the acid concentration of the electrolyte, which is

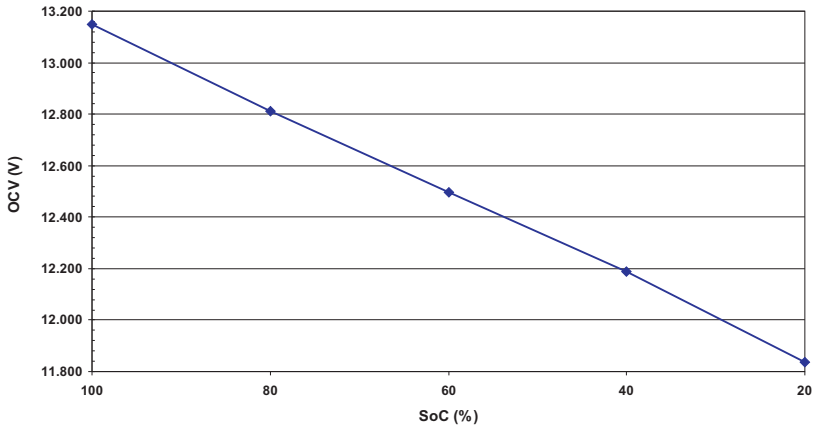

Fig. 5.16: OCV vs. SoC

a good indicator of the battery SoC, cannot be directly measured. Hence, the SoC needs to be estimated indirectly, through the measurement of other variables such as current and time or voltage.

In this Thesis two methods for the calculation of the SoC have been applied. In the first method the SoC is linearly dependant on the open circuit voltage OCV, as depicted in Fig. 5.16, which was an information supplied by Exide-Tudor. The advantage of this method is its simplicity, however, it presents a serious drawback, related to the time the battery should rest before the OCV can be measured. This rest time is needed to allow diffusion phenomena to take place in order to allow the voltage to reach its steady state point. Depending on the process which the battery has suffered previous to the OCV measurement, the rest time can vary from 30 minutes if a discharge has taken place before, to hours if it was a charging process. This rest time can be critical for certain applications, such as electric or hybrid vehicles, in which the driver cannot wait hours to know the battery SoC. Therefore, this method can only be applied before the use of the battery, to calculate the initial SoC, or after a full recharge.

The second method used to measure the SoC consists in the integration of the battery current with respect to time. This method can be applied under operating conditions, provided the initial SoC is known due to the

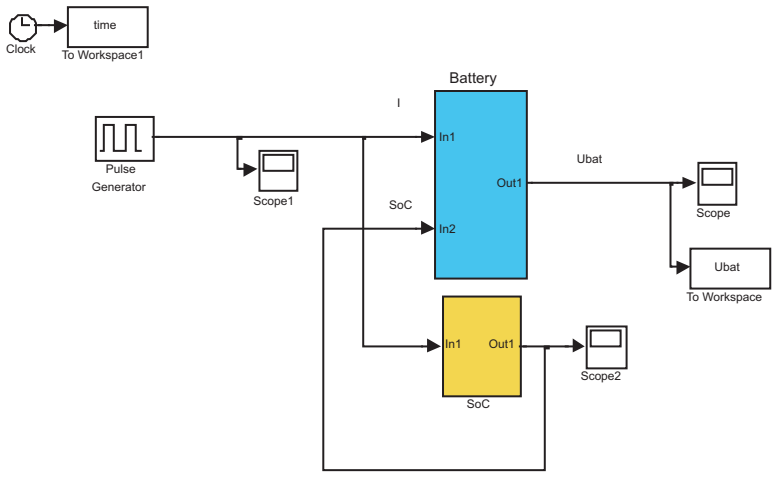

Fig. 5.17: Matlab/Simulink model for the battery

OCV measurement.

$$SoC_t(\,\%) = SoC_{t-1} \pm \frac{\eta}{C_n} \cdot \int_{t-1}^{t} I(t)dt \cdot 100 \tag{5.4}$$

The equation takes into account the previous SoC and the charge efficiency η.

The model obtained for the battery is implemented in Matlab/Simulink, taking into account the different parameters of the equivalent circuit, that may be different if the process is either a charge or discharge one. Figs. 5.17 and 5.18 represent the block model in Matlab/Simulink. The current profile in Fig. 5.19 has been applied to the real battery and model, and the experimental and modeled voltage profile obtained is depicted in Fig. 5.20.

If instead of a discharge cycle the battery undergoes a charge cycle, the charge current profile is depicted in Fig. 5.21 and the corresponding experimental and modeled voltage in Fig. 5.22.

5.6. Per-unit approach to batteries

All the battery models developed heretofore, including the one described above represent the electrical behavior of batteries by means of an equivalent circuit whose variables include voltages (V), currents (A), impedances (Ω)

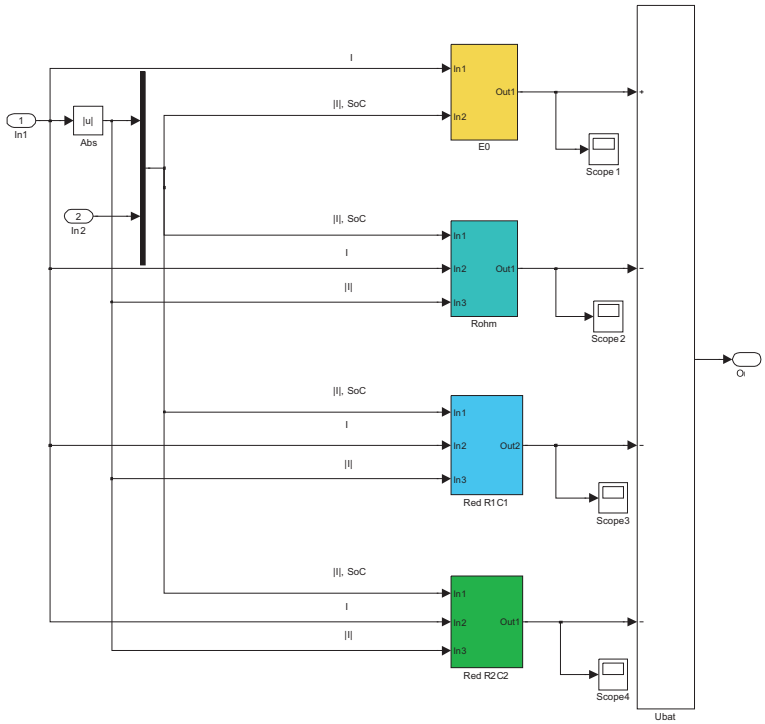

Fig. 5.18: Detail of the Matlab/Simulink model

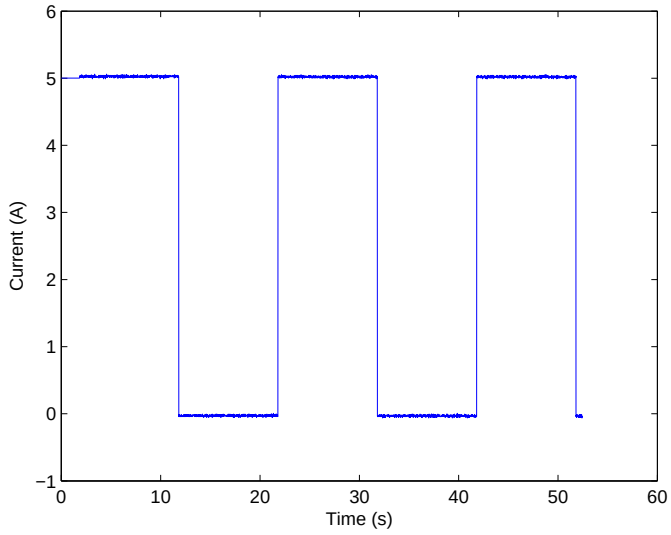

Fig. 5.19: Discharge current profile required to the battery

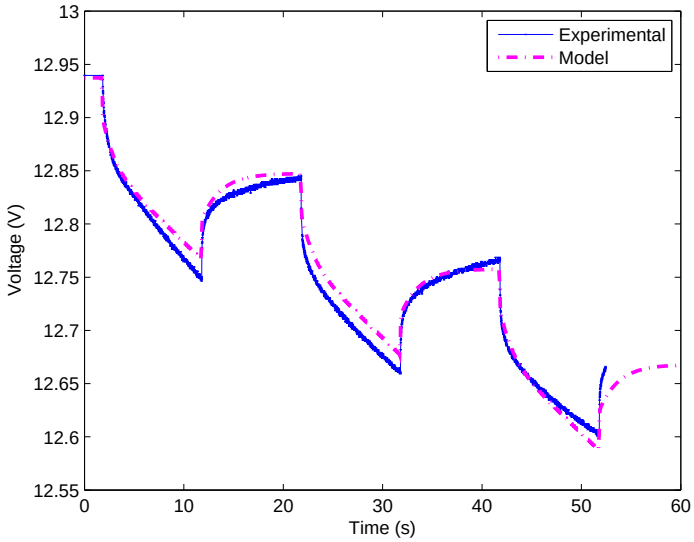

Fig. 5.20: Experimental and modeled battery voltage during discharge

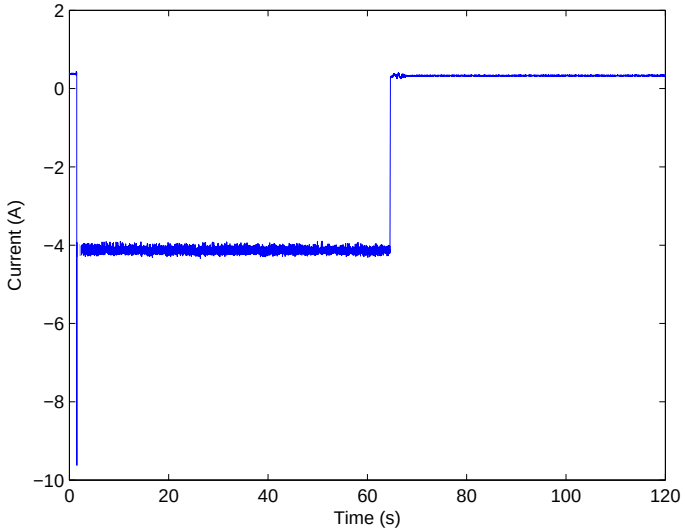

Fig. 5.21: Charge current profile injected in the battery

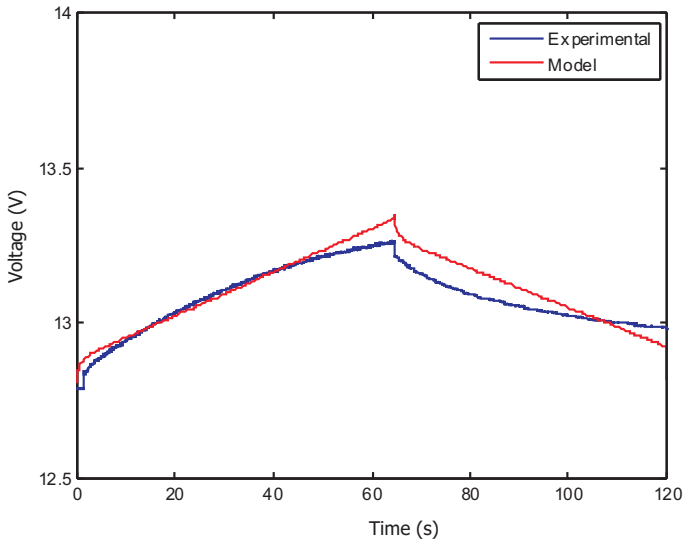

Fig. 5.22: Experimental and modeled battery voltage during charge

and power (W), i.e. in absolute magnitudes. This approach corresponds to the basic way power engineers solve electrical circuits and power systems.

But this classic approach needs to be changed when energy storage systems, such as batteries are incorporated to a power system. With this classic point of view, the general assumption is that the energy delivered by the power sources is unlimited. This may be true for other power sources, but not for batteries or other energy storage system. Apart from voltage, current, power and impedance storage systems are not completely defined without an additional variable: the available energy stored and ready to be delivered at a given instant.

For the analysis of power systems which present different voltage levels, the usual way to describe the variables is in per-unit values (p.u.) relative to a defined set of base values. The usual set of variables are power, voltage, current and impedance. However, when energy comes into play a new base magnitude needs to be included: the base time. Time is taken into account in the variable "battery capacity", expressed in Amperes hour (A·h), which is the product of the rated current times the rated discharge time. Therefore, the classic base magnitudes have to be revised and new magnitudes included.

Author	Voltage (V)	Capacity (A·h)	*Rohm* (mΩ)
Blanke [72]	12	70	5.2
Gauchia	12	50	3.2
Hariprakash [71]	6	4	75
Karden [88]	4	100	0.6
Salkind [15]	12	100	6.5
Salkind [15]	6	10	5

Table 5.4: Comparison between different authors

Curiously, there is a mixture of per-unit and absolute variables which have been used by both electrochemical and power engineers. For example, voltage is expressed in V, current in A, but battery state of charge is defined as a percentage, that is, a dimensionless variable. In most cases, for electrochemical systems, power engineers inherit the vocabulary established by electrochemical engineers, even if an obvious different focus is given, but no in depth transformation has been done to adapt the inherited variables to the power engineering world. Furthermore, the current situation collides with the usual way power engineers use to represent and analyze the electrical power system.

The drawbacks of this mixed per-unit and absolute variables are clearly exposed when a comparison between the performance of batteries with different characteristics, or a sizing calculation is carried out. The variables, such as voltage, capacity, impedance, power, etc. can assume a wide range of values as they are dependant on the overall size of the system, defined by its rated capacity, voltage or current. For example, if one of the parameters of the equivalent circuit calculated previously is compared to those obtained by other authors, no clear conclusion about the correctness of the results can be concluded. Table 5.4 presents the results for the ohmic resistance at 70 % obtained by several authors.

Analyzing Table 5.4, no clear relationship can be extracted, as batteries with similar voltages and capacities exhibit very different impedances. Therefore, how can any author compare its results to those obtained by other authors?

This Thesis proposes the application of a per-unit system to batteries to

overcome these problems, explaining the need to use two different base times, in order to represent phenomena which occur in different time horizons, as it is the case of the long-term charge/discharge processes versus the transient phenomena. To this end, an equivalent circuit for a battery will be developed and its parameters will be calculated and represented as per-unit values. Finally, the proposed methodology will be applied to different cases referred in the bibliography and compared with experimental results obtained for this work.

5.6.1. Steady-state per-unit system for a battery

For energy storage devices such as batteries, the usual base variables used (voltage, current, power and impedance) is inadequate, as a base value for the energy stored or released by the battery must be defined. Hence, it is essential to introduce the concept of capacity, which is related with the discharge duration according to the Peukert equation [62].

$$C \cdot I^{pc-1} = constant \tag{5.5}$$

Where C is the rated capacity, I the current and pc the Peukert coefficient (usually between 0.5 and 2), which is unique for each technology and model. The equation reveals that the available capacity at constant discharge current is reduced for increasing discharge rates.

Therefore, a new set of base magnitude which includes a base capacity C_b related to a discharge time t_b must be created. Known the base capacity and the discharge time (information which can be easily found in the data sheet handed by the manufacturer), the base current can be obtained.

$$I_b\,(A) = \frac{C_b}{t_b} \tag{5.6}$$

If the "natural" choice of taking the open circuit voltage as base voltage is adopted, the rest of base values can be obtained, completing the set of base values necessary to describe the battery performance for stationary operation. All the base values are presented in Table 5.5. Evidently, if three values are suitably selected, the rest of the base values can be calculated. However, the selection criterion of the first three base values is not arbitrary as the base

Base capacity	Base discharge time	Base current	Base voltage	Base power	Base impedance
C_b (A· h)	t_b (h)	I_b (A)	U_b (V)	P_b (W)	Z_b (Ω)

Table 5.5: Proposed base variables for a battery

Author	U (V)	C (Ah)	t (h)	R (mΩ)	Ib (A)	Zb (Ω)	R (p.u.)
Blanke	12	44	20	5,2	2,2	5,45	0,95
Gauchia	12	50	20	3,2	2,5	4,8	0,67
Hariprakash	6	4	5	75	0,8	7,5	10
Karden	4	100	10	0,6	10	0,4	0,24
Salkind	12	100	20	6,5	5	2,4	2,7
Salkind	6	10	20	5	0,5	12	0,42

Table 5.6: Proposed base variables for a battery

values must be linearly independent.

$$P_b = U_b \cdot I_b \qquad Z_B = \frac{U_b}{I_b} \tag{5.7}$$

Table 5.6 completes Table 5.4 by adding the base magnitudes and by expressing the resistances in p.u. values. The base current is calculated known the discharge time for which the capacity is defined. The base impedance can be calculated as the ratio of the base voltage (rated value) and base current.

The comparison between the resistance values in absolute and per-unit values yields different information about the relationship between them. For example, the resistance obtained by Karden is one order of magnitude smaller than the one presented by Blanke or the obtained in this Thesis. No linear relationship can be found with voltage or capacity, which was also pointed out by Karden [88]. However, the three mentioned values are near enough when compared as p.u. values. Therefore, the comparison between absolute values can be misleading, as the capacity of the batteries influences, for example, the impedance.

5.6.2. Per unit representation of the discharge curve

The discharge curve is an extended representation of the evolution of the battery voltage with the discharged capacity. Its frequent use makes it ad-

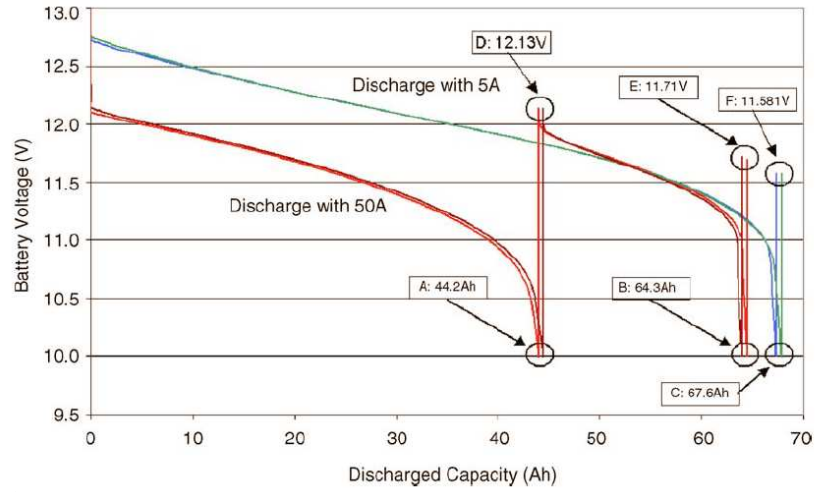

a)

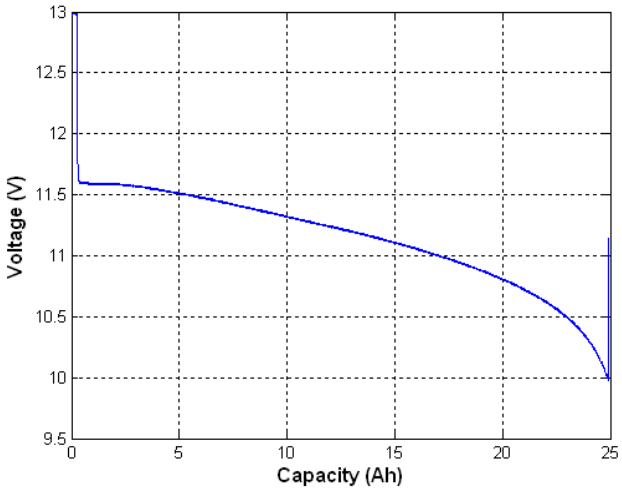

b)

Fig. 5.23: Discharge curve obtained by a)Doerffel and b)Gauchia in absolute values

visable to define it in per-unit values, in order to allow a direct comparison between curves obtained for different batteries, which can proceed from different manufacturers or can be from different technologies.

Fig. 5.23 a, taken from Doerffel [63] represents experimental results in which a battery apparently discharged at high discharge rate can be further discharged at a lower discharge rate, all variables being expressed in absolute values in the original work. Fig. 5.23 b represents a discharge curve obtained for the Exide-Tudor battery used in this Thesis.

Base capacity	Base discharge time	Base current	Base voltage	Base power	Base impedance
45 A· h	5 h	9 A	12 V	108 W	1.33 Ω

Table 5.7: Base values for the Exide-Tudor battery studied

Base capacity	Base discharge time	Base current	Base voltage	Base power	Base impedance
65 A· h	20 h	3.25 A	12 V	39 W	3.69 Ω

Table 5.8: Base values for the BLA1 battery used by Doerffel

Comparing these two figures, there is apparently no relationship between them, as e.g., the discharged capacity and current are different, as Doerffel discharges its battery at 50 A and the Exide-Tudor battery is discharged at 138.42 A. However, if a per-unit system is defined and the same curves are compared in per unit values, other conclusions may be extracted. For both cases a set of base values are presented in Tables 5.7 and 5.8.

For these base values the same curves can be depicted as in Fig. 5.24, in which a simple comparison can be made. If the absolute value of both discharge currents are expressed as per-unit values, both batteries are then discharged with a 15.38 p.u. current. With the same per-unit current the Exide-Tudor battery presents a higher activation voltage drop, which is the voltage drop present at the beginning of the discharge. However, the Exide-Tudor discharges an 18 % less capacity than the battery of Doerffel, even though the battery used by Doerffel has nearly 31 % more rated capacity.

For example, the battery tested by Doerffel has a discharged capacity of 44.2 Ah, but this value does not give any information about the remaining capacity without an explicit reference to the rated capacity of the battery. On the other hand, 0.68 p.u. as the discharge capacity contains all the necessary information, as it is already referred to the rated capacity, once the set of base values are stated once and for all. Expressing all the results as p.u. values has an added value, as it allows a simple and direct comparison with similar work carried out by different authors, with different batteries, which can have very different characteristics (rated capacity, open circuit voltage, discharge time, etc).

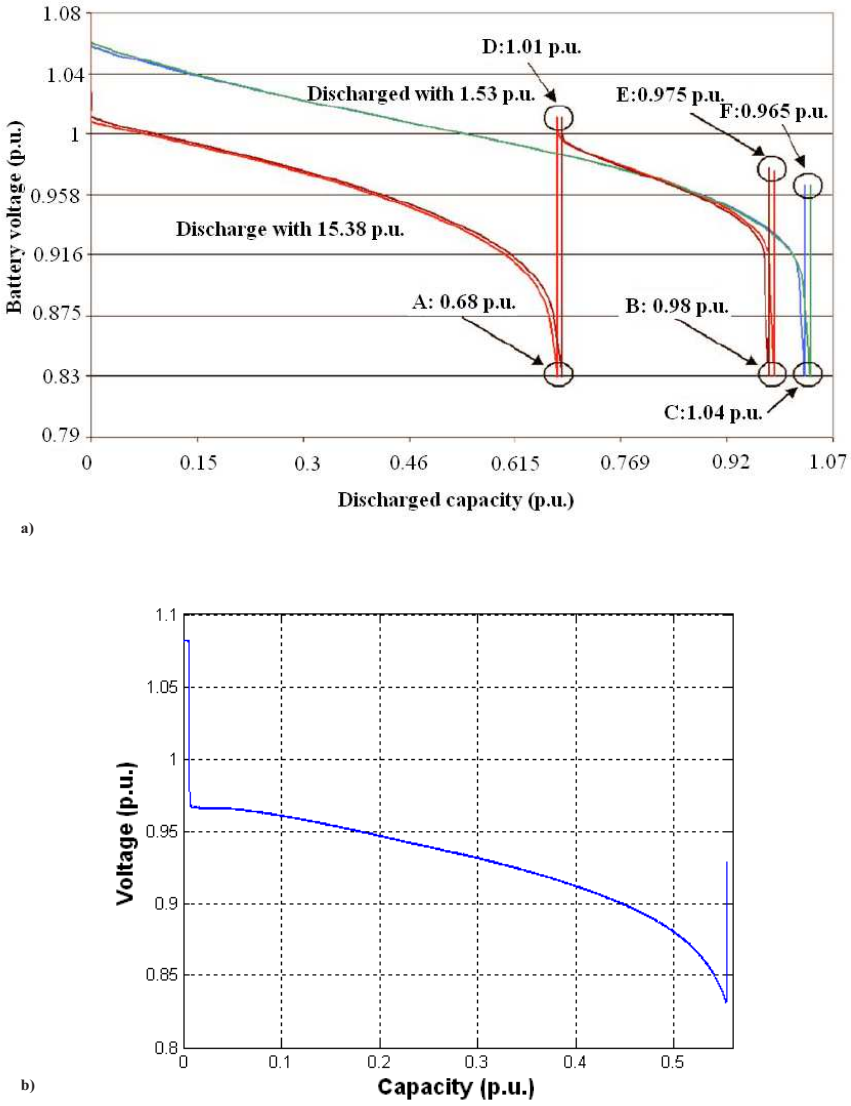

Fig. 5.24: Discharge curve obtained by a)Doerffel and b)Gauchia in p.u. values

5.6.3. Per-unit approach during alternate loads

The per-unit model and base magnitudes obtained in the previous section are especially useful for the interaction of the battery with other power systems also expressed in per-unit values. However, the dynamic behavior and internal processes of the battery include phenomena whose time horizon can be shorter than the 5 hours base time obtained previously. Hence, a more appropriate base system can be obtained to represent, study and compare

the internal electrochemical dynamic behavior of the battery.

This second temporal horizon is straightforward after conducting the EIS tests, as the most relevant phenomena takes place between 0.1 Hz and 6 kHz. For this frequency interval, the corresponding time range is 10 s and 0.16 ms, which is between three and seven orders of magnitude smaller than the 5 h discharge time horizon.

The dynamic time horizon is related to the frequency at which the dynamic processes occur. So a base frequency can be defined as a new base variable, which was not included in the previous base values due to the fact that these were defined for stationary values. However, the internal behavior of the battery is clearly dependant on the frequency, as reflected by the Nyquist plot. Hence, a criterion for the selection of the base frequency should be established. Studying the Nyquist plot, there are three singular candidate points to be considered. The first and second one are the cut-off frequencies for R_1C_1 and R_2C_2, defined as:

$$f_{c1} = \frac{1}{R_1 C_1} \qquad f_{c2} = \frac{1}{R_2 C_2} \tag{5.8}$$

The third possible point is the resonance frequency, defined as the frequency at which the capacitive and inductive impedances cancel each other, and therefore the battery impedance becomes purely resistive:

$$\begin{aligned} Z_{total}(\omega) = &\left[R_{ohm} + \frac{R_1}{1+\omega^2 C_1^2 R_1^2} + \frac{R_2}{1+\omega^2 C_2^2 R_2^2}\right] + ... \\ &... + j\omega \cdot \left[L - \frac{C_1 R_1^2}{1+\omega^2 C_1^2 R_1^2} - \frac{C_2 R_2^2}{1+\omega^2 C_2^2 R_2^2}\right] \end{aligned} \tag{5.9}$$

$$\mathrm{Re}\left[Z\left(\omega\right)\right]_{\omega=\omega_r} = R_{ohm} + \frac{R_1}{1+(2\pi f_r)^2 C_1^2 R_1^2} + \frac{R_2}{1+(2\pi f_r)^2 C_2^2 R_2^2} \tag{5.10}$$

The choice of the resonance frequency as the base frequency has a relevant advantage compared to the cut-off frequency, which is the simple identification in the Nyquist plot where $\mathrm{Im}[\mathrm{Z}(\omega)] = 0$, or in the Bode plot, where $\omega = 0$. As seen in Fig. 5.8, the resonance frequency is variable, as it decreases with increasing state of charge; therefore, one point of the curve must be selected as base frequency. Considering that the rest of base magnitudes

were selected for rated values and fully charged battery, it is logical to infer that the base frequency should also be selected for a fully charged battery. Therefore, the base frequency chosen for our Exide-Tudor battery is 189.87 Hz.

Known this base frequency, the frequencies magnitudes can be expressed in per-unit values for the rest of points of the EIS tests, if e.g. one point is at 400 Hz, its per-unit frequency would be 2.01 p.u. As it happened with the rest of per-unit magnitudes, knowing the per-unit frequency reveals more information than the absolute frequency. 2.01 p.u. means that the battery behavior is inductive, as the per-unit frequency is larger than 1 p.u., whilst 400 Hz does not give this information.

5.7. Conclusions

EIS tests were also applied to model the dynamic nonlinear behavior of batteries. A high number of tests were necessary due to the fact that batteries can present a wide range of states of charge, as well as accept an also wide range of currents. For both situations, charge and discharge processes were tested. However, time domain tests were also necessary to obtain the open circuit voltage hysteresis effect. This effect is rarely taken into account but can affect the resulting accuracy of model.

The direct comparison in absolute values of the equivalent circuit parameters renders confusing results due to the disparity of voltages and capacities. Therefore, in this Thesis we propose a per-unit system to correctly carry out this comparison, which, up to now, has not been found in literature. The per-unit system proposed includes, apart from the classical base voltage, current, power and impedance, a base time. Time is a key variable in batteries, due to the limited amount of reactants contained in the battery casing, and is related to capacity and current.

Batteries, as fuel cells, generate dc power. However, they can also accept, up to some extent, a certain amount of ac component superimposed on the dc current load. This ac current load frequency will influence the battery impedance behavior, and should therefore be taken into account. Through

the EIS tests carried out it is possible to know the capacitive, resistive and inductive behavior of the battery impedance. Therefore, for these ac component it is possible to define a base frequency. Various points were considered as possible base frequencies, but finally the resonance frequency was chosen. This choice was due to the resistive behavior at the resonance point (1 p.u.), which clearly identifies any capacitive (smaller than 1 p.u.) or inductive behavior (larger than 1 p.u.). Moreover, it is an easily identifiable point in both the Nyquist and Bode plots.

CHAPTER 6

Nonlinear dynamic model for ultracapacitors

6.1. Introduction

This chapter presents a nonlinear dynamic model of ultracapacitors (also called supercapacitors) for simulation purposes. The model is experimentally validated under abrupt current loads.

The ultracapacitor modeled is a 3000 F 2.5 V Maxwell Boostcap. Its principal characteristics and photograph are shown in Table 6.1 and Fig. 6.1.

6.2. EIS tests experimental procedure

Ultracapacitors are receiving great attention by researchers, and due to its more recent development, the modeling techniques and model topology are still under investigation, as presented in the State-of-the-art, and there is not an unanimous equivalent circuit topology.

Capacitance	C (F)	3000
Maximum voltage	U (V)	2.7
DC series resistance	ESR dc (mΩ)	0.29
Series resistance at 1 kHz	ESR 1kHz (mΩ)	0.24
Leakage current	Ic (mA)	5.2
Shortcircuit current	Isc (A)	4800
Maximum specific energy	Emax (Wh/kg)	5.52
Maximum specific power	Pmax (W/kg)	13.8
Weight	m (kg)	0.55

Table 6.1: Maxwell Boostcap 3000F ultracapacitor characteristics

Fig. 6.1: 3000F Maxwell ultracapacitor

Moreover, ultracapacitors are high power elements, which are capable of working with very high currents (hundreds of amperes) and which need special test conditions, which require equipments able to manage very high currents and small voltages.

Normally, impedance analyzers accept low currents (e.g. 60 mA) and medium voltages (45 V). This low maximum current forces the use of other equipments along with the impedance analyzer, such as potentiostats, which are able to absorb higher dc currents. Some examples are the 1287 A Solartron potentiostat, which endures up to 2 A, the Multi-Channel Cell Test System, also by Solartron, with a 5 A limit or the HCP-1005 Kromatec potentiostat which includes an 100 A booster.

The EIS tests can be carried out either with current control (galvanostatic mode) or with voltage control (potentiostatic mode). Either option requires an ac power source able to operate in a wide range of frequencies, at very high currents and low voltages. These conditions are very difficult to find in

conventional equipments (either potentiostats or power sources).

The current range is determined by the element under study. For very large capacitance values, such as those used in this work (3000 F 2.5 V) it can be easily deduced that current variations are as large as hundreds of amperes, which result in voltage variations of only some mV, the minimum value required to have a good signal-to-noise ratio. To carry out EIS tests under these conditions, the available commercial equipments were not useful. Therefore, in this Thesis we propose an experimental setup which allows to conduct frequency and time domain tests with high currents in a flexible and low cost way.

6.2.1. EIS test conditions

The first important decision which must be taken is under which mode the EIS tests should be carried out: galvanostatic or potentiostatic. To apply a potentiostatic (voltage control) EIS test it is necessary to use an ac power source, able to absorb high currents with low voltage and be able to work in a very wide range of frequencies. It is difficult to find an equipment which fulfills all these requirements. Therefore, the EIS tests are conducted in galvanostatic mode. Even if current is the control variable, the ultracapacitor voltage must be carefully monitored, to avoid over-voltage.

In order to define the range of current amplitudes to be used during the EIS tests, a series of previous measurements were made, starting at 20 A. In all cases the resulting voltage amplitudes were measured. It was found that, due to the very large capacitance of the ultracapacitor, the EIS results for ac currents below to 150 A were useless due to the insufficient ac voltage amplitude, which caused an incorrect impedance calculation. At 150 A, the EIS tests results were clear enough to ensure a correct measure, with an ac voltage amplitude of 70 mV.

The ac signal frequency is variable between 0.1 Hz and 1 kHz. The lower frequency limit is chosen due to the fact that smaller frequencies would lengthen the test duration and cause a significant variation of the test conditions.

The maximum frequency is limited to 1 kHz because the ultracapacitor inductive behavior is already clearly identified at this frequency.

For other electrochemical systems, such as batteries or fuel cells, the ac component is normally superimposed to a dc level. However, ultracapacitors charge and discharge very quickly and it is difficult to keep the test conditions in a narrow interval. For example, the discharge time can be as short as 30 s, with a voltage variation from 2.7 rated voltage to 0 V. EIS tests, taking into account the frequency range lasts 15 minutes, so an EIS tests during a dc discharge is not possible. Moreover, the tests conditions should be kept as constant and invariable as possible, so a variation of the 100 % of the test voltage is unacceptable. Therefore, the ac current will be the only current absorbed/supplied by the ultracapacitor. This test procedure guarantees that the voltage at the beginning and end of the test will be the same due to the fact that the energy stored during half of the period of the ac current signal will be discharged during the other half. The authors who have applied EIS to ultracapacitors did it in potentiostatic mode (voltage control). Only Buller [18] carried out a galvanostatic mode EIS, but did not describe the test procedure.

In order to obtain an equivalent circuit, the dependency of the parameters of the equivalent model with current and/or voltage should be investigated. As explained in [21], [20] or [17], and unlike batteries or fuel cells, ultracapacitors parameters depend on the voltage, instead of the current, so the charge stored depends on the capacitance and voltage.

Taking into account the preceding considerations, the ultracapacitor will be tested under the following conditions:

- DC current: 0 A.
- AC current amplitude: 150 A.
- DC voltage: 1.5 V, 2 V and 2.5 V.
- Frequency: 0.1 Hz to 1 kHz.

6.2.2. EIS experimental setup proposed

To carry out the EIS tests, the equipment used is the following:

- Impedance analyzer: Solartron 1260.
- DC Electronic load: Chroma 63201 (60 V, 300 A).
- DC Power source: Sorensen 20-150E (12 V, 150 A).
- dSpace PX 10. The signals are acquired through an input/output board DS 2201, which is connected to its connector panel CP 2201. Both elements are part of a dSpace real-time control and acquisition system. The I/O DS 2201 board has 20 input channels, with 5 A/D converters which multiplex 4 channels each. There are 8 output channels with 8 parallel D/A converters. All the channels have a 12 bit resolution.
- LEM transducer: LA-205 S.
- Computer.

The EIS test is controlled by the impedance analyzer, which is the equipment which varies the frequency and monitors current and voltage to calculate the impedance. Due to the fact that it cannot directly generate a 150 A ac signal, the impedance analyzer controls other equipments which can work at high currents: the dc electronic load and power source. As explained in Figs. 6.2 and 6.3, the impedance analyzer is programmed to generate an ac voltage signal, which is monitored by the dSpace system. Through Matlab/Simulink, this signal is separated in its positive and negative semi-cycles. The positive semi-cycle is scaled to control the electronic load, which will sink the corresponding ac current. Meanwhile, the negative semi-cycle is scaled to program the dc power source, which will supply the corresponding ac current. Therefore, the coordinated and real-time control of the electronic load and power source results in a constant amplitude/variable frequency current at the ultracapacitor terminals, which follows the control signal generated by the impedance analyzer.

According to the wiring diagram depicted in Fig. 6.4, the ultracapacitor is connected in parallel to the electronic load and power source. In this way, it can absorb the current during positive semi-cycles and release it during

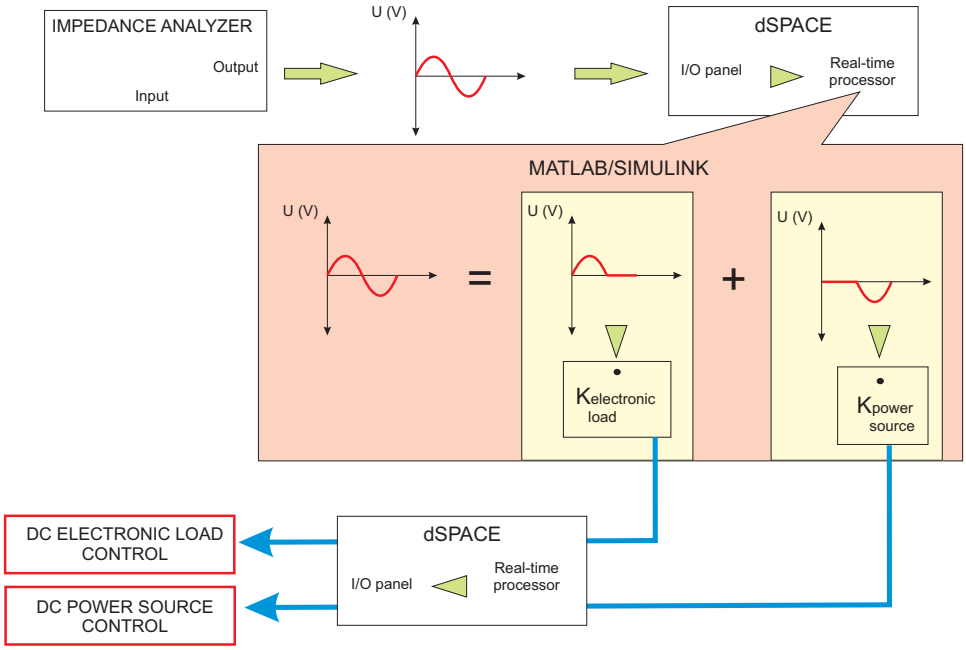

Fig. 6.2: EIS control procedure for ultracapacitors

negative semi-cycles. A current LEM transducer is connected in series with the ultracapacitor to measure the current, which is sent to the impedance analyzer. The voltage at terminals of the ultracapacitor is directly sent to the impedance analyzer, which accepts dc voltages smaller to 42 V. With the current and voltage measures the impedance analyzer is able to calculate the ultracapacitor complex impedance. The laboratory setup diagram and photograph are shown in Figs. 6.4 and 6.5.

6.2.3. EIS tests results

The graphical representation of the EIS tests are the Nyquist plots shown in Fig. 6.6. The ultracapacitor capacitive behavior is restricted to a small interval (from 0.1 Hz to 31.6 Hz). For the lower frequencies of this interval the Nyquist plot is practically a vertical line, which is the representation of a capacitance in series with a resistance, whose value (0.25 mΩ) is identified as the intersection between the curve and the abscissa axis. In literature, this part of the curve is not totally vertical due to the contact resistance between components, high electrode porosity or low proton mobility inside the electrodes [95].

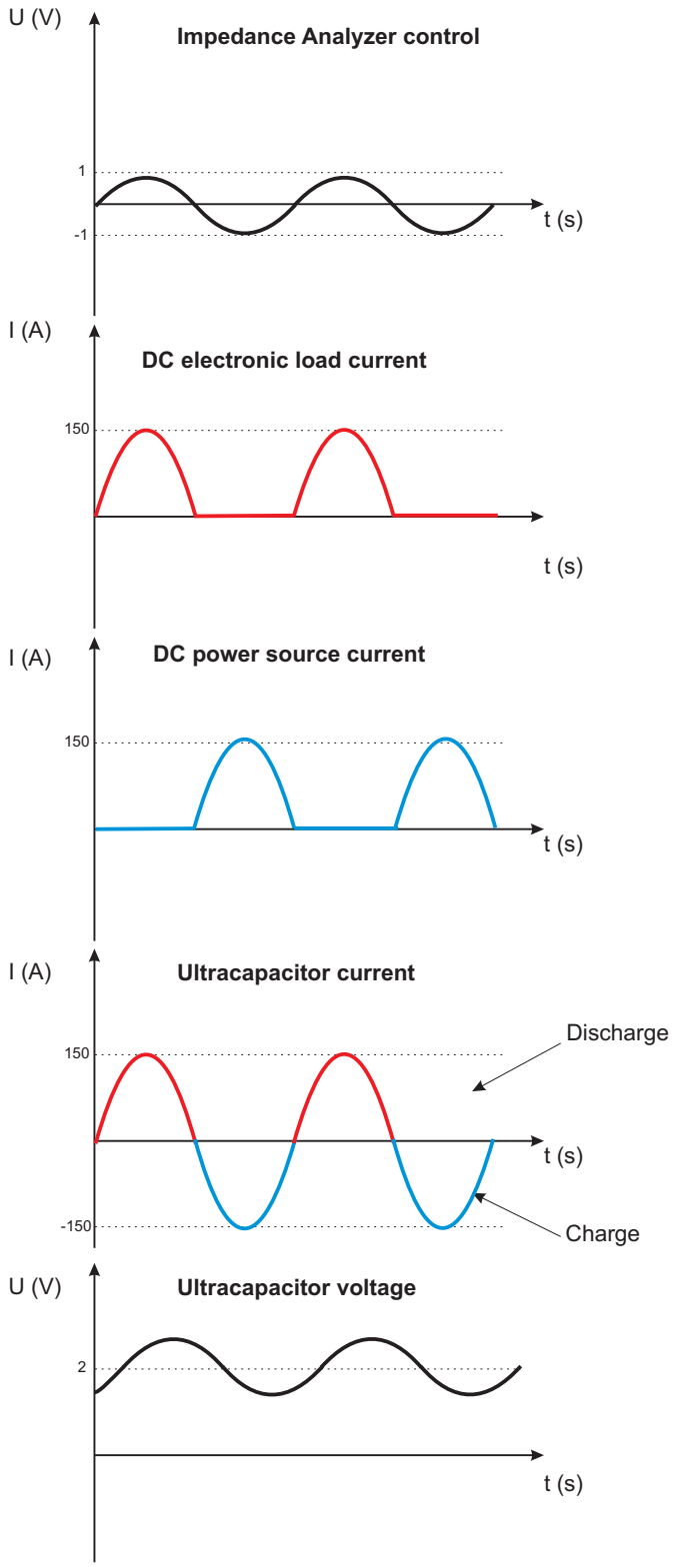

Fig. 6.3: Currents and voltage evolutions for each equipment

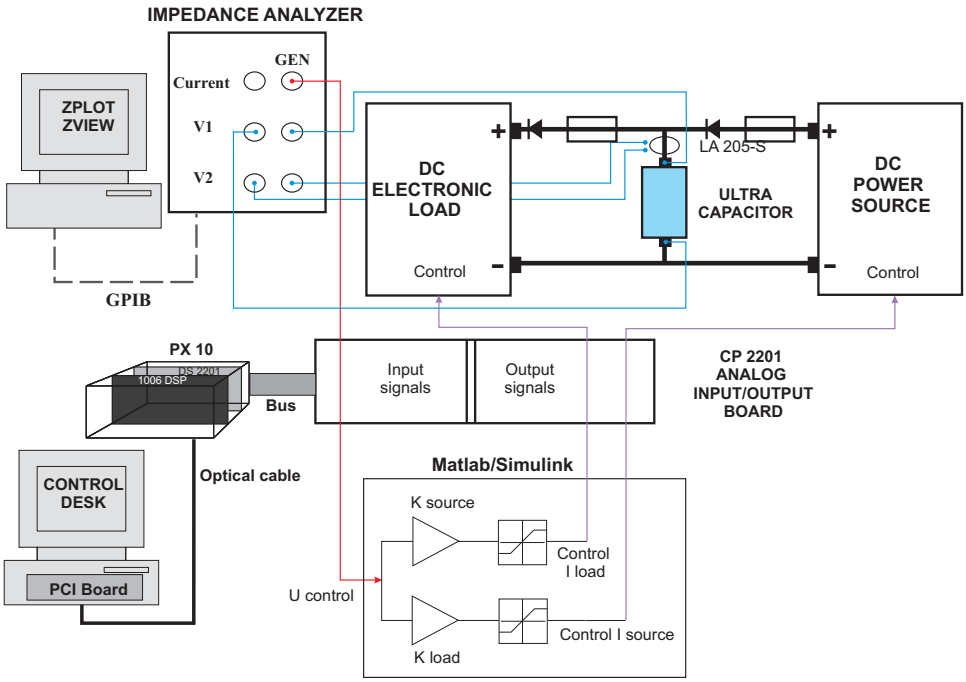

Fig. 6.4: EIS experimental setup

From 1 Hz to 31.6 Hz the complex impedance changes to a 45º slope due to diffusion phenomena at the electrode pores. In literature, some authors such as Barsoukov [46] and Brouji [76] explain that the ultracapacitor electrodes are highly porous structures, through which the charge transport resembles a transmission power electric line, due to the fact that the pore diameter is small compared to its length. This diffusion phenomena can be represented by a Warburg impedance, which is the series connection of RC networks. In this Thesis, the diffusion has been represented with two RC networks, avoiding the use of higher number of networks, which complicate the modeling and require more computational work.

From 31.6 Hz onwards, the ultracapacitor behavior is totally inductive. In literature, most authors neglect or do not comment the ultracapacitor inductive behavior and do not present this region on the Nyquist plot. Other authors such as [18], just mentions it, whilst [21] or [20] state that during inductive behavior the real part of the impedance increases due to skin effect. However, our results show that the real part of the impedance decreases before it starts increasing. At these frequencies, the current does not flow

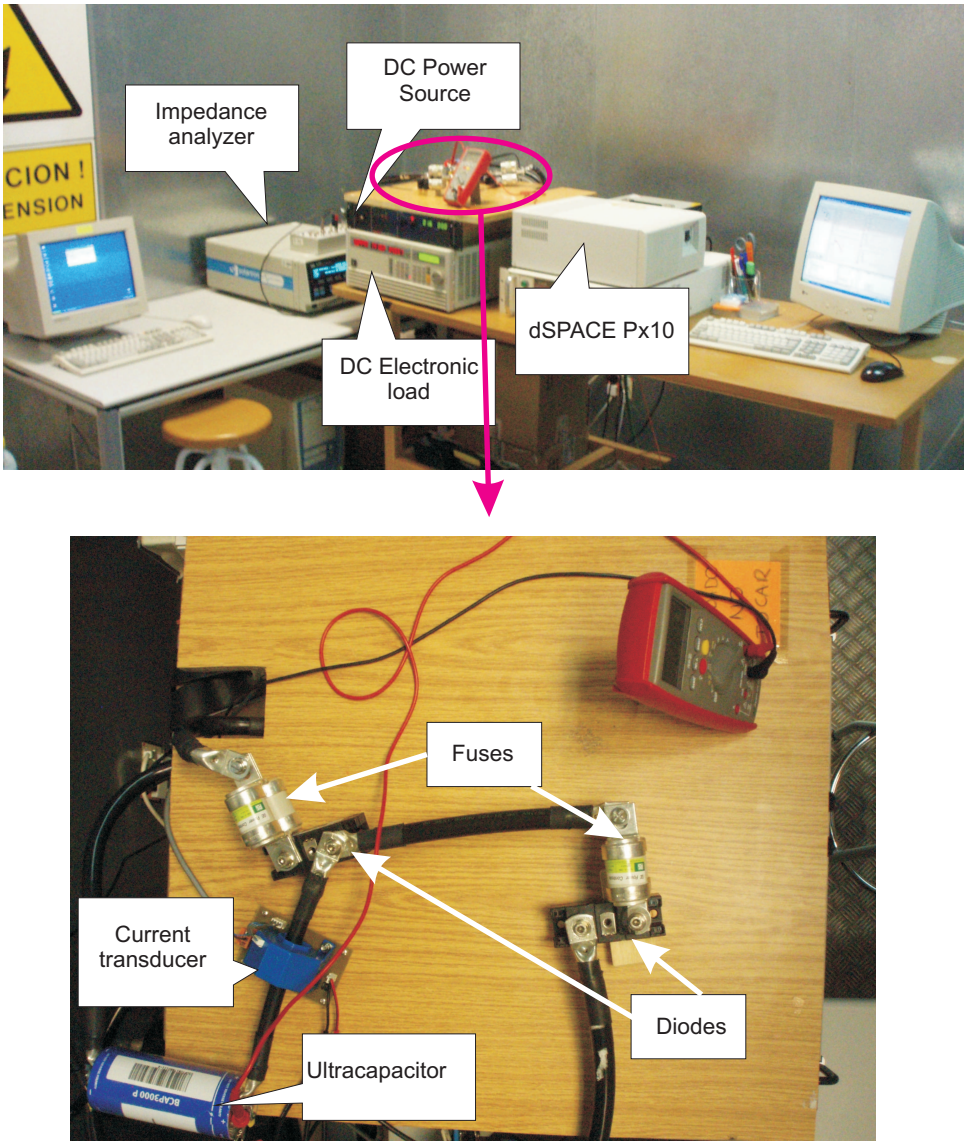

Fig. 6.5: Photograph of the ultracapacitor EIS setup

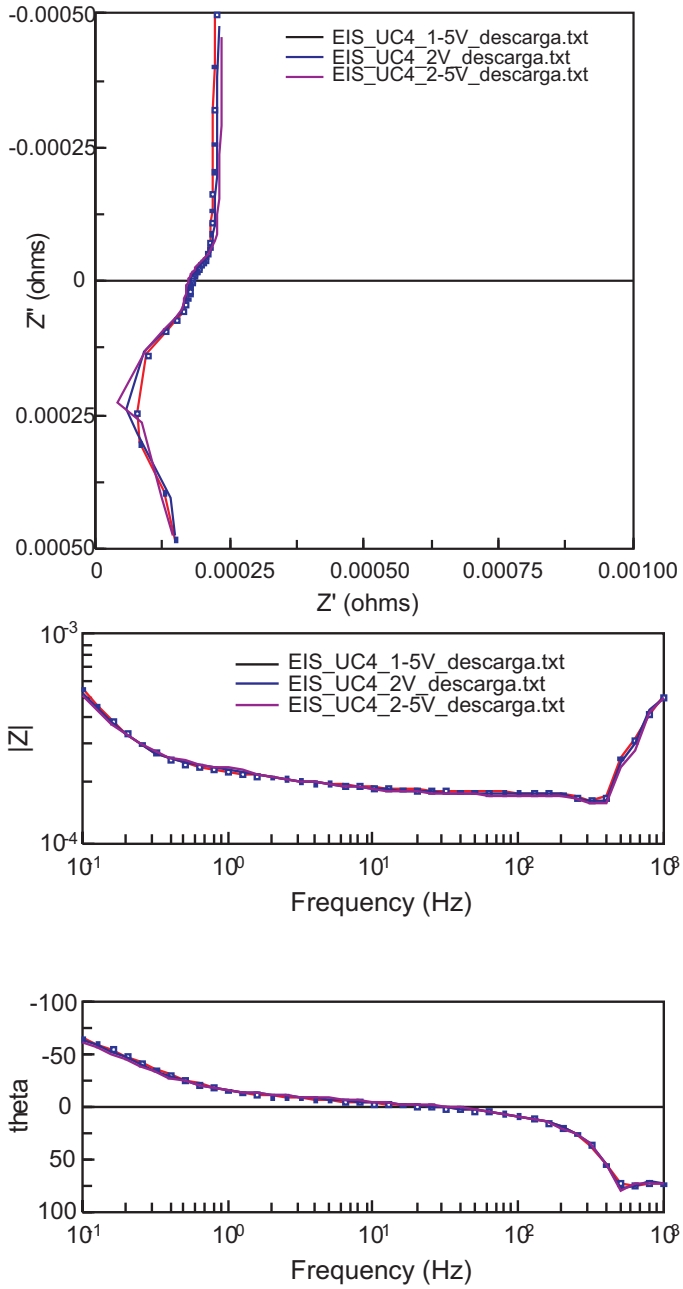

Fig. 6.6: Nyquist and Bode plots obtained for the ultracapacitor after the EIS tests

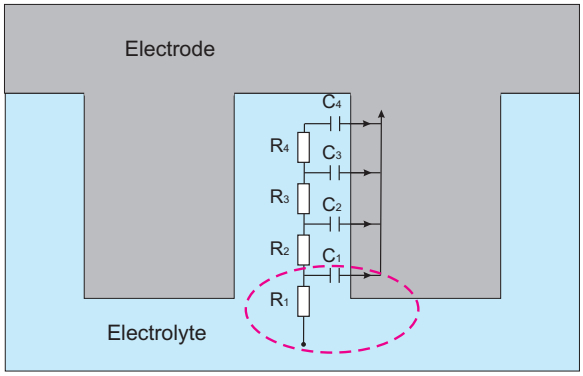

Fig. 6.7: High frequency effect on the pore effective surface. Adapted from [29]

inside the pores, but stays at the beginning of the pore, as depicted in Fig. 6.7. This implies that most of the current flows through the bulk material, whose resistance is smaller than the electrolyte resistance, causing the reduction seen in the Nyquist plot. When the frequency increases this effect is summed up with the skin effect, which causes an eventual increase of the real part of the impedance. The real part of the impedance should be always positive, therefore, possible negative values are due to small errors present when the real part of the resistance is 10^{-4} Ω.

Among the wide variety of equivalent circuits under study, the best fit of the Nyqist plot was found for the circuit structure shown in Fig. 6.8. The parameters obtained present assumable errors, and only one parameter presents an error bigger than 10 %. The values obtained from ZView were introduced in the software Statgraphics, in order to obtain the polynomial dependency of each parameter with the voltage. The model obtained explains the 100 % of the variability. The equations obtained are shown in (6.1).

$$\begin{aligned}
&\mathrm{L\ (H)} = 1.15 \cdot 10^{-7} - 7.10 \cdot 10^{-9} \cdot \mathrm{U} + 8.80 \cdot 10^{-10} \cdot \mathrm{U}^2 \\
&\mathrm{C}_1(F) = 1816 + 1260 \cdot \mathrm{U} - 244 \cdot \mathrm{U}^2 \\
&\mathrm{C}_2\ (\mathrm{F}) = 2307 - 648 \cdot \mathrm{U} + 100 \cdot \mathrm{U}^2 \\
&R_2(\Omega) = 1{,}16 \cdot 10^{-5} + 2{,}09 \cdot 10^{-5} \cdot U - 0{,}19 \cdot 10^{-5} \cdot U^2 \\
&C_3\ (\mathrm{F}) = 1.51 + 1.11 \cdot \mathrm{U} - 0.29 \cdot \mathrm{U}^2 \\
&R_3(\Omega) = 6{,}39 \cdot 10^{-4} - 1{,}47 \cdot 10^{-4} \cdot U + 0{,}36 \cdot 10^{-4} \cdot U^2
\end{aligned} \tag{6.1}$$

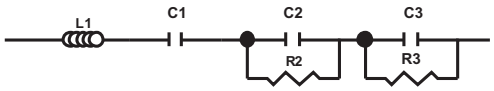

Element	Freedom	Value	Error	Error %
L1	Free(+)	1,0728E-7	1,5885E-9	1,4807
C1	Free(+)	3157	75,692	2,3976
C2	Free(+)	1560	319,51	20,481
R2	Free(+)	3,8784E-5	3,9544E-6	10,196
C3	Free(+)	2,532	0,099294	3,9216
R3	Free(+)	0,00016681	2,193E-6	1,3147

Chi-Squared:	0,01661
Weighted Sum of Squares:	1,2624
Data File:	D:\SANDRA\RESULTADOS EIS UC\Definitivos\EIS U
Circuit Model File:	D:\SANDRA\RESULTADOS EIS UC\Circuito Equival
Mode:	Run Fitting / Freq. Range (0,1 - 1000)
Maximum Iterations:	800
Optimization Iterations:	0
Type of Fitting:	Complex
Type of Weighting:	Calc-Modulus

Fig. 6.8: Equivalent circuit fitted with ZView

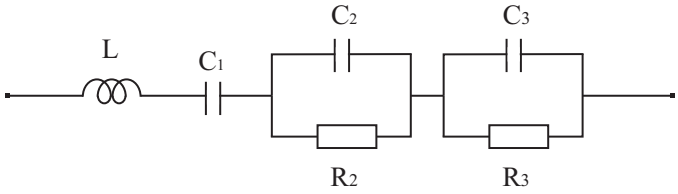

Fig. 6.9: Ultracapacitor equivalent circuit

6.2.4. Ultracapacitor impedance model and validation

With the previous equations, the model obtained is shown in Fig. 6.9. It can be observed that, unlike batteries or fuel cells, the ultracapacitor model is a purely passive model, with no voltage or current sources. All the elements involved present electrical equations, which are easily programmed in Matlab/Simulink. The voltage at the ultracapacitors terminal programmed corresponds to 6.2.

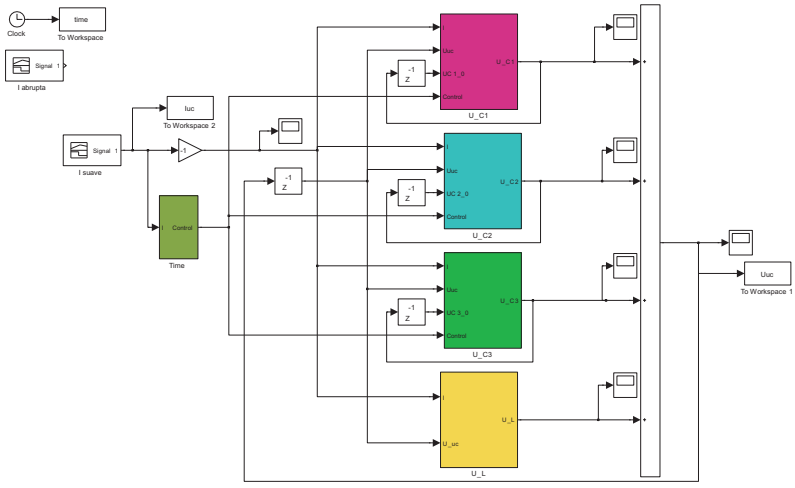

Fig. 6.10: Ultracapacitor Matlab/Simulink model

$$
\begin{aligned}
U_{uc} &= U_L + U_{C_1} + U_{C_2} + U_{C_3} \\
U_L &= L \cdot \frac{dI}{dt} \\
U_{C_1} &= \int \frac{1}{C_1} \cdot I \cdot dt \\
U_{C_2} &= \int \frac{1}{C_2} \cdot \left(I - \frac{U_{C_2}}{R_2} \right) \cdot dt \\
U_{C_3} &= \int \frac{1}{C_3} \cdot \left(I - \frac{U_{C_3}}{R_3} \right) \cdot dt
\end{aligned}
\tag{6.2}
$$

The ultracapacitor model has two inputs and one output. The inputs are the current demanded and the voltage at its terminals. This ultracapacitor models needs an initial voltage value to begin the simulation. The model output is the voltage at the terminals of the ultracapacitor. The Matlab/Simulink model is shown in Fig. 6.10

To obtain an experimental validation of the model, an abrupt load current profile, depicted in Fig. 6.11, was programmed and the voltage at terminals monitored. The experimental and modeled voltages are compared in Fig. 6.12. It can be observed that the ultracapacitor time constant is very small and causes the dynamic evolution to present a linear evolution under abrupt

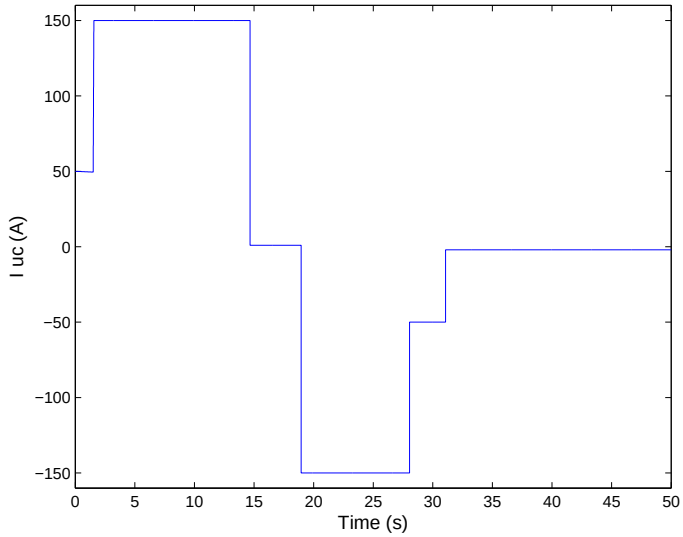

Fig. 6.11: Abrupt ultracapacitor current load

current profiles. The model follows quite precisely the experimental voltage.

6.3. Conclusions

Ultracapacitors are a relatively new technology, and therefore, its test procedure, equivalent circuit and characteristic curve are not universally defined. Moreover, ultracapacitors are high power elements which need special test considerations. These considerations are rarely mentioned in literature, where authors avoid disclosing its test setup and procedure, and most of them do not make any attempt to validate the model proposed.

Ultracapacitors tested up to now are usually smaller than the 3000 F ultracapacitor tested in this Thesis. Therefore, the equipments used by other authors, frequently not mentioned, are not applicable due to its small current limit. In this Thesis we propose an EIS test procedure which allows to carry out these test during the high currents needed to obtain a correct impedance calculation. The setup proposed uses conventional laboratory equipments, such as dc electronic load and dc power source, which can be synchronously controlled by an impedance analyzer through a real-time acquisition and control system.

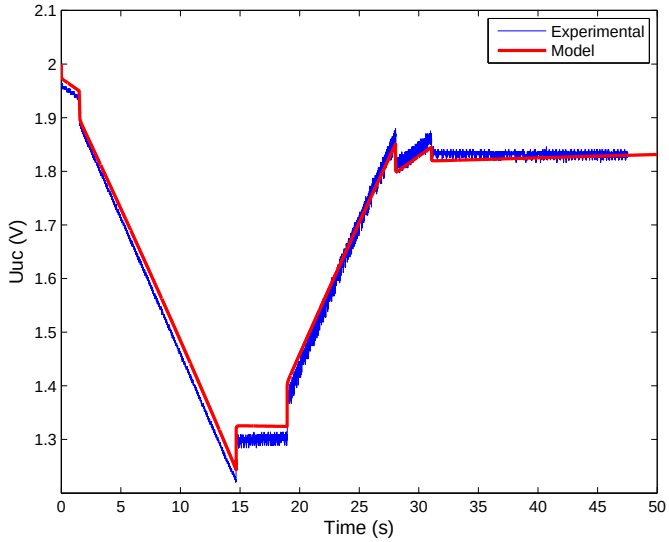

Fig. 6.12: Experimental and modeled voltage

After testing all the equivalent circuits presented by other authors and new ones, the one presented is found to be a good fit for the Nyquist plot and the experimental validation confirms the model adequacy. The model proposed is similar to the one presented by Buller (can be seen in the state-of-the-art chapter), however, Buller included a large number of RC networks, when just the two networks presented render good results. Moreover, the ultracapacitor behavior during high frequencies, not studied or incorrectly explained by other authors, was studied, revealing a reduction of the real part of the impedance due to the pore small effective surface.

CHAPTER 7

HIL simulation for hybrid energy sources

7.1. Introduction

In automotive applications, due to environmental and energetic concerns, fuel cell hybrid electric vehicles (FCHEVs) have turned out to be an interesting alternative to traditional vehicles based on internal combustion engines (ICE). One of the consequences of the development of hybrid electric vehicles (HEVs) is the variety of topologies which the power train can adopt. An overview of these architectures can be consulted in [96]. However, even if FCHEVs present attractive properties, they must still reach competitive achievements in terms of range, cost, fuel storage, etc. To achieve these objectives extensive work must be done in the development and testing of the electrochemical systems (fuel cells, batteries, and ultra capacitors), electric drives, power electronics, and control. The design of some of these subsystems could benefit from adequate tools to lower development costs. This issue is particularly relevant, e.g. during the design of power electronics, when most of the important costs and complexity are associated to the direct connection to the fuel cell system. These design tools can be classified in three groups: pure numerical simulation, pure hardware platforms or hardware-in-the-loop (HIL) simulation systems.

Pure simulation is the most cost effective approach; however the models and simulations carried out are a mere approximation of the real system, and the accuracy of the conclusions strongly rely on the accuracy and validity of the numerical models used. On the other hand, with pure hardware a realistic performance of the devices involved can be obtained [97]. However, this approach presents some drawbacks which cannot be ignored, such as high costs of the elements under test, the infrastructure and security requirements (especially for a hydrogen storage and supply system) and the complexity associated to the performance of the test when a high number of elements are involved.

An intermediate solution between the two previous approaches is the hardware-in-the-loop (HIL) simulation, in which one or several devices of the system are used instead of their simulated models. Depending on the nature of the variables which interact between the simulated and hardware devices, HIL simulation can be classified as signal level, power level or mechanical level, as described by Bouscayrol in [79]. The power or mechanical levels are especially suitable for the simulation of hybrid energy systems in vehicles as the devices involved are power sources, such as fuel cells and batteries, power converters and electric machines.

The HIL test benches presented by other authors [27], [81] include the vehicle simulator as an electric machine working against a brake. But the inclusion of the electric machine and brake results in a high cost and complex HIL system, which is limited to vehicular applications. In addition, these HIL systems could not be used for other power levels as it is designed for a specific case and power rating [98]. If instead of carrying out the simulation in absolute values it is carried out in per-unit values the HIL test bench will be independent of the application power rating.

Hence, obtained the electric models for batteries, fuel cells and ultracapacitors, it is possible to carry out a per-unit HIL simulation of a hybrid system which includes two or more of these electrochemical sources. The HIL test bench developed is able to reproduce a wide range of power applications. Moreover, the vehicle simulator does not consist of any electric machine dri-

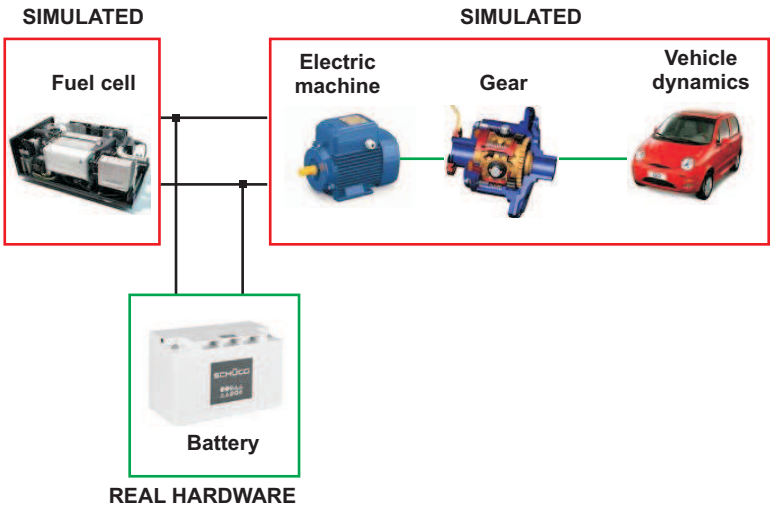

Fig. 7.1: Case studied

ving a break, but of a combined control of a dc electronic load and source, which allows to simulate both the vehicle power requirement and regenerative braking. This simulator does not present the complexity of setup which the electric machine and drive present and is able to follow the vehicle power demand.

7.2. HIL description

The HIL simulation is carried out for a particular case of a vehicular application, as shown in Fig. 7.1.

A vehicle power load profile is formed by a relatively low base power (cruising) with very high abrupt power peak loads (acceleration and overtaking). In vehicles with internal combustion engines, the average power generated by the engine is considerably lower than its maximum power.

If the internal combustion engine is substituted by a hybrid system fuel cell/energy storage, the primary system (fuel cell) can have a lower installed power due to the presence of the energy storage. The fuel cell can supply the power needed for the base power load, however it cannot respond to highly dynamic changes in the instantaneous power load. Fast energy storage devices, such as batteries or ultracapacitors can supply the power requested by

the peak loads, but they suffer from serious capacity shortage for the supply of the long term energy [99]. As neither the fuel cell nor the fast energy storage devices can supply individually the whole power load, hybridization between both devices is needed. This is, of course, one of the possible alternatives, but it represents the most essential aspects of the problem. The sealed lead-acid batteries used in Chapter 5 [85], especially designed for traction purposes are used, due to their maturity and robustness, as well as to their ability to supply very high current peaks; however, they may be replaced by ultracapacitors or by other battery technologies [38], such as Ni-Mh or Li-ion, the latter being likely the most frequent choice in the next future.

Once the elements of the hybrid system have been identified two relevant decisions must be made when designing a HIL simulation. The first one is related to which components should be simulated or implemented by hardware. This choice is based on the flexibility, cost and complexity which each system adds to the whole HIL simulation. For example, a fuel cell is a complex and high cost system which needs special environments and installations due to the presence of hydrogen. Therefore, this system is a good candidate for being included as simulated in the HIL system. On the other hand, energy storage systems, such as batteries (or supercapacitors) are modular systems which do not require a specific installation and present a lower cost, simple operation and flexibility. Therefore, they are suitable for being part of the hardware systems in the HIL simulation, especially for electrical or electronic research laboratories, which are not specifically designed to operate with hydrogen-fed systems.

Finally, the load which is fed by the hybrid energy system varies significantly depending on the application (stationary or vehicular). The inclusion of an electric machine and brake limits the application of the HIL platform to vehicular cases and it is a complex and expensive system. Hence, in this Thesis the load is simulated as the parallel connection of a controlled dc electronic load and dc power source. With this load simulation, both stationary and vehicular applications could be simulated, and even regenerative braking can be tested.

The second decision is an important issue related to the sizing of the whole

HIL simulation. The HIL test bench developed should be able to reproduce a wide range of power applications. Therefore, the installed power of the HIL test bench should be high enough to ensure a realistic simulation, but not so high so as to increase significantly the cost and complexity of the setup. In order to satisfy these requirements, in this Thesis we propose a per-unit HIL simulation which is detailed in the following section.

7.2.1. Per-unit HIL simulation

To cope with systems where different currents, powers and voltage levels are involved, power engineers make an extensive use of the per unit system (p.u.). Any system attributes, as dynamic models, control, setup, results and conclusions expressed in p.u. values are also valid for absolute values, as the adimensional magnitudes are linked to the same set of equations (whether static, dynamic, linear or nonlinear) that describe the model behavior in absolute values. Moreover, if the variables are expressed as p.u., the sizing of the HIL test bench can be independent of the real application sizing, and be therefore useful for any power rating.

For the simulated case studied the maximum power rating is 25 kW. As the setup of a 25 kW test bench is more costly and complicated, a smaller test bench with a reducing scale of 10:1 is proposed, which implies a maximum power of 2.5 kW on the HIL simulation. The simulation of this reduced scale system is carried out with the p.u. system, in order to easily extrapolate the results and conclusions obtained to the real power system. The p.u. system will depend on the base values selected. The base values can be arbitrarily decided by the user, however, for the purpose for this work, we have chosen a base power of 250 W, as it is the base power of the power cycle, which will be supplied by the fuel cell. It is proposed to select the battery voltage as the base voltage: 12 V. Known these two values, the base current can be calculated. The following base values have been chosen:
Base power (P_b): 250W.
Base voltage (U_b): 12 V (rated battery voltage).
Base current (I_b): 20.83 A.
Base capacity (C_b): 50 A·h (rated battery capacity).

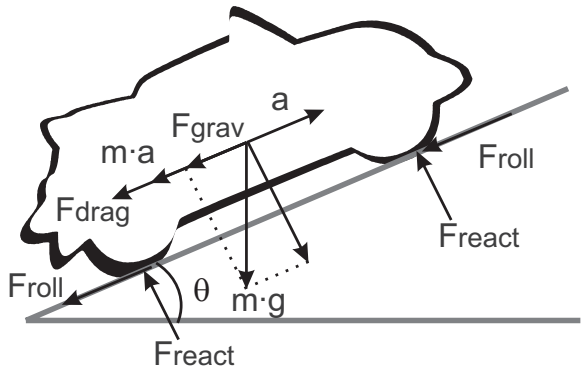

Fig. 7.2: Forces present in a vehicle while driving uphill

7.3. HIL implementation

In this section, we present the HIL implementation for the vehicle model and vehicle and fuel cell simulator. The fuel cell simulator will be based on the dynamic nonlinear model obtained during Chapter 4.

7.3.1. Vehicle model

In this work we use a simplified model for the mechanical part of the vehicle, including vehicle forces, gear box and electric machine. The vehicle power requirements have been calculated through the resistance forces [100] which must be overcome by the vehicle power sources to move the vehicle at the desired speed. These resistance forces are normally calculated while the vehicle is being driven uphill, as shown in Fig. 7.2.

$$\begin{aligned} F_{grav} &= m \cdot g \cdot sen\theta \\ F_a &= m \cdot a \\ F_{drag} &= \frac{1}{2} \cdot \rho_{air} \cdot A \cdot C_d \cdot v^2 \\ F_{roll} &= m \cdot g \cdot \cos\theta \cdot \left(f_0 + f_v \cdot v^2\right) \end{aligned} \tag{7.1}$$

Equation (7.1) shows the resistance forces F_{grav}, F_a, F_{drag}, and F_{roll}. F_{grav} represents the gravitational force, which depends on the vehicle mass m, the gravitational acceleration g and the slope angle θ. F_a represents the acceleration resistance, which depends on the mass m and the vehicle acceleration a. The drag resistance F_{drag} depends on the air density air, the vehicle frontal

Parameter	Symbol	Quantity
Vehicle mass	m (kg)	1000
Frontal surface	$A\ (m^2)$	1.8
Drag coefficient	C_d	0.19
Copper losses	k_c	0.3
Iron losses	k_i	0.01
Winding losses	k_w	0.000005
Electronic losses	EL	600

Table 7.1: Parameters for the simulated vehicle

surface A, the drag coefficient C_d and the vehicle speed v. Finally, the rolling resistance F_{roll} depends on the weight $m{\cdot}g$, the slope angle θ , the static friction coefficient f_0 and the dynamic friction coefficient f_v. The parameters for the simulated case are presented in Table 7.1.

Electric powertrains admit different electric machine technologies, such as induction machine, permanent magnets, switched reluctance, etc. as described by [101]. As this work is focused on the implementation of a flexible test bench which allows both stationary and vehicular applications, the electric machine is taken into account as a system which introduces an efficiency factor (7.2) between the power requested by the vehicle and the power supplied by the fuel cell/battery system, centering the attention on the energy sources dynamic behavior and time window. In (7.2), T is the torque needed to move the vehicle at the requested speed; ω is the electric machine rotational speed, which depends on the gear ratio, k_c, k_i and k_w represent the copper, iron and windage coefficient losses. The values for these coefficients are detailed in Table 7.1.

$$\eta_{mot} = \frac{T \cdot \omega}{T \cdot \omega + T^2 \cdot k_c + \omega \cdot k_i + \omega^3 \cdot k_\omega + EL} \tag{7.2}$$

7.3.2. Vehicle simulator

The vehicle simulator is implemented by means of a programmable dc electronic load and a dc power source, operating under combined control mode, similar to the one used during the ultracapacitor testing. The dc electronic load (Chroma 63201) acts as a sink for the power generated by the energy sources, whilst the dc power source (Sorensen SGI) can generate rege-

nerative braking by injecting power to the dc bus to which the energy sources are connected. It is important to take the regenerative braking into account as it has an important impact on the battery state of charge SoC and the vehicle range due to the recharging cycles.

One of the advantages of this vehicle simulator, compared to the one used by other authors, is that it presents a lower cost and complexity than an electric machine and brake system. Moreover, it adds flexibility to the whole test bench, as any load power cycle (stationary or vehicular) can be simulated without altering the load simulator. The layout of the vehicle emulator, shown in Fig. 7.3, is composed by a software and hardware simulation of the vehicle. The software part includes the driving cycle, vehicle resistive and tractive forces, gear ratio and electric machine efficiency and torque. Once the speed driving cycle is transformed to a power or current profile, this profile is used to control externally both the electronic load and power source. The control of both the electronic load and power source is done analogically; through a 0-10 V signal which programs the equipment from 0-100 % of its rated value. The power generated by the simulated fuel cell and the physical battery is absorbed by the electronic load according to the programmed power cycle. The dc power source of the load simulator will only inject power in the dc bus during regenerative braking peaks. This power is used to recharge the battery. The power source is protected with a power diode which prevents current from sinking to the power source. The communication between the software and hardware part of the load simulator is done in real-time, as explained later.

7.3.3. Fuel cell simulator

The fuel cell simulator is based on the dynamic nonlinear model obtained previously, which is fed to a dc power source which emulates its behavior. The fuel cell system simulator is formed by a programmable dc power source (Sorensen DCS20-150E) which is programmed with a 0-10 V signal for the output voltage and with a 0-10 V signal for the output current limit, allowing the voltage and current control of the fuel cell, just as it happens when the fuel cell is connected to a dc-dc power converter. These values are establis-

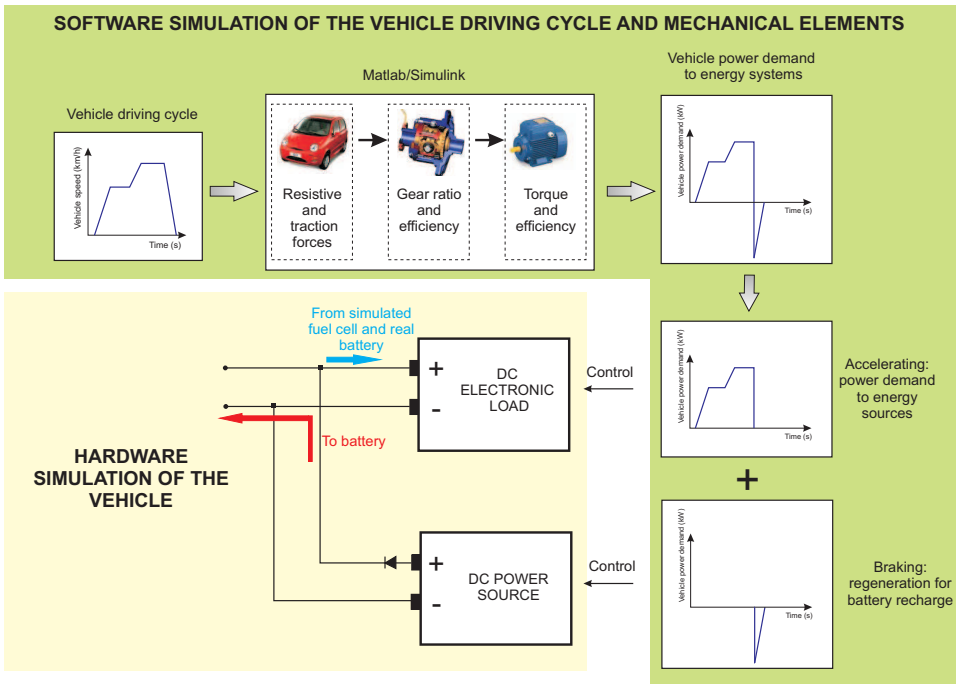

Fig. 7.3: Vehicle simulator proposed

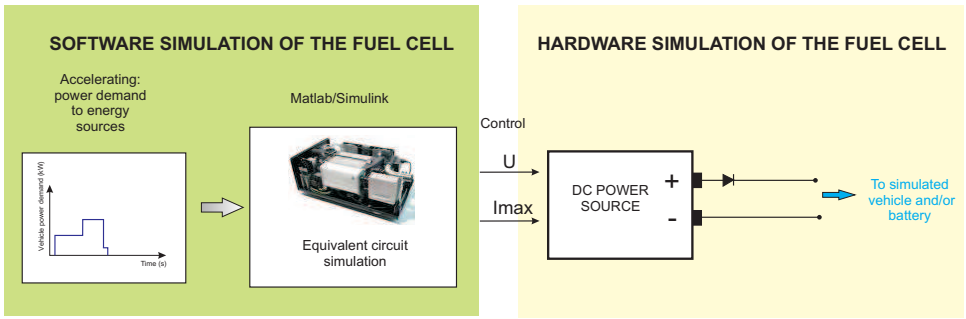

Fig. 7.4: Fuel cell simulator proposed

hed by the control system, depending on the vehicle driving cycle and the battery state of charge, as explained later. The model presented in previous chapters is implemented in Matlab/Simulink and fed to the dc power source, as shown in Fig. 7.4. Just as in a physical fuel cell system, the power source which simulates the fuel cell operation is protected against sinking currents by a power diode. As in the case of the vehicle simulator, the interaction between the software and hardware simulation of the fuel cell system is done in real-time.

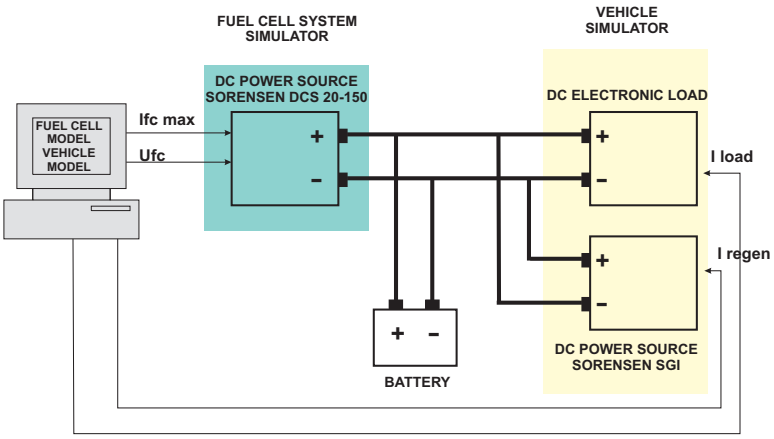

Fig. 7.5: HIL simulation power wiring

7.3.4. HIL power connections

The energy storage subsystem of this hybrid energy application consists of a Maxxima Exide-Tudor sealed lead-acid battery of 12 V, 50 Ah (20 h) connected in parallel to the dc bus. The power connections for the whole test bench are depicted in Fig. 7.5. As it can be observed, multiple power sources are connected in parallel. However, this presents no inconvenience in terms of voltage or current establishment. This is due to two facts. The first one is that the vehicle simulator (dc electronic load + power source) is current controlled, and therefore adapts to the voltage imposed by the hybrid energy system and hence, no ideal voltage sources are directly connected in parallel. The power source which simulates the fuel cell acts as a voltage or current source, depending on the load power requirements. Besides, both the simulated fuel cell and the battery show a non-negligible variable series impedances.

When more than two equipments must be connected in parallel, it is difficult and messy to do it directly. Therefore, for this Thesis we have designed a particular two floor chassis which allows the parallel connection of up to 5 equipments in a safe, direct and neat way. Fig. 7.6 presents the external photograph, which includes safe power connectors (they can endure up to 400 A and 250 V).

An internal power busbar is connected to the Bus, ESS1 (energy storage system 1), ESS2 (energy storage system 2), Power source and Load connectors, so that any equipment connect to these terminals is connected in parallel without having to do it each time the system topology changes.

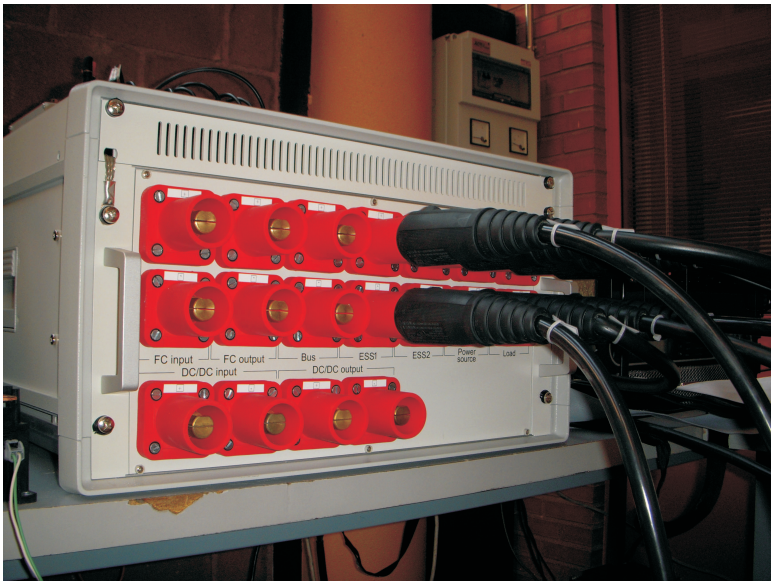

Fig. 7.6: Chassis developed for power connections

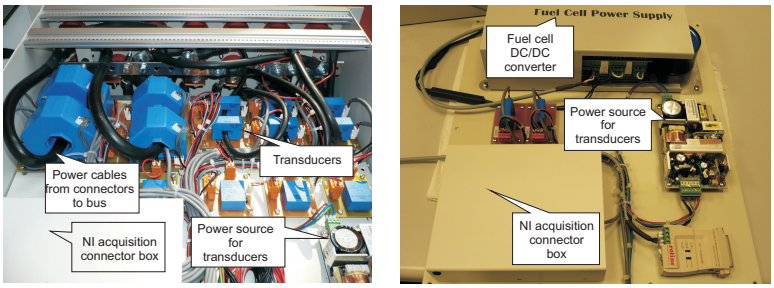

Fig. 7.7: Chassis upper (left) and lower (right) floor

The fuel cell and DC/DC connectors are not in parallel with the rest. This increases the chassis flexibility, because then the fuel cell can be connected to the parallel power busbar either directly or through a DC/DC converter. To connect the fuel cell or the DC/DC converter to the busbar a wildcard connector has been included: the "Bus" connector. If no fuel cell or DC/DC converter is connected, then it is free to connect a third energy storage system if needed.

As it can be seen in Fig. 7.7 all the transducers are duplicated, in order to acquire with two different acquisition systems (National Instruments and dSpace) and to ensure a reading if one of the transducers fail. Both power and control wiring are included in the chassis, therefore, for safety purposes,

a ground connection was included.

7.4. HIL acquisition and control system

7.4.1. HIL acquisition system

An acquisition system is necessary to register the evolution of the different devices involved. LEM transducers are used to measure the dc bus voltage, as well as the simulated fuel cell, dc electronic load and dc power source which emulate the vehicle and battery current. The signals are acquired through an input/output board DS 2201, which is connected to its connector panel CP 2201. Both elements are part of the dSpace real-time control and acquisition system.

7.4.2. HIL control system

Hybrid systems accept a variety of control schemes, as for example [102], [103], [104] or [105]. The objective of the control system presented is to test the HIL test bench, in order to demonstrate its usefulness and applicability.

Due to the fact that the energy system is hybrid between a simulated fuel cell and a physical battery, the control applied in this case will analyze and quantify the power share between the simulated fuel cell system and the real battery. Because the fuel cell system is not able to supply high energy peaks, the fuel cell system will be assigned the role of supplying the average power. With this strategy, the simulated fuel cell can be kept at or near the most efficient operation point. The power peaks will be supplied by the battery, which has a much faster response. The result is the simulated fuel cell feeding the average load power and recharging the battery during low current consumption periods, and the battery supplying power peaks and accepting energy during regenerative braking. Thence, it is possible to have a total control of the hybrid system by what could be called the "energy management mode" (EMM) of the system, which will depend on the type of control selected: fuel cell optimization, battery SoC, etc. The battery SoC at any instant must be calculated (7.3) and controlled.

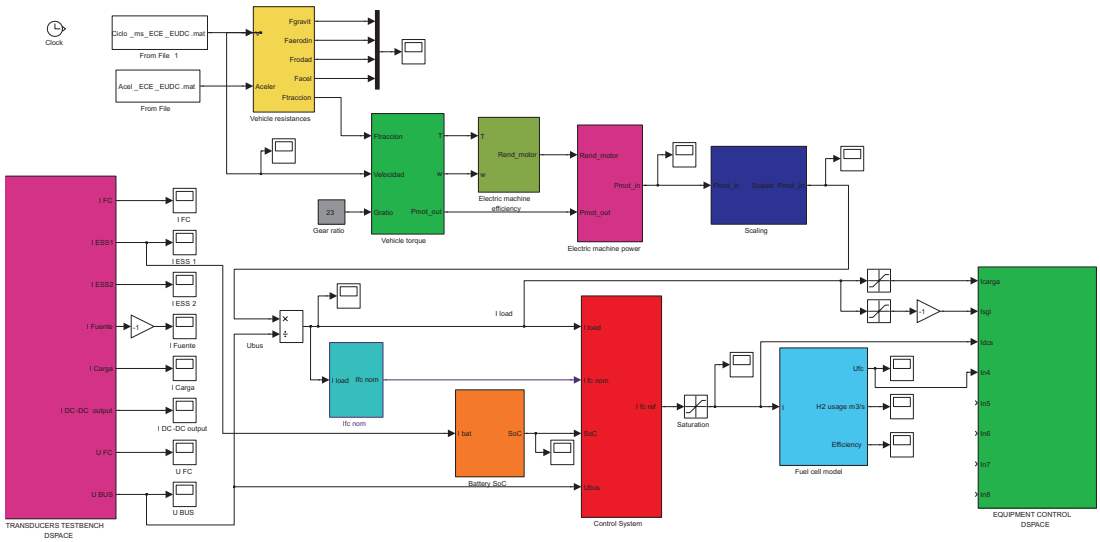

Fig. 7.8: HIL Matlab/Simulink programme

$$SoC_t\,(\,\%) = SoC_{t-1}\,(\,\%) \pm \frac{\eta}{C_n} \cdot \int_{t-1}^{t} I(t) \cdot dt \cdot 100 \tag{7.3}$$

The SoC calculation takes into account the charging efficiency and the battery rated capacity C_n. As reflected in the second addend of (7.3), the charged capacity depends on the charge efficiency. The sign of the second addend depends on the battery operation mode: it is positive for charge and negative for discharge.

The complete Matlab/Simulink programme is shown in Fig. 7.8. The control system is implemented in a real-time platform as a general-purpose operating system does not have a consistent, repeatable, and known timing performance. The real-time platform is based on a dSpace Modular Hardware formed by an expansion box PX10, with a digital signal processor DSP DS 1006. The DSP communicates with the host computer through an optical cable and a PCI board. The dSpace and the host computer carry out task sharing, as the dSpace hardware performs the real-time calculation and the host computer provides the user interface and the experiment environment. The DSP DS 1006 is built around an AMD Opteron processor which runs at 3 GHz and has 256 MB as local memory for the execution of real-time

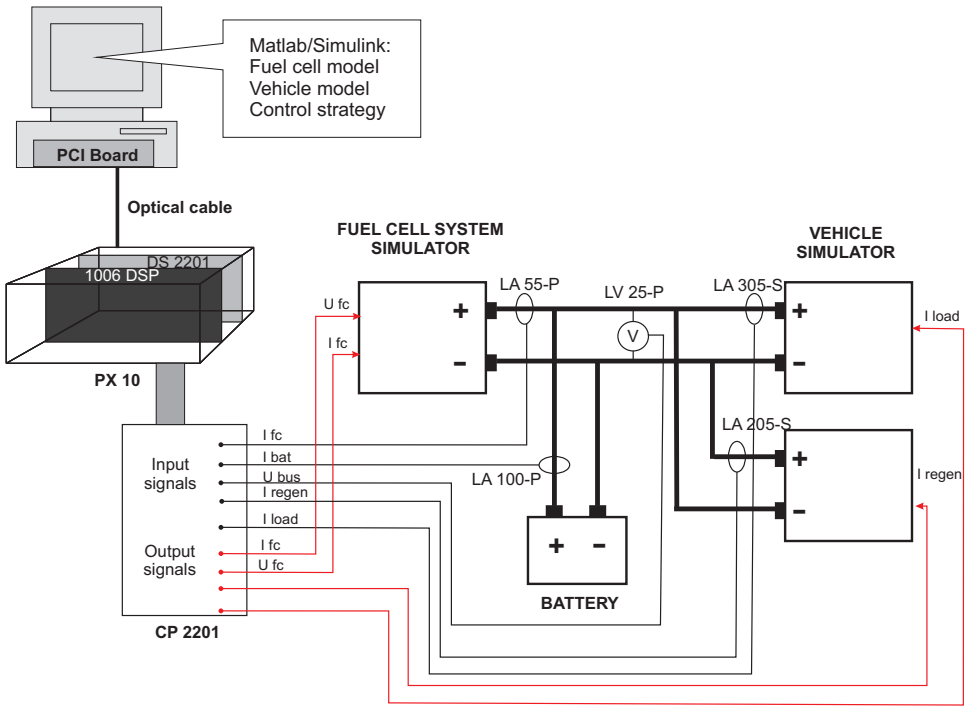

Fig. 7.9: HIL simulation

models, 128 MB of global memory to exchange data with the host computer and 2 MB of flash memory. The I/O boards can be programmed using Matlab/Simulink and Real Time Interface (RTI).

The program developed is executed with a fixed step 1 ms and a fourth order Runge Kutta algorithm. The 1 ms time step selected is smaller than the vehicle (seconds), fuel cell (20 ms for the model used) and battery (10 ms for the battery used) time constant, and can therefore capture the dynamic operation of any system involved. Smaller time steps could lead to heavy experimental data files (e.g. over 1 million samples were recorded for each signal captured during the test carried out.) Figs. 7.9 and 7.10 present the layout and photograph of the whole HIL simulation.

7.4.2.1. Energy management modes (EMM)

In a hybrid system, a wide range of control schemes could be implemented, depending on the objective: maximum range, minimum fuel consumption, minimum SoC variation, etc. This wide range of control schemes is due to the hybrid nature of the system, with one source able of supplying

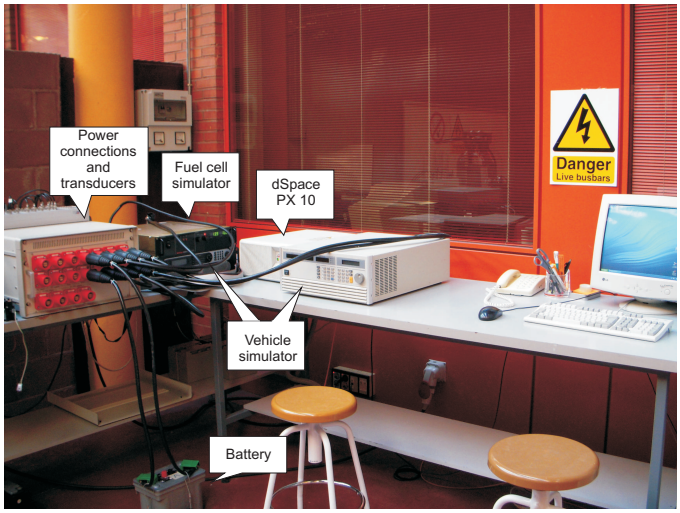

Fig. 7.10: HIL photograph

long term load (fuel cell) and another source capable of supplying shorter term loads (energy storage system). With these different time windows, control schemes may benefit one system but penalize the other. Therefore, some type of compromise should be reached.

In this Thesis, two different and representative EMM of how a control scheme affects each system will be applied: the first one will reduce the hydrogen consumption and efficiently recharge the battery, whilst the second one will keep the battery SoC within an established interval. Of course, other control schemes could be tested.

For EMM 1, the fuel cell output will vary between two different levels (one low level to reduce the fuel consumption and the maximum power point when the load current surpasses 100 A) while supplying the load and recharging the battery with the profile shown in Fig. 7.11. Fig. 7.11 presents this charge profile, in which the values are selected based on previous experiences with the battery.

If the load current is smaller than the rated fuel cell current the battery starts a recharge cycle. The charge current depends on the battery SoC, as for increasing $SoCs$ the battery voltage increases. The recommended charging voltage limit for this battery, as specified by the manufacturer, is 14.4 V. Due to the fact that the charge efficiency decreases dramatically for high

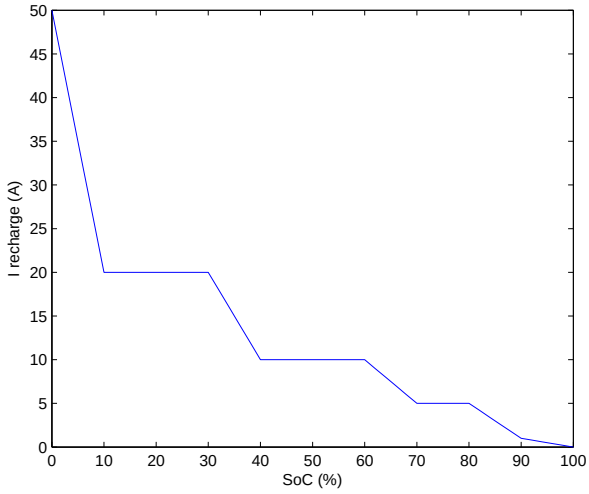

Fig. 7.11: Fuel cell recharge current to the battery

SoCs, the *SoC* is kept between 40 %-60 %, as in this interval there is no risk of overcharge or battery depletion, which would contribute to shorten the battery life due to gasification or sulphatation phenomena. The 60 % upper limit for the *SoC* also assures that the battery will be always ready to accept power peaks during regenerative breaking.

For EMM 2, the fuel cell will be kept at its maximum power point, both during the vehicle power following and during the battery recharge. Hence, the battery will have to deal with the peak transients. If during the driving cycle the battery voltage surpasses the manufacturer recommendation (max. 14.4 V or 1.2 p.u.) the control system will reduce the fuel cell reference (37.78 A or 2 p.u.) in order to reduce the charge regime or force the battery into a discharge cycle, which in both cases will lower the battery voltage.

In general, for both EMMs, depending on the drive cycle, the battery could exceed the maximum 100 % *SoC* if a low load or high regenerative breaking takes place. Hence, if the maximum *SoC* is exceeded the fuel cell reference will be reduced in order to force the battery into a discharge cycle. Also, the fuel cell will be in continuous operation, even during short stops, in order to recharge the battery. However, if the stop time exceeds 5 minutes the control system will stop the fuel cell. Moreover, if during the stop time the battery *SoC* exceeds the 80 %, the fuel cell will also stop.

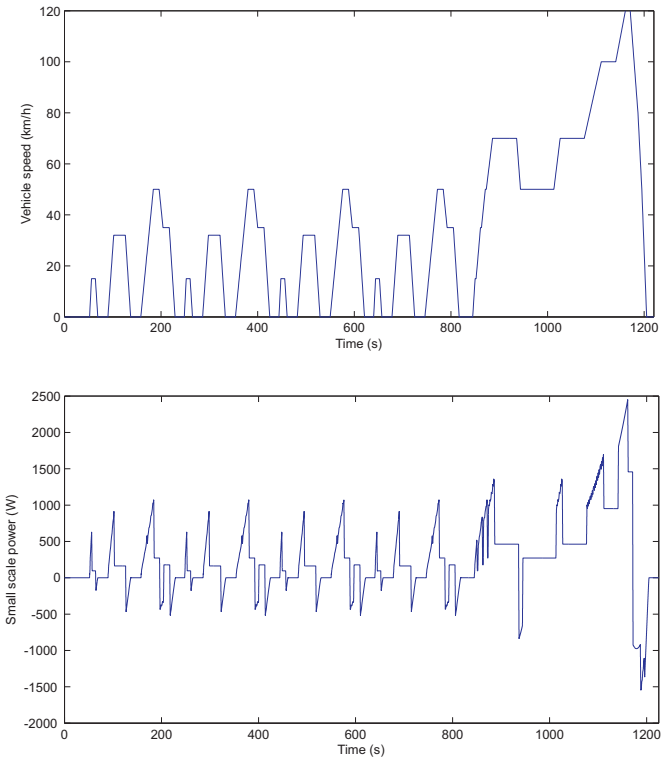

Fig. 7.12: NEDC driving cycle and downsized power (10:1)

7.5. HIL experimental results

To test the p.u. HIL simulation presented, a driving cycle is applied to the simulated system. The New European Driving Cycle (NEDC) simulates during 1225 seconds an urban and suburban route with frequent stops, as it can be seen in Fig. 7.12. The maximum speed is 120 km/h.

With this driving cycle the power requested to the downsized fuel cell/battery system is shown in Fig. 7.12. The maximum downsized power is 2500 W, which corresponds to a real 25 kW of the original application. As the simulation is carried out for a smaller system (10:1), the results presented are expressed in per-unit values.

The simulated fuel cell current is measured by a current transducer at the Sorensen DCS power source which emulates its behavior for both control schemes. The current profile is presented in per-unit values. For EMM 1 in Fig. 7.13 the fuel cell current varies between 1.2 p.u. and 2 p.u., which

are the two levels established. There is also a third level at 0.5 p.u., which corresponds to the battery recharge. For EMM 2 in Fig. 7.14 the fuel cell is kept at a constant operation point (its maximum power transfer point), which corresponds with a 2 p.u. current, when the current is referred to the base system. These current values affect the hydrogen consumption, which is 2.5e-3 l/s for EMM1 and 3.7e-3 l/s for EMM2. Due to the fact that this constant operation of the fuel cell will affect the battery SoC and voltage, the control system will measure continuously the battery voltage. It can be observed in Fig. 7.14 that when the measured battery voltage surpasses 14.4 V (1.2 p.u.) the fuel cell current decreases in order to allow a battery discharge or reduce the recharge level. On the other hand, the bus voltage variation for control scheme 1 is lower, as it varies between 0.87 and 1.2 p.u.

For both energy management modes the battery absorbs up to 5 p.u. The battery is recharged both from the fuel cell during low loads or during the regenerative braking. As the battery is reserved for the high peak currents, the bus voltage presents a variation around 1.07 p.u. for EMM 1 and around 1.1 p.u. for EMM 2. The voltage variation is of 0.33 p.u. for EMM 1 and 0.37 p.u. for EMM 2. This voltage variation is a normal situation for a battery, which needs to vary considerably its voltage in order to supply the current demanded during the charge/discharge cycles. This voltage variation is not so dramatic in other energy storage systems. For example, supercapacitors can supply or absorb hundreds of amperes during very short time intervals by just varying mV the supercapacitor voltage.

The battery absorbs the frequent regenerative braking and fuel cell current which keeps the battery SoC. However, the two different energy managements affect the SoC in a considerable way. For EMM 1 the SoC does not vary significantly during most part of the cycle, but collapses during the suburban section. EMM 2 keeps the battery SoC within more appropriate values: 40 % (0.4 p.u.) and 52 % (0.52 p.u.), which avoids the battery depletion or overcharge.

The fuel cell power varies around 2.2 p.u., which corresponds to 550 W in the downsized system and 5.5 kW in the real application. The battery power can reach nearly 5 p.u., which is 1250 W in the downsized system and 12.5

kW in the real system.

7.6. Conclusions

Hardware-in-the-loop simulation is a powerful tool for simulating systems with a high number of components, which may require a complex and expensive setup. In this Thesis, HIL simulation has been applied to a fuel cell/battery hybrid vehicle. Unlike other authors, the vehicle simulation does not include an electric machine to reproduce the regenerative braking. A combined control of a dc electronic load and dc power source allows to simulate both the vehicle power requirement and regenerative braking. This vehicle simulator can easily switch to a stationary load simulator by just changing the programmed power cycle.

The hybrid fuel cell/battery system was setup as a combination of simulated and real hardware systems. The fuel cell simulator can be setup with a programmed dc power source which is able to reproduce the fuel cell voltage and current evolution. On the other hand, the battery is a simple and modular system which can be easily introduced as hardware.

The HIL simulation is carried out under a p.u. system, which allows to downsize the whole test bench and to study the hybridization between simulated fuel cell and battery and was successfully carried out for two different control schemes.

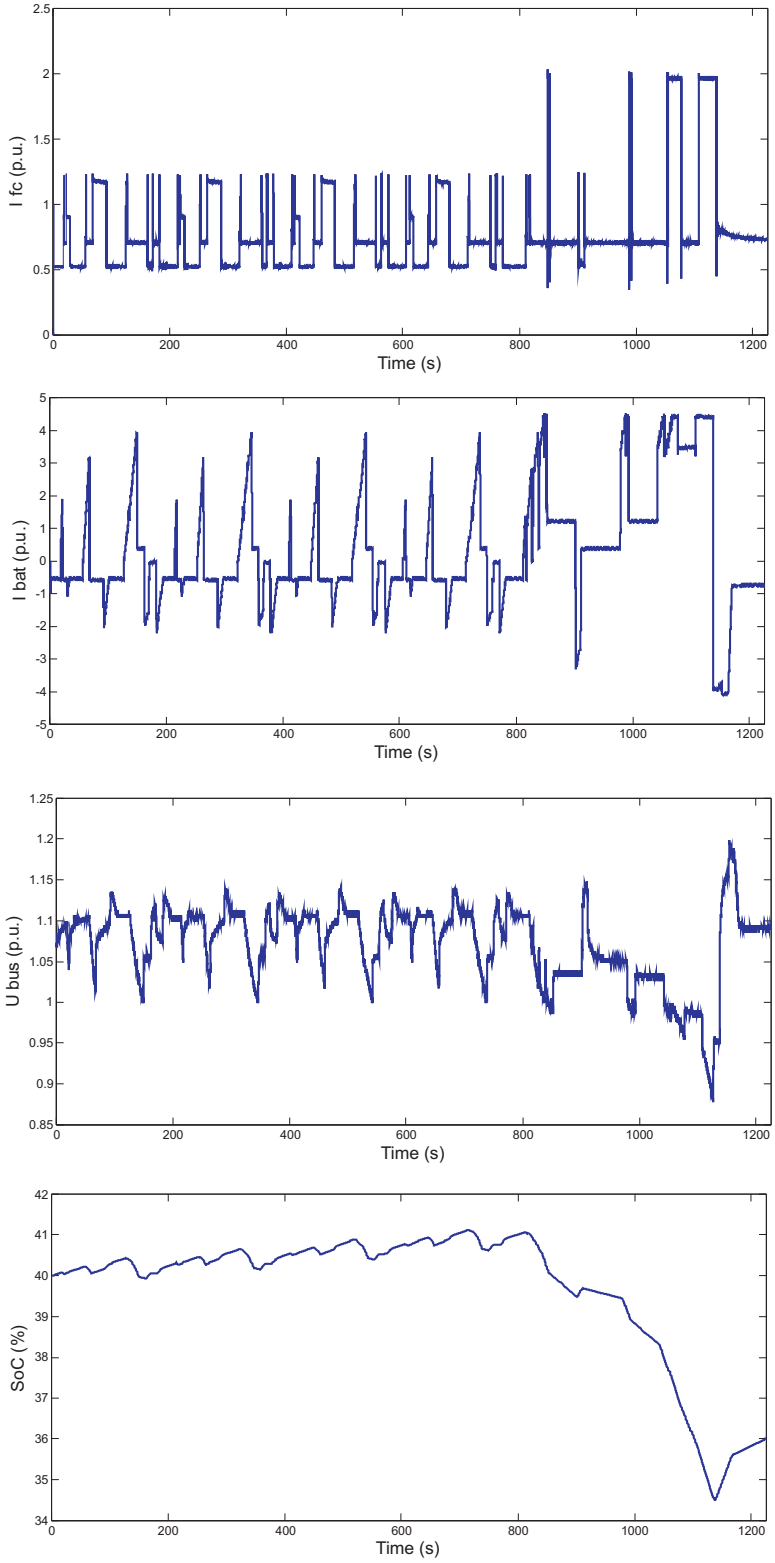

Fig. 7.13: Energy management mode 1

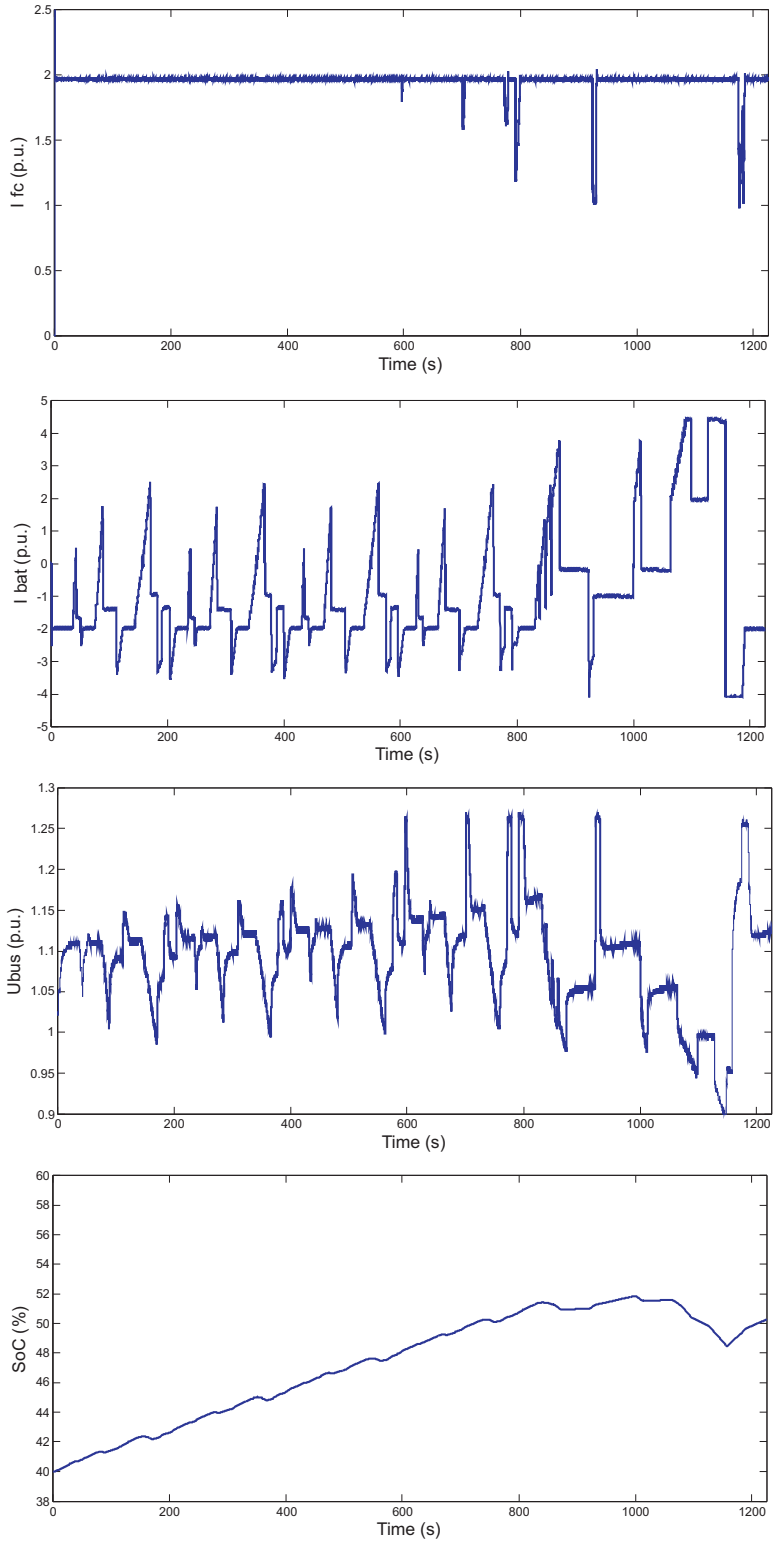

Fig. 7.14: Energy management mode 2

References

[1] R. Swenson, "Hubbert peak of oil production." Internet: http://www.hubbertpeak.com, 2009.

[2] U. A. Team, "World petroleum assessment," geological survey, U.S. Department of Interior, 2000.

[3] E. I. Administration, "International energy outlook," Report DOE/EIA-0484, Department of Energy, U.S.A, May 2009.

[4] P. Siakkis and K. Angelis, "Energy, transport and environment indicators," Pocketbook ISSN 1725-4566, European Commission, L-2920 Luxembourg, 2007.

[5] N. R. E. Laboratory, "Learning about renewable energy." Internet: http://www.nrel.gov, 2009.

[6] www.whitedogbatteries.com/battcrossect.htm, "Motorcycle battery cross section." Internet, 2005.

[7] G. Zorpette, "Super charged," *IEEE Spectrum*, vol. 42, pp. 32–37, January 2005.

[8] P. Pathapati, X. Xue, and J. Tang, "A new dynamical model for predicting transient phenomena in a pem fuel cell system," *Renewable Energy*, vol. 30, pp. 1–22, 2005.

[9] J. Garnier, M.-P. Pera, D. Hissel, F. Harel, D. Candusso, N. Glandut, J.-P. Diard, A. Bernardinis, J.-M. Kauffman, and G. Coquery, "Dynamic PEM fuel cell modeling for automotive applications," *Vehicular*

Technology Conference, vol. 5, pp. 3284–3288, October 2003. Orlando, Florida, USA.

[10] K. Cooper and M. Smith, "Electrical test methods for on-line fuel cell ohmic resistance measurement," *Journal of Power Sources*, vol. 160, pp. 1088–1095, October 2006.

[11] W. Choi, J. Howze, and P. Enjeti, "Development of an equivalent circuit model of a fuel cell to evaluate the effects of inverter ripple current," *Journal of Power Sources*, vol. 158, pp. 1324–1332, August 2006.

[12] E. Karden, S. Buller, and R. D. Doncker, "A method for measurement and interpretation of impedance spectra for industrial batteries," *Journal of Power Sources*, vol. 85, pp. 72–78, January 2000.

[13] S. Nelatury and R. Singh, "Extracting equivalent circuit parameters of lead-acid cells from sparse impedance measurements," *Journal of Power Sources*, vol. 112, pp. 621–625, November 2002.

[14] D. Baert and A. Vervaet, "A new method for the measurement of the double layer capacitance for the estimation of battery capacity," *IEEE International Telecommunications Energy Conference*, pp. 733–738, October 2003. Yokohama, Japan.

[15] A. Salkind, P. Singh, A. Cannone, T. Atwater, X. Wang, and D. Reisner, "Impedance modeling of intermediate size lead-acid batteries," *Jouranl of Power Sources*, vol. 116, pp. 174–184, July 2003.

[16] M. Thele, O. Bohlen, D. Sauer, and E. Karden, "Development of a voltage-behavior model for NiMh batteries using an impedance-based modeling concept," *Journal of Power Sources*, vol. 175, pp. 635–643, January 2008.

[17] L. Zubieta and R. Bonert, "Characterization of double-layer capacitors for power electronics applications," *IEEE Transactions on Industry Applications*, vol. 36, pp. 199–205, January/February 2000.

[18] S. Buller, E. Karden, D. Kok, and R. D. Doncker, "Modeling the dynamic behavior of supercapacitors using impedance spectroscopy,"

36th Industry Application Conference, vol. 4, pp. 2500–2504, September 2001. Chicago, USA.

[19] R. Dougal, L. Gao, and S. Liu, "Ultracapacitors model with automatic order selection and capacity scaling for dynamic system simulation," *Journal of Power Sources*, vol. 126, pp. 250–257, February 2004.

[20] W. Lajnef, J. Vinassa, O. Briat, S. Azzopardi, and E. Woirgard, "Characterization methods and modelling of ultracapacitors for use as peak power sources," *Journal of Power Sources*, vol. 168, pp. 553–560, June 2007.

[21] F. Rafik, H. Gualous, R. Gallay, A. Crausaz, and A. Berthon, "Frequency, thermal and voltage supercapacitor characterization and modeling," *Journal of Power Sources*, vol. 165, pp. 928–934, March 2007.

[22] W. Ren, M. Steurer, and L. Oi, "Evaluating dynamic performance of modern electric drives via power hardware-in-the-loop simulation," *IEEE International Symposium on Industrial Electronics*, June 2008. Cambridge, UK.

[23] R. Moore, K. Hauer, G. Randolf, and M. Virji, "Fuel cell hardware-in-the-loop," *Journal of Power Sources*, vol. 162, pp. 302–308, November 2006.

[24] R. Trigui, B. Jeanneret, B. Malaquin, F. Badin, and C. Plasse, "Hardware-in-the-loop simulation of a diesel parallel mild hybrid electric vehicle," *IEEE Vehicle Power and Propulsion Conference*, pp. 448–455, September 2007. Arlington, Texas, USA.

[25] Y. Cheng, J. V. Mierlo, P. Lataire, and G. Maggetto, "Test bench of hybrid electric vehicle with the supercapacitor based energy storage," *IEEE International Symposium on Industrial Electronics*, pp. 147–152, September 2007 2007. Brussels, Belgium.

[26] R. Schupbach and J. Balda, "A versatile laboratory test bench for developing powertrains of electric vehicles," *IEEE Vehicular Technology Conference*, vol. 3, pp. 1666–1670, September 2002. Vancouver, Canada.

[27] D. Winkler and C. Gühmann, "Hardware-in-the-loop simulation of a hybrid electric vehicle using modelica/dymola," *22nd International Battery, Hybrid and Fuel Cell Electric Vehicle Symposium and Exhibition*, pp. 1054–1063, 2006. Yokohama, Japan.

[28] Ballard Power Systems Inc., *Nexa Power Module User's Manual*, June 2003. MAN5100078.

[29] R. Kötz and M. Carlen, "Principles and applications of electrochemical capacitors," *Electrochimica Acta*, vol. 45, pp. 2483–2498, 2000.

[30] D. of Environment and Heritage, "Energy storage technologies: a review paper," tech. rep., Australian Greenhouse Office, 2005.

[31] I. Zamora, J. S. Martin, J. Mazon, J. S. Martin, and V. Aperribay, "Emergent technologies in electrical microgeneration," *International Journal of Emerging Electric Power Systems*, vol. 3, no. 2, pp. 1–30, 2005.

[32] F. Barbir, *PEM fuel cells, theory and practice*. Burlington, MA 01803, USA: Elsevier, first ed., 2005.

[33] U. Bossel, "Energy and the hydrogen economy." ABB Switzerland Ltd., 2003.

[34] A. Lovins, "Twenty hydrogen myths." Rocky Mountain Institute, February 2005.

[35] J. Larminie and A. Dicks, *Fuel cell systems explained*. West Sussex, PO19 1UD, England: John Wiley and Sons Ltd., 1 ed., 2000.

[36] R. O'Hayre, S.-W. Cha, W. Colella, and F. Prinz, *Fuel cell fundamentals*. Hoboken, New Jersey, USA: John Wiley and Sons, 1 ed., 2006.

[37] C. Spiegel, *Designing and building fuel cells*. Two Penn Plaza, New York (USA): Mc Graw-Hill, 1 ed., 2007.

[38] S. Lukic, J. Ciao, R. Bansal, F. Rodriguez, and A. Emadi, "Energy storage systems for automotive applications," *IEEE Transactions on Industrial Electronics*, vol. 55, pp. 2258–2267, June 2008.

[39] D. Berndt, "Valve-regulated lead-acid batteries," *Journal of Power Sources*, vol. 100, pp. 29–46, 2001.

[40] D. Berndt, *Maintenance-free batteries.* Baffins Lane, Chichester, West Sussex, UK: John Wiley and Sons, 1 ed., 1994.

[41] M. Wright, "Ultracapacitors." University of Alaska Fairbanks web page, 2007.

[42] A. Burke, "Ultracapacitors: why, how, and where is the technology," *Journal of Power Sources*, vol. 91, pp. 37–50, November 2000.

[43] U. Reggiani, L. Sandrolini, and G. Burbui, "Modelling a PEM fuel cell stack with a nonlinear equivalent circuit," *Journal of Power Sources*, vol. 165, pp. 224–231, February 2007.

[44] A. Balkin, "Modeling a 500 w polymer electrolyte membrane fuel cell," Master's thesis, University of Technology Sydney, June 2002.

[45] K. Adzakpa, K. Agbossou, Y. Dube, M. Dostie, M. Fournier, and A. Poulin, "PEM fuel cells modeling and analysis through current and voltage transient behaviors," *IEEE Transactions on Energy Conversion*, vol. 23, pp. 581–591, June 2008.

[46] E. Barsoukov and J. Macdonald, *Impedance Spectroscopy.* Hoboken, New Jersey, USA: Wiley and Sons, 2 ed., 2005.

[47] S. Page, A. Anbuky, S. Krumdieck, and J. Brouwer, "Test method and equivalent circuit modeling of a PEM fuel cell in a passive state," *IEEE Transactions on Energy Conversion*, vol. 22, pp. 764–773, September 2007.

[48] P. Wingelaar, J. Duarte, and M. Hendrix, "Dynamic characteristics of PEM fuel cells," *Power Electronics Specialists Conference*, pp. 1635–1641, 2005.

[49] J. Amphlett, R. Mann, B. Peppley, P. Roberge, and A. Rodrigues, "A model predicting transient responses of proton exchange membrane fuel cells," *Journal of Power Sources*, vol. 61, pp. 183–188, July-August 1996.

[50] J. Pukruspan, H. Peng, and A. Stefanopoulo, "Simulation and analysis of transient fuel cell system performance based on a reactant flow model," *International Mechanical Engineering Congress and Exposition*, November 2002. New Orleans, Louisiana, USA.

[51] C. Wang, M. Nehrir, and S. Shaw, "Dynamic models and model validation for pem fuel cells using electrical circuits," *IEEE Transactions on Energy Conversion*, vol. 20, pp. 442–451, June 2005.

[52] Z. Zhang, X.Huang, J. Jiang, and B. Wu, "Improved dynamic model considering effects of temperature and equivalent internal resistance for PEM fuel cell power modules," *Journal of Power Sources*, vol. 161, pp. 1062–1068, October 2006.

[53] M. Soltani and S. Bathaee, "A new dynamic model considering effects of temperature, pressure and internal resistance for PEM fuel cell power modules," *International Conference on Electric Utility Deregulation and Restructuring and Power Technologies*, pp. 2757–2762, April 2008. Nanjin, China.

[54] X. Yuan, J. Sun, M. Blanco, H. Wang, J. Zhang, and D. Wilkinson, "AC impedance diagnosis of a 500 W PEM fuel cell stack. part I: Stack impedance," *Journal of Power Sources*, vol. 161, pp. 920–928, October 2006.

[55] X. Yuan, J. Sun, H. Wang, and J. Zhang, "AC impedance diagnosis of a 500 W PEM fuel cell stack. part II: individual cell impedance," *Journal of Power Sources*, vol. 161, pp. 929–937, October 2006.

[56] M. Parthasarathy and J. Weidner, "Analysis of electrochemical impedance spectroscopy in proton exchange membrane fuel cells," *International Journal of Energy Research*, vol. 29, pp. 1133–1151, October 2005.

[57] E. Laffly, M. Cecile, and D. Hissel, "PEM fuel cell modeling with static dynamic decomposition and voltage rebuilding," *International Symposium on Industrial Electronics*, pp. 1519–1524, June 2008. Cambridge, UK.

[58] C. Brunetto, A. Moschetto, and G.Tina, "Fuel cell testing by elecrochemical impedance spectroscopy," *Electric Power Systems Research*, vol. 79, pp. 12–26, January 2009.

[59] W. Zhu, R. Payne, R. Nelms, and B. Tatarchuk, "Equivalent circuit elements for pspice simulation of PEM stacks ant pulse load," *Journal of Power Sources*, vol. 178, pp. 197–206, March 2008.

[60] C. Boccaletti, G. Duni, G. Fabbri, and E. Santini, "Simulation models of fuel cell systems," *Proceeding of ICEM, Electrical Machines*, 2006. Chania, Crete Island, Greece.

[61] T. Yalcinoz and M. Alam, "Dynamic modeling and simulation of air-breathing proton exchange membrane fuel cell," *Journal of Power Sources*, vol. 182, pp. 168–174, July 2008.

[62] W. Peukert, "Ueber die abhängigkeit der kapacität von der entladestromstärke bei bleiakkumulatoren," *Elektrotechnische Zeitschrift*, vol. 20, pp. 287–288, 1897.

[63] D. Doerffel and S. Sharkh, "A critical review of using the peukert equation for determining the remaining capacity of lead-acid and lithium-ion batteries," *Journal of Power Sources*, vol. 155, pp. 395–400, April 2006.

[64] E. Karden, S. Buller, and R. D. Doncker, "A frequency-domain approach to dynamical modeling of electrochemical power sources," *Electrochimica Acta*, vol. 47, pp. 2347–2356, 2002.

[65] A. Tenno, R. Tenno, and T. Suntio, "Battery impedance and its relationship to battery characteristics," *IEEE International Telecommunications Energy Conference*, pp. 176–183, September 2002. Montreal, Quebec, Canada.

[66] S. Buller, M. Thele, R. D. Doncker, and E. Karden, "Impedance-based simulation models," *IEEE Industry Applications Magazine*, pp. 62–67, March/April 2005.

[67] M. Thele, S. Buller, D. Sauer, R. D. Doncker, and E. Karden, "Hybrid modeling of lead-acid batteries in frequency and time domain," *Journal of Power Sources*, vol. 144, pp. 461–466, June 2005.

[68] F. Huet, R. Nogueira, P. Lailler, and L. Torcheux, "Investigation of the high-frequency resistance of a lead-acid battery," *Journal of Power Sources*, vol. 158, pp. 1012–1018, August 2006.

[69] F. Huet, "A review of impedance measurements for determination fo the state-of-charge or state-of-health of secondary batteries," *Journal of Power Sources*, vol. 70, pp. 59–69, July 1998.

[70] W. Viswanathan, A. Salkind, J. Kelley, and J. Ockerman, "Effect of state of charge on impedance spectrum of sealed cells. part II: Lead acid batteries," *Journal of Applied Electrochemistry*, vol. 25, pp. 729–739, 1995.

[71] B. Hariprakash, S. Martha, A. Jaikumar, and A. Shukla, "On-line monitoring of lead-acid batteries by galvanostatic non-destructive technique," *Journal of Power Sources*, vol. 137, pp. 128–133, 2004.

[72] H. Blanke, O. Bohlen, S. Buller, R. D. Doncker, B. Fricke, A. Hammouche, D. Linzen, M. Thele, and D. Sauer, "Impedance measurements on lead-acid batteries for state-of-charge, state-of-health and cranking capability prognosis in electric and hybrid electric vehicles," *Journal of Power Sources*, vol. 144, pp. 418–425, June 2005.

[73] B. Conway and W. Pell, "Power limitations of supercapacitor operation associated with resistance and capacitance distribution in porous electrode devices," *Journal of Power Sources*, vol. 105, pp. 169–181, March 2002.

[74] W. Lajnef, J. Vinassa, S. Azzopardi, O. Briat, E. Woirgard, C. Zardini, and J. Aucounturier, "Ultracapacitors modeling improvement using an experimental characterization based on step and frequency responses," *35th Annual IEEE Power Electronics Specialists Conference*, pp. 131–134, June 2004. Aachen, Germany.

[75] O. Briat, W. Lajnef, J. Vinassa, and E. Woirgard, "Power cycling test for accelerated ageing of ultracapacitors," *Microelectronics Reliability*, vol. 46, pp. 1445–1450, 2006.

[76] H. E. Brouji, O. Briat, J. Vinassa, N. Bertrand, and E. Woirgard, "Comparison between changes of ultracapacitors model parameters du-

ring calendar life and power cycling ageing tests," *Microelectronics Reliability*, vol. 48, pp. 1473–1478, 2008.

[77] H. Michel, "Temperature and dynamics problems of ultracapacitors in stationary and mobile applications," *Journal of Power Sources*, vol. 154, pp. 556–560, March 2006.

[78] D. Maclay, "Simulation gets in the loop," *IEE Review*, vol. 43, pp. 109–112, May 1997.

[79] A. Bouscayrol, "Different types of hardware-in-the-loop simulation for electric drives," *IEEE International Symposium on Industrial Electronics*, June 2008. Cambridge, UK.

[80] B. Lu, X. Wu, H. Figueroa, and A. Monti, "A low cost real-time hardware-in-the-loop testing approach of power electronics controls," *IEEE Transactions on Industrial Electronics*, vol. 54, pp. 919–931, April 2007.

[81] J. Timmermans, J. V. Mierlo, and P. Lataire, "Test platform for hybrid electric power systems: development of a hil test platform," *European Conference on Power Electronics and Applications*, pp. 1–7, 2007. Aalborg, Denmark.

[82] J. Jorcin, M. Orazem, N.Pebere, and B. Tribollet, "CPE analysis by local electrochemical impedance spectroscopy," *Electrochimia Acta*, vol. 161, pp. 929–937, January 2006.

[83] B. Shevoc, "System level modeling of thermal transients in PEMFC systems," mechanical engineering, Virginia Polytechnic and State University, Blacksburg, Virginia, January 2008.

[84] W. Choi, *New approaches to improve the performance of the PEM based fuel cell power systems.* PhD thesis, Texas University, August 2004.

[85] F. Trinidad, C. Gimeno, J. Gutierrez, R. Ruiz, J. Sainz, and J. Valenciano, "The VRLA modular design for 42 v mild hybrid systems," *Journal of Power Sources*, vol. 116, pp. 128–140, July 2003.

[86] S. Buller, M. Thele, E. Karden, and R. D. Doncker, "Impedance-based non-linear dynamic battery modeling for automotive applications," *Journal of Power Sources*, vol. 113, pp. 422–430, January 2003.

[87] A. Jossen, "Fundamental of battery dynamics," *Journal of Power Sources*, vol. 154, pp. 530–538, March 2006.

[88] E. Karden and R. D. Doncker, "The non-linear low frequency impedance of lead/acid batteries during discharge, charge and float operation," *International Telecommunications Energy Conference*, October 2001. Edinburgh, Scotland, UK.

[89] P. Mauracher and E. Karden, "Dynamic modelling of lead/acid batteries using impedance spectroscopy for parameter identification," *Journal of Power Sources*, vol. 67, pp. 69–84, July-August 1997.

[90] S. Abu-Sharkh and D. Doerffel, "Rapid test and non-linear model characterisation of solid-state lithium-ion batteries," *Journal of Power Sources*, vol. 130, pp. 266–274, May 2004.

[91] A. Fashih, "Modeling and fault diagnosis of automotive lead-acid batteries," Master's thesis, The Ohio State University, Columbus, Ohio, USA, April 2006.

[92] AENOR, "Baterías y acumuladores de plomo y arranque. parte i: Requisitos generales y métodos de ensayo." UNE-EN 50342-1, 2006.

[93] J. Stevens and G. Corey, "A study of lead-acid battery efficiency near top-of-charge and the impact on pv system design," tech. rep., Sandia National Laboratories.

[94] S. Piller, M. Perrin, and A. Jossen, "Methods for state-of-charge determination and their applications," *Journal of Power Sources*, vol. 95, pp. 113–120, June 2001.

[95] F. Lufrano, P. Staiti, and M. Minutoli, "Evaluation of nafion based double layer capacitors by electrochemical impedance spectroscopy," *Journal of Power Sources*, vol. 124, pp. 314–320, October 2003.

[96] A. Emadi, K. Rajashekara, S. Williamson, and S. Lukic, "Topological overview of hybrid electric and fuel cell vehicular power systems architectures and configurations," *IEEE Transactions on Vehicular Technology*, vol. 54, pp. 763–770, May 2005.

[97] C. Chen and M. Cheng, "Implementation of a highly reliable hybrid electric scooter drive," *IEEE Transactions on Industrial Electronics*, vol. 54, pp. 2462–2473, October 2007.

[98] A. Vath, Z. Lemes, H. Mäncher, M. Söhn, N. Nicoloso, and T. Hartkopf, "Dynamic modeling and hardware-in-the-loop testing for PEMFC," *Journal of Power Sources*, vol. 157, pp. 816–827, July 2006.

[99] R. Nelson, "Power requirements for batteries in hybrid electric vehicles," *Journal of Power Sources*, vol. 91, pp. 2–26, November 2000.

[100] T. Gillespie, *Fundamentals of Vehicle Dynamics*. SAE, 1992.

[101] M. Ehsani, Y. Gao, and J. Miller, "Hybrid electric vehicles: architecture and motor drives," *Proceedings of the IEEE*, vol. 95, pp. 719–728, April 2007.

[102] P. Thounthong, S. Raël, B. Davat, and I. Sadli, "A control strategy of a fuel cell/battery hybrid power source for electric vehicle applications," *37th IEEE Power Electronics Specialists Conference*, pp. 1–7, June 2006. Jeju, South Korea.

[103] Z. Jiang, L. Gao, and R. Dougal, "A flexible multiobjective control in active hybrid fuel cell/battery power sources," *IEEE Transactions on Power Electronics*, vol. 20, pp. 244–253, January 2005.

[104] W. Jiang and B. Fahini, "Active current sharing and source management in a fuel cell-battery hybrid power system," *IEEE Transactions on Industrial Electronics*, vol. 56, pp. 1–1, 2009.

[105] Y. Gao and M. Ehsani, "Design and control methodology of plug-in hybrid electric vehicles," *IEEE Transactions on Industrial Electronics*, vol. 56, pp. 1–1, 2009.